Dissertation submitted to
the Combined Faculties of the Natural Sciences and Mathematics
of the Ruperto-Carola-University of Heidelberg, Germany
for the degree of Doctor of Natural Sciences

Put forward by
Ana Valente
born in
São João da Madeira, Portugal

Oral examination: December 19th, 2012

On the cross-correlation between Weak Gravitational Lensing and the Sunyaev–Zel'dovich effect

by Ana Valente
under the supervision of Prof. Dr. Matthias Bartelmann

Referees:
Prof. Dr. Matthias Bartelmann, Institut für Theoretische Astrophysik, Universität Heidelberg
Prof. Dr. Luca Amendola, Institut für Theoretische Physik, Universität Heidelberg

Zusammenfassung

Die Verteilung und Entwicklung von kosmischen Strukturen - sowohl in ihren dunklen als auch baryonischen Komponenten - ist immer noch ein großer Unsicherheitsfaktor im gegenwärtigen Modell unseres Universums und ein aktives Forschungsfeld. Um dieses Thema anzugehen, krosskorrelieren wir die Signale des schwachen Gravitationslinsen- und des thermischen Sunyaev-Zel'dovich-Effektes von Galaxienhaufen als eine Funktion der Rotverschiebung. Wir benutzen das Halomodell, dass die großräumige kosmische Struktur beschreibt, um die Zweipunktkorrelationsfunktion zwischen der Dichte der dunklen Materie und des Gasdruckes in Halos abzuschätzen. Nachdem wir das dreidimensionale Leistungsspektrum berechnet und mit Hilfe der Gleichung von Limber auf den Himmel projiziert haben, schätzen wir ab, wie sich die Krosskorrelation zwischen diesen beiden Datentypen mit zunehmender Rotverschiebung aufbaut. Wir berechnen die Kovarianzmatrix für eine gegebene Krosskorrelationsfunktion und werten zu erwartende Fehlerbalken für realistische Surveys aus. Außerdem untersuchen wir zum einen, wie die Wahl von kosmologischen Parametern unsere Ergebnisse beeinflusst, und zum Anderen den Einfluss der Eigenschaften von Galaxienhaufen auf das Krosskorrelationssignal. Wir finden heraus, dass - obwohl das Krosskorrelationssignal nicht geeignet scheint, um kosmologische Parameter einzuschränken - es hochgradig von den intrinsischen Eigenschaften der Galaxienhaufen abhängt und deshalb eine Möglichkeit bietet, die Entwicklung der Gaskomponente von Halos zu beschreiben.

Abstract

The distribution and evolution of cosmic structures, in their dark and baryonic components, remains a source of uncertainty in the current model of the Universe and is an active field of research. To address this subject, we cross-correlate the weak gravitational lensing and thermal Sunyaev-Zel'dovich effects of galaxy clusters as a function of redshift. We use the halo model of large-scale structure to estimate the two-point correlation function between the dark matter density and the gas pressure in halos. After obtaining the three-dimensional power spectrum and projecting it onto the sky by means of Limber's approximation, we estimate how the cross-correlation between these two types of data builds up as redshift increases. We calculate the covariance matrix for a measured cross-correlation function and evaluate expected error bars for realistic surveys. Further, we examine how the choice of cosmological parameters affects our results and inspect the influence of cluster properties on the cross-correlation signal. We find that, although the cross-correlation signal does not seem to be suitable for constraining cosmological parameters, it is highly sensitive to the intrinsic properties of the clusters and thus provides a way to characterise the evolution of the halo gas component.

Contents

Motivation

The lack of a definitive, thorough understanding of the matter distribution and the formation of structure in the Universe continues to be a central motivation for most contemporary cosmological studies. Be it dark or baryonic matter, the ever ongoing appearance of increasingly powerful surveys and cosmological simulations promises more and better insight into this particular field, allowing the measurement and the analysis of many effects described by previous theoretical and observational research. Two of such phenomena are addressed in the work presented here.

Searching for a way to assess how the dark-matter distribution relates to the hot baryonic content of the large scale structure of the universe, we choose the weak gravitational lensing (Bartelmann and Schneider 2001) and the thermal Sunyaev-Zel'dovich (SZ) (Sunyaev and Zel'dovich 1970, 1972) effects as privileged probes of the dark matter and of the diffuse baryonic gas, respectively. Gravitational lensing, taken here as describing the line-of-sight integrated effect of the gravitational potential of galaxy clusters on the images of background galaxies, provides a detectable signal and thus a useful tool to describe structures we cannot observe directly and which are believed to dominate the matter content of the Universe (Mellier 1999; Refregier 2003; Munshi et al. 2008; Bacon et al. 2000; Laureijs et al. 2011). The thermal Sunyaev-Zel'dovich effect has developed over decades into one of the preferred tools to trace the distribution of hot, ionised gas which is trapped in the same potential wells (Birkinshaw 1999; Carlstrom et al. 2002; Planck Collaboration et al. 2011b).

In this study, we exploit the simplicity and usefulness of the halo-model framework (Cooray and Sheth 2002) to obtain the power spectrum of the cross-correlation between the weak gravitational-lensing and thermal SZ signals. Over the past couple of decades, this formalism for auto- and cross-correlation studies has become an important supplementary tool to probe cosmology, either because of its predictive power or because it paves a straightforward path towards relating theoretical expectations on dark-matter halos to observations. We focus on the low-order statistics of this cross-correlation signal and examine the covariance matrix and the redshift dependence of the correlation function based on the angular cross-power spectrum. Furthermore, we investigate the possibility of constraining cosmological models with the results obtained. Additionally, we constrain the halo mass integration to evaluate the effect of only considering hot clusters at given redshift ranges.

Previous works have dealt with the computation and analysis of cross-correlations between a wide range of signals. In particular, many of these studies have been devoted to the joint analysis of the weak gravitational lensing and thermal SZ signals. The promising nature of complementing information from the baryonic and dark-matter components of galaxy clusters prompted several works (Doré et al. 2001; Seljak et al. 2001; Munshi et al. 2011). To carry out this particular cross-correlation within the halo model framework can be a desirable choice as presented in Cooray (2000) and Cooray and Sheth (2002). Most of this analytic work has focused not only on a low-correlation level but also on higher-order statistics.

Our goal is to remain on the analysis of the two-point correlation but go beyond preceding studies and, by making use of some of the same techniques, approach the subject of how we can constrain the cosmological evolution of the matter-gas cross-correlation signal. We ultimately aim to achieve a clearer picture of the thermal history of the baryonic component of the large-scale structure.

Chapter 1

Theoretical background

Modern cosmology rests on decades of scientific research and discovery through which the image one has of the Universe nowadays became the standard. We start this thesis by succinctly addressing the most important cosmological concepts from history and literature which are relevant to understand the present study. In Section 1.1, we provide an overview of two chronological sequences of events: the scientific path that led to the building of the present-day cosmological paradigm and the sequence of events that this model entails. On the other hand, the beginning of Section 1.2 follows the stages that make up the evolutional history of the Universe. With these accounts, we aim to put our work into context and point out which is the regime of evolution history we wish to investigate. The fundamental quantities and equations of the standard cosmological model are presented. The follow-up Section 1.3 is devoted to characterising the cosmic microwave background (CMB). The main concepts of structure formation and evolution are accounted for in Section 1.4, at the end of this chapter.

All concepts presented in this chapter can be found in a more detailed account in general cosmology textbooks (Kolb and Turner 1990; Dodelson 2003; Liddle 2003; Weinberg 2008) and reviews (Lyth 1993; Trodden and Carroll 2004; Bartelmann 2010), to give a few examples.

1.1 Historical introduction

The tale of modern Cosmology is bound to always begin with the derivation of the Theories of Special and General Relativity by Albert Einstein (Einstein 1905, 1916), the core component of our current view of the Universe. His works unified the descriptions of space and time and the way these are affected by cosmological distribution of energy, respectively. The field equations of general relativity were then solved according to simplifying assumptions on the general characteristics of the cosmos. Firstly, using a cosmological constant Λ that Einstein had included in his models to achieve a stationary Universe, and famously rejected afterwards. de Sitter too included a non-zero value of Λ, a term which dominates his empty model.

The solutions of Einstein equations regarded nowadays as the most accurate description of the Universe, are the ones derived by Friedman (Friedman 1924). These include the cosmological constant and suggest an expanding fabric of the Universe. In the late 1920s, the concept of expansion was subject of further study. Lemaître too derived solutions of the field equations and additionally suggested the existence of a relation between distance and redshift (Lemaître 1931). After observing a large number of galaxies, Hubble confirmed the distance-redshift relation, thus confirming the existence of expansion. Lemaître interpreted Λ as depicting the energy fluctuation of a fluid in vacuum and provided an equation of state to describe it.

As the first steps were being given towards the description of the Universe dynamics as a whole, observations by Zwicky suggested that characteristics of clusters of galaxies were incompatible with the amount of matter that could be observed. To explain the existence of such structures, he theorised that a different kind of matter should be present in vast amounts although it could not be directly measured (Zwicky 1937c). Other studies suggested the presence of this dark matter in galaxies (Oort 1940).

Works on the mechanisms of structure growth were conducted by Lifshitz, with a linear perturbation approach (Lifshitz 1946). At approximately the same time, the first studies on structure formation at the atomic level were published. Alpher et al. (1948) presented the theory of nucleosynthesis consistent with a scenario where the Universe starts to evolve from a very hot, dense state which after a period of expansion cools down enough to allow the combination of primordial nucleons into nuclei.

In 1948 we can find the first predictions of an uniform radiation that permeates all the volume of the Universe, a relic from the first moments when the primordial fluid released photons. Known as the Cosmic Microwave Background radiation as it peaks in that part of the electromagnetic spectrum, it was found by chance by Penzias and Wilson (1965) and promptly indentified by Dicke et al. (1965).

Shortly after, independent groups predicted structures of low amplitude in the CMB (Peebles and Yu 1970; Sunyaev and Zel'dovich 1970). During the time between its detection and the detection of structures, the CMB was intensively researched theoretically, with Peebles (1982) hypothesising that the low amplitude of the CMB fluctuations could be explained by the majority of matter being a form of dark matter which doesn't interact with radiation.

Computational works shed light on other particularities of the Universe matter content: the use of numerical simulations found that the existence of cold (non-relativistic) dark matter explains the structure formation within the Friedman cosmological models (e.g. Davis et al. (1985)).

One of the most incisive moments of the last decades was the proposal of an inflationary phase of expansion in the early time of the Universe. The theory of inflation (Guth 1981) was motivated by the need to solve fundamental problems in the Friedman models and gained strength with the work of Mukhanov and Chibisov (1981) which stated that the origin of structures could reside in the inflation of quantum fluctuations.

What followed was the advent of an era devoted to observations of the Universe on all its scales, which lasts still today. Supernovae type Ia were found to be standardisable candles and are used as probes of the expansion and overall cosmological model since they provide a method for measuring cosmological distances (Howell 2011). Most important to this phase were a series of measurements of the cosmic microwave background radiation. First with the Cosmic Background Explorer (COBE), which measured the radiation in the whole sky, as well as the anisotropy pattern for the first time (Smoot et al. 1992; Boggess et al. 1992). The combination of these measurements with observations of galaxies was found to support the vision that links the cosmological constant to a kind of Dark Energy that will eventually drive the expansion of the Universe. Later, with the more precise observations by the Wilkinson Microwave Anisotropy Probe (WMAP) (Komatsu et al. 2011), not only was the ΛCDM model supported; the density fluctuations imprinted in the CMB are in agreement with what is predicted by inflationary theories. Further,

Figure 1.1: From top left to bottom right, some of the key scientists to the development of the present cosmological picture: Albert Einstein, Alexander Friedman, Georges Lemaître, Edwin Hubble, Fritz Zwicky and George Gamow.

the detection of baryonic acoustic oscillations supports the models where dark matter is treated as a non-relativistic fluid. The origins and evolution of the Universe, as modelled by the conclusions of the studies mentioned in this historical introduction are summarised in the next section.

1.2 Foundations of Cosmology

Here we present the basic formalism of the cosmological standard, or concordance, model as well as its most important corollaries: the description of time, space, dynamics and content of the Universe. The Universe, as interpreted at present day, is built upon two fundamental concepts. The first of them is the isotropy and homogeneity of the Universe on large sales: it should look about the same in all directions and points. This is a direct consequence of the Cosmological Principle, according to which any observer should, at any given time, look at the Universe and find the same general characteristics. The second belief is that the dynamics of space and time are fully described by Einstein's Theory of General Relativity (GR) (Einstein 1916). Here we show how these two simple but powerful assumptions come together to form the standard model of cosmology.

1.2.1 History of the Universe

During the described succession of discoveries and scientific advances towards a clearer picture of the cosmos, the standard model of cosmology was built up to account for the succession of events that occurred after the beginning of the Universe until the present day. Figure 1.2 depicts the basic steps believed to have been taken through the formation and evolution of structures in the Universe, in chronological order, which we here review.

It is consensually believed that the early state of the Universe can be characterised by a very dense state of a primordial plasma. It was in a very hot state, dominated by quantum fluctuations – General Relativity breaks when transported to such early stages of the cosmological history. It is speculated that the plasma expanded and cooled allowing the separation of previously symmetric interactions: gravity, strong and weak interactions and electromagnetism forces become independent. It is at this stage that inflationary theories expect an epoch of exponential expansion to have occurred. The main outcome of this expansion is the creation, via quantum fluctuations, of primordial curvature perturbations uniformly distributed over a quasi-homogeneous background. The precise mechanism that could have given rise to such a period is still an active area of research (see, e.g., Liddle and Lyth (2000) or Weinberg (2008)) but it is generally described by a particle called the inflaton.The inflationary period is expected to have ended with the decay of the inflaton into the whole a range of particle types.

After this point, the picture of the Universe starts to get more precise, as the studies of the last century have substantially clarified the chronology of events from this stage on, as well as detailed the processes taking place to a large extent.

The lowering temperatures at the photon era provide the conditions for nuclei formation, with protons and neutrons building the first nuclei of hydrogen, helium and few other elements atoms. This period is aptly known as nucleosynthesis. It is believed that at this point, radiation was the dominant energy source of the Universe. Subsequently, the decrease of density allowed the combination of the nuclei and free electrons – the so-called recombination period; during this time, the optical depth of the medium starts to

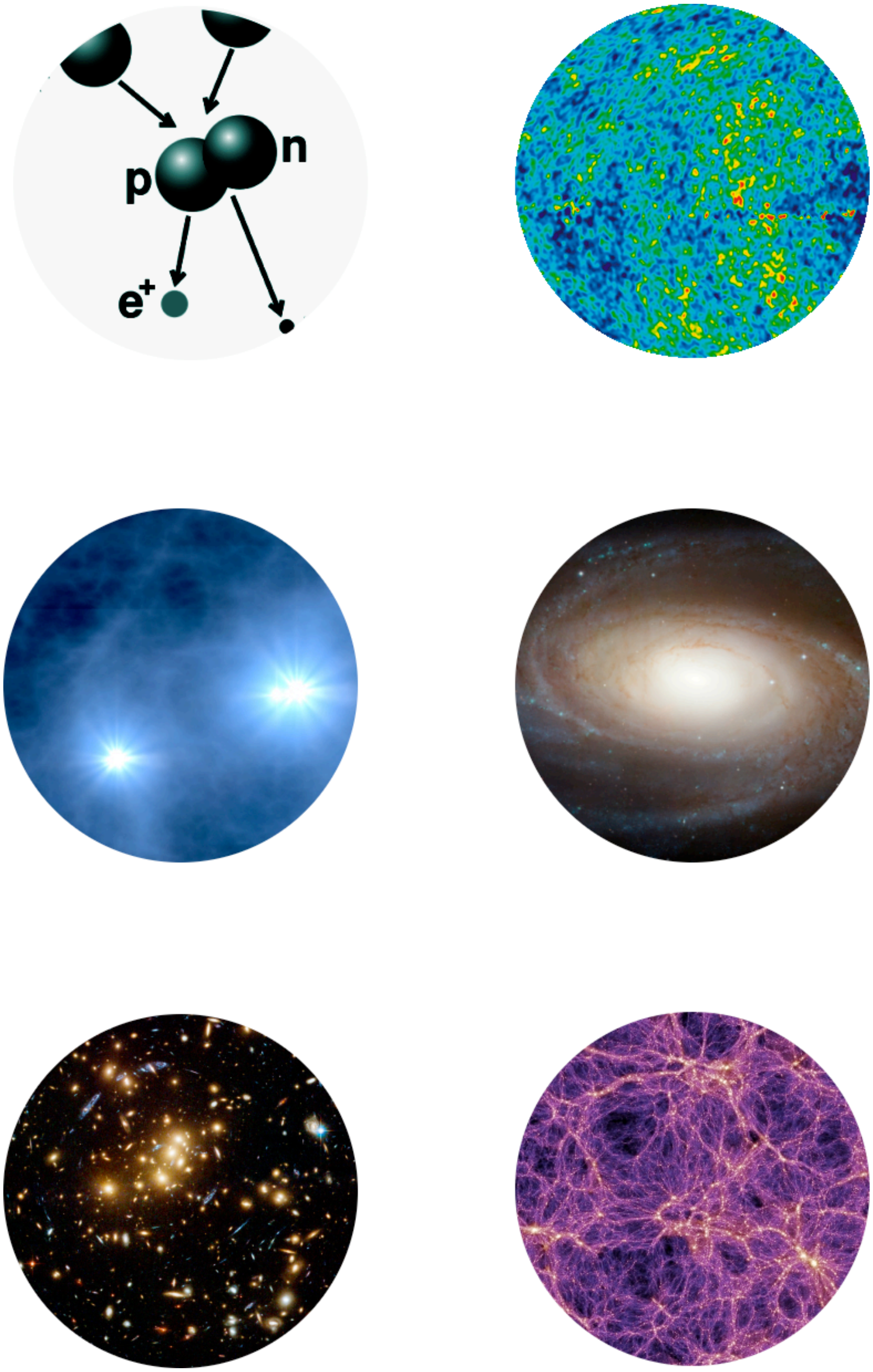

Figure 1.2: Highlights of the structure formation and evolution according to the standard cosmological model. From top left to bottom right: nucleosynthesis, details of the temperature fluctuations on the cosmological microwave background (NASA/WMAP), first stars (NASA/WMAP), galaxy (Hubble Space Telescope), galaxy cluster (Hubble Space Telescope) and the web-like configuration of the large-scale structure (Millenium simulation).

diminish and the mean paths of free photons increase steadily until they can travel through space without being subjected to scattering: this is the origin of the cosmic microwave background.

Left from the recombination epoch is a very homogeneous radiation visible over the whole sky. The primordial density perturbations created during inflation give rise to temperature fluctuations in this background. These are the seeds for structure formation. As structure slowly starts forming during this dark period of time, a re-ionization of particles occurs. In the cold dark matter scenario – the most widely accepted by now as it allows the existence of very small density perturbations as the ones observed in the CMB – structure forms from the bottom up. This means that the first structures to form are the smallest. As conditions are created for the gravitational collapse of element densities, the first stars and quasars are born. The intense radiation created by such objects re-ionises the surrounding material. The formation of structures produces progressively large objects. Stars agglomerate in galaxies; galaxies are attracted to each other and build clusters; clusters of galaxies come into contact with others nearby, creating super-clusters, in a web-like structure with empty areas permeating filaments that meet where clusters are.

The present state of the Universe seems to be characterised by an accelerated expansion phase driven by the Λ-associated density (or dark energy) of negative pressure.

There is no clear picture of the ultimate fate of the Universe. This is under debate and depends on a better assessment of the cosmological model and parameters.

In the next sections we will present the fundamental framework of the cosmological standard model and focus on particular stages of the Universe evolution. We pay special attention to: firstly, the origin of structures and the processes that characterise their growth; secondly, the observed background radiation released at the time of recombination, the CMB.

1.2.2 The cosmological standard model

The isotropy and homogeneity assumptions can be introduced in Einstein's equations of GR with the following description of space and time, the Robertson-Walker metric:

$$\mathrm{d}s^2 = -\,c^2\,\mathrm{d}t^2 \,+\, a^2(t)\,\left[\mathrm{d}r^2 \,+\, f_k(r)^2\left(\mathrm{d}\theta^2 \,+\, \sin^2\theta\,\mathrm{d}\phi^2\right)\right] \tag{1.1}$$

where $\mathrm{d}s^2$ is the line element which for the description of light is 0. c is the speed of light and r, θ and ϕ are co-moving spatial co-ordinates. a is the scale-factor which depends on proper time t (time as measured by a co-moving observer) and describes the expansion or contraction of the three-dimensional space. Physical (or proper) scales are related to co-moving ones by the scale factor as:

$$\ell(t) = \frac{a(t)}{a_0}\,\ell_0\,. \tag{1.2}$$

a_0 is commonly taken as the scale-factor at present day and given the value of 1. The parameter k is the curvature constant and its value determines the space geometry: 0 characterises it as flat and positive or negative values correspond to positively and negatively curved space, respectively. The radial function f depends on the radial co-ordinate r in different ways, for given curvature values:

$$f_k(r) = \begin{cases} k^{-1/2}\,sin(k^{1/2}\,r) & k > 0 \\ r & k = 0 \\ |k|^{-1/2}\,\sinh(|k|^{1/2}\,r) & k < 0 \end{cases}\quad. \tag{1.3}$$

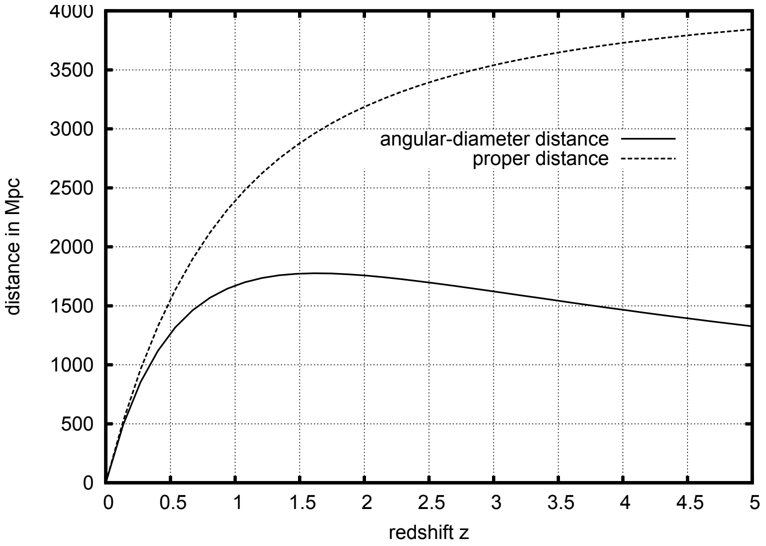

Figure 1.3: Proper and angular distances as functions of redshift. Replotted from Bartelmann (2010).

Further, the relative velocity v between two co-moving observers can be written as depending on the scale factor:

$$v(t) = \frac{\mathrm{d}\ell}{\mathrm{d}t} = \frac{\dot{a}(t)}{a(t)}\,\ell(t) \equiv H(t)\,\ell(t)\,. \tag{1.4}$$

This is the Hubble law, first discovered during the study of the velocities of distant galaxies relative to an observer (Hubble 1929): observed galaxies were receding from the observer; the relation between the velocity of recession and the distance defines the rate of expansion of the Universe at a given time, the Hubble parameter:

$$H(t) \equiv \frac{\dot{a}(t)}{a(t)}\,. \tag{1.5}$$

This parameter is also commonly used in its reduced version h, in units of 100 km s^{-1} Mpc^{-1}. As the Universe expands, the spectrum of distant objects is shifted from an initial wavelength λ to an observed wavelength λ_0. This change can be quantified by the redshift value z, given simply by:

$$z \equiv \frac{\lambda_0 - \lambda}{\lambda} = \frac{1}{a} - 1 \tag{1.6}$$

providing a useful relation between the redshift and the scale factor:

$$a = (1+z)^{-1}\,. \tag{1.7}$$

The radial function (1.3) is used to define the angular-diameter distance D_{ang}, which connects the physical and angular sizes of an object via the scale factor:

$$D_{\mathrm{a}} = a\, f_k(r(a))\,. \tag{1.8}$$

The dependence of the angular-diameter distance on the redshift is shown in Figure 1.3: after a sharp increase from redshifts 0 to 1.5, the distance slowly but steadily decreases.

Returning to the general description of the Universe dynamics, one can use the Einstein's field equations, here written in the customary Einstein notation:

$$G_{\mu\nu} = R_{\mu\nu} - \frac{1}{2} R\, g_{\mu\nu} \tag{1.9}$$

$$= \frac{8\pi G}{c^4} T_{\mu\nu} + \Lambda\, g_{\mu\nu}\,. \tag{1.10}$$

Here G and Λ correspond to the gravitational and cosmological constants, respectively. (Λ, which was initially introduced to obtain a static Universe description, is now supported by observations, as seen later on.) $g_{\mu\nu}$ describes the metric and several tensors are also depicted: the Einstein tensor $G_{\mu\nu}$, the Ricci tensor $R\mu\nu$ (with associated scalar R) and the energy-momentum tensor $T_{\mu\nu}$. The latter, combining the energy and momemtum densities of all forms of matter, is given by:

$$T_{\mu\nu} = \left(\rho + \frac{p}{c^2}\right) U_\mu U_\nu - \frac{p}{c^2} g_{\mu\nu} \tag{1.11}$$

with ρ and p as density and pressure, both functions of time. This relation hold true for an ideal fluid. U is the 4-velocity field, normalised such that $U_\mu U^\mu = -1$. Obeying the isotropy/homogeinity assumptions, the tensor becomes fully described by:

$$T_{00} = \rho \quad \text{and} \quad T_{ij} = p g_{ij}\,. \tag{1.12}$$

Introducing the Robertson-Walker metric (1.1) to the field equations (1.10) we get two relations – the Friedman equations:

$$\left(\frac{\dot{a}}{a}\right)^2 = \frac{8\pi G}{3}\rho + \frac{\Lambda c^2}{3} - \frac{kc^2}{a^2} \tag{1.13}$$

$$\frac{\ddot{a}}{a} = -\frac{4\pi G}{3}\left(\rho + 3\frac{p}{c^2}\right) + \frac{\Lambda c^2}{3} \tag{1.14}$$

The combination of these two equations yields the following equality:

$$\dot{\rho} = -3\,\frac{\dot{a}}{a}\left(\rho + \frac{p}{c^2}\right) \tag{1.15}$$

describing the first law of thermodynamics, giving the relation between density and pressure. An equation of state of the form:

$$p = w\rho c^2 \quad \text{with} \quad -1 \leq w \leq 1 \tag{1.16}$$

where the parameter w may be constant, can characterise the Universe during phases of domination of the different components of the cosmological fluid. Going through with the integration of (1.15), the solutions for ρ are of the general form:

$$\rho(t) = \rho_{\mathrm{i}} \left(\frac{a(t)}{a_{\mathrm{i}}}\right)^{-3(1+w)} \tag{1.17}$$

where the index designates initial values of the density and scalar factor. Replacing w by 0, 1/3 and -1, we get the evolution of the density field under the major influence of matter, radiation and the Λ field, respectively.

The Friedman equation (1.13) can be further re-written in terms of densities:

$$\frac{8\pi G}{3H^2}\rho + \frac{\Lambda c^2}{3H^2} - \frac{kc^2}{a^2H^2} = 1\,. \tag{1.18}$$

Defining a critical density by:

$$\rho_{\text{critical}} \equiv \frac{3H^2}{8\pi G} \tag{1.19}$$

we introduce the matter density parameter:

$$\Omega \equiv \frac{\rho}{\rho_{\text{critical}}} \tag{1.20}$$

For universes with $\Lambda = 0$, the density parameter defines the spatial geometry of the Universe:

$$\Omega = \begin{cases} > 1 & k = +1 \\ = 1 & k = 0 \\ < 1 & k = -1 \end{cases} \tag{1.21}$$

as closed, flat and open, respectively. Otherwise, defining:

$$\Omega_\Lambda = \frac{\Lambda c^2}{3H^2} \quad \text{and} \quad \Omega_k = -\frac{kc^2}{a^2H^2} \tag{1.22}$$

(1.18) simply becomes:

$$\Omega + \Omega_\Lambda + \Omega_k = 1 \tag{1.23}$$

describing the evolution of the density. We note that Ω contains the contributions of matter and radiation $\Omega = \Omega_m + \Omega_r$ and in turn, $\Omega_m = \Omega_{\text{DM}} + \Omega_{\text{b}}$. 'DM' stands for dark matter, the dominant component of structures which although not directly observed – as it is believed to not interact with electromagnetic radiation – is inferred by the gravitationally induced behaviour of the directly observable baryonic matter, labelled here with 'b'. In the standard model of cosmology, the dark matter component is assumed to be cold, meaning that the particles were well non-relativistic when they de-coupled from thermal equilibrium. This has been supported by many and diverse studies (more decisively by the cosmic microwave background measurements) hence, the standard model is also known as Λ-Cold Dark Matter model, or ΛCDM. The nature of dark matter has been heavily debated and is still poorly understood.

Combining Eq (1.14) with the above relations for the density parameters and the solutions for the equation of state (1.17), we define the acceleration parameter q, describing the rate at which the expansion of the Universe occurs:

$$q \equiv -\frac{\ddot{a}a}{\dot{a}^2} = -\frac{\ddot{a}}{aH^2} = \frac{1+3w}{2}\Omega + \Omega_\Lambda\,. \tag{1.24}$$

Evaluating the Friedman equation with the solutions for the different fluid components given by (1.17) in a Big Bang scenario (meaning that the scale factor tends to zero some finite time in the past), we find that the expansion of the Universe starts with a radiation dominated epoch:

$$H(t)^2 = H_0^2\left[\Omega_{r0}\left(\frac{1}{a}\right)^4 + \Omega_{m0}\left(\frac{1}{a}\right)^3 + \Omega_{k0}\left(\frac{1}{a}\right)^2 + \Omega_{\Lambda 0}\right] \tag{1.25}$$

PARAMETER	ESTIMATE	ERROR	
Ω_m	0.272	± 0.014	
Ω_b	0.0456	± 0.0016	
Ω_Λ	0.728	$^{+0.015}_{-0.016}$	
H_0	70.4	$^{+1.3}_{-1.4}$	km s^{-1} Mpc^{-1}
σ_8	0.809	± 0.024	

Table 1.1: Cosmological parameters of the ΛCDM model from the 7-year release of the Wilkinson Microwave Anisotropy Probe. Measurements include baryonic acoustic oscillations and type-Ia supernovae data (Komatsu et al. 2011). The parameter σ_8 corresponds to the normalisation of the power spectrum and is a measure of the clustering level, as discussed further in Section 1.4.

where the index ′0′ indicates the values at present time. As the expansion proceeds, the scale factor increases and the other terms become gradually relevant. At a certain point, there is an equilibrium between the influence of radiation and matter. The redshift at which this occurs, known as the equivalence redshift, can be easily computed and is approximately $1 + z_\mathrm{eq} = \Omega_{m0}/\Omega_{r0} \simeq 2.4 \times 10^4 \Omega_0\, h^{-2}$. The stage at which the radiation is released from the matter, in a process described in the next section, happens after this equilibrium period, at a redshift of about 1100.

Following this description, observations indicate that we are now in an Universe dominated by the cosmological constant, so that Ω_Λ is the driving source of expansion, associated to the energy type known as Dark Energy.

The extensive cosmological observations of the last decades yielded estimates of all the parameters involved in the description of the Universe. The Hubble parameter can be measured by a range of methods, from galaxy distances, Cepheid variable stars, supernovae, the Sunyaev-Zel′dovich effect or gravitational lensing. The total matter density as well as the radiation level can most accurately be estimated from the cosmic microwave background. The cosmological constant associated energy has in supernovae type Ia its most valuable proponent.

Table 1.1 shows the most recent values for these parameters, calculated from the data of the 7-year release of the Wilkinson Microwave Anisotropy Probe (Komatsu et al. 2011).

1.3 The cosmic microwave background

After an initial phase where it is dense and hot, the Universe expands. This allows the temperature to decrease, creating conditions for ions and free electrons to form a neutral fluid, releasing electrons, in a period known as recombination. During this process, the medium becomes transparent, as the mean free path of the photons increases dramatically, and by the end of recombination photons are able to travel without being scattered. Once this stage is achieved, a highly isotropic radiation field is emitted – this is known as the Cosmic Microwave Background radiation. There is a spherical radius separating the observer from the period when this emission is released defining the so-called last scattering surface.

This relic radiation of the recombination period is predicted by the Big Bang theory. It was first

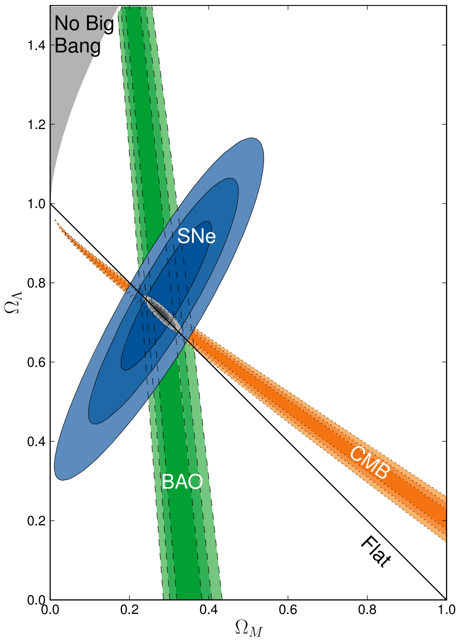

Figure 1.4: Contraints from the joint data from Supernovae Ia, galaxy clusters and the CMB in the matter-Λ density plane point to flatness of the Universe. Reprinted from Amanullah et al. (2010).

hypothesised by Lemaître and estimated by Osterbrock et al. in the search for measurements of the inter-stellar medium. By chance detected in the 1960s (Penzias and Wilson 1965) via a radio antenna, with an emission corresponding to a temperature of $\sim$ 3K, the radiation was readily and rightfully interpreted by Dicke et al. (1965) as the signature from the recombination period. It has since been extensively used as one of the most important probes of cosmological properties. The intrinsic characteristics of the CMB can reveal the structure of the Universe at the time the radiation was released. Moreover, the interaction of these photons throughout time and space with evolved structures, sheds light upon the cosmological history as well as its state at present day.

The relevance of the CMB in the current cosmological model is invaluable. Combining the output from CMB surveys with data from galaxy clusters and Supernovae Ia it was possible to constrain the cosmological parameters sufficiently to characterise the Universe as spatially flat (see Figure 1.4 by Amanullah et al. (2010)).

In the next sections we will first characterise the basic properties of the CMB radiation, focusing on the intensity and power spectra. Afterwards we shortly describe how the original radiation can be altered during its journey from the last scattering surface, through processes that create distortions in its spectrum.

1.3.1 Temperature fluctuations

The cosmic background radiation globally dominates the emission in the Universe. This emission has been extensively and precisely measured since the years of its discovery and displays a black-body intensity

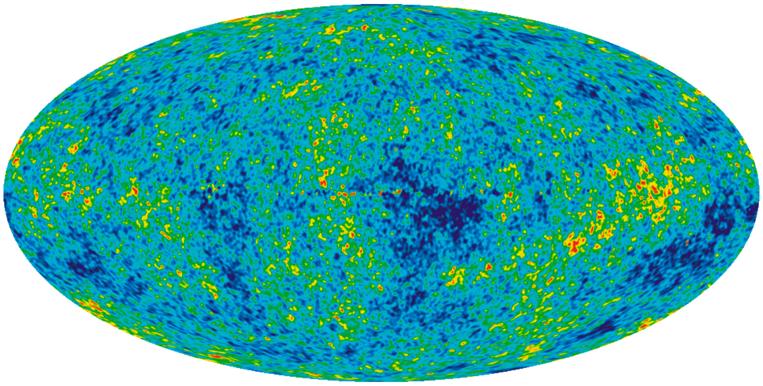

Figure 1.5: CMB all-sky map from the WMAP 7- year data release showing the temperature fluctuations of the microwave emission. Credit: NASA/WMAP Science Team.

spectrum, commonly given by the Planck distribution:

$$P(\nu, T)\,\mathrm{d}\nu \;=\; 8\pi h \left(\frac{\nu}{c}\right)^3 \frac{1}{\exp^{h\nu/k_\mathrm{B}T} - 1}\,\mathrm{d}\nu \tag{1.26}$$

with a corresponding temperature of $T_\mathrm{CMB} = 2.725 \pm 0.002$ K (Mather et al. 1999). The parameters that define the shape of the black-body intensity spectrum are the frequency ν, light-speed c, Boltzmann constant k_B and Planck's constant h.

Although the intensity of the CMB seems to be the same in every direction, a rigourous analysis to its intensity discloses the presence of very small temperature fluctuations in a seemingly isotropic distribution. The origin of these fluctuations can be divided in three main anisotropy types. The first and most intense source of temperature fluctuations is the mirroring of the density perturbations of the primordial fluid at the last scattering surface. The second source of anisotropy comprises all the mechanisms which affect the propagation of the CMB photons once they are released. The third type is related to the noise of observations. The overall anisotropy field has also been observed and Figure 1.5 displays one of these measurements by the Wilkinson Microwave Anisotropy Probe (WMAP), where all sources of noise have been removed.

The CMB temperature fluctuations are commonly statistically characterised by the correlation of the fluctuations given different positions in the sky – the power spectrum. The deviation from the average background temperature can be decomposed into spherical harmonics $Y_{\ell m}$:

$$\frac{\Delta T}{T} \;=\; \sum_{\ell=0}^{\infty} \sum_{m=-\ell}^{\ell} a_{\ell m}\, Y_{\ell m}(\theta, \phi) \tag{1.27}$$

with

$$a_{\ell m} = \int Y^{*}_{\ell m} \frac{\Delta T}{T} \mathrm{d}\Omega' \,. \tag{1.28}$$

θ and ϕ are spherical angles and $\mathrm{d}\Omega$ stands for the solid angle displacement. The coefficients defined by $a_{\ell m}$ are multi-polar moments. It is assumed that the fluctuations are a Gaussian random field, which allows the full description of the temperature fluctuations by the angular power spectrum:

$$C(\hat{n}, \hat{n}') \;\equiv\; \left\langle \frac{\Delta T}{T}(\hat{n})\, \frac{\Delta T}{T}(\hat{n}') \right\rangle \;=\; \sum_{\ell\ell'} \sum_{mm'} \langle a^{*}_{\ell m}\, a_{\ell' m'} \rangle\, Y^{*}_{\ell m}(\hat{n})\, Y^{*}_{\ell' m'}(\hat{n}') \tag{1.29}$$

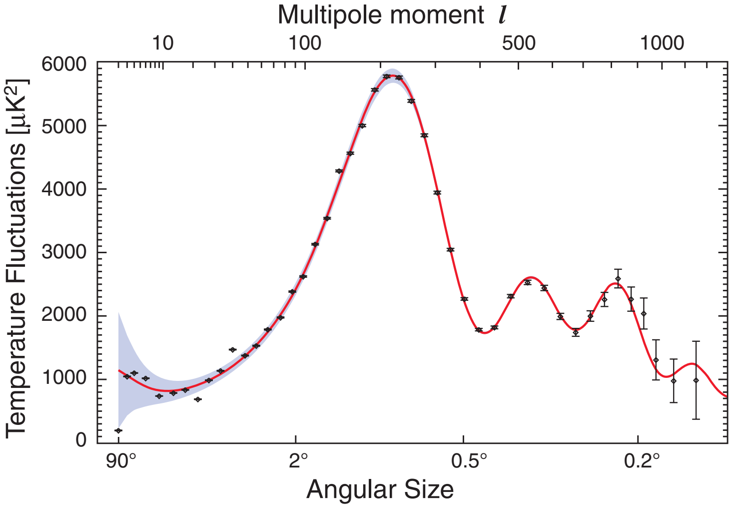

Figure 1.6: The CMB power spectrum as observed by WMAP. Credit: NASA/WMAP Science Team.

where $\hat{n}$ is a unit vector defined as the direction of the sky given by the spherical angles θ and ϕ. The correlation is averaged over an ensemble of similar perturbation configurations. Assuming symmetry over all angles (isotropy), the coefficients (1.28) are simply related to the angular power spectrum C_ℓ by:

$$\langle a^*_{\ell m} a_{\ell' m'} \rangle = C_\ell \delta_{\ell\ell'} \delta_{mm'} \tag{1.30}$$

with

$$C_\ell = \langle |a_{\ell m}|^2 \rangle \, . \tag{1.31}$$

Introducing these assumptions in (1.29) we get the spectrum dependent on the spherical angles:

$$C(\hat{n}, \hat{n}') = \sum_\ell \frac{(2\ell + 1)}{4\pi} C_\ell \, P_\ell(\cos\vartheta) \tag{1.32}$$

with $\cos\vartheta = \hat{n}.\hat{n}'$. Through C_ℓ, theoretical models and the observations can be compared. The power spectrum of the temperature fluctuations, also observed by WMAP, is shown in Figure 1.6. The CMB radiation traces many cosmological properties while travelling through space and different scales of the power spectrum shed light on different medium characteristics. This subject will be further discussed in the next section.

1.3.2 Spectrum anisotropies

A closer look at the CMB power spectrum of Figure 1.6 allows the analysis of the primary anisotropy by dividing the curve into sections corresponding to particular scale ranges as shown in Figure 1.7. This shape is theoretically predicted by the cosmological standard model. Each range is characterised by the effect of different physical processes which are imprinted in the power spectrum.

Starting at the large-scales regime we identify the region of the spectrum below angular multipoles of $\ell \sim 100$ as being under the Sachs-Wolfe effect: the phenomenon predicted by Sachs and Wolfe (1967) and

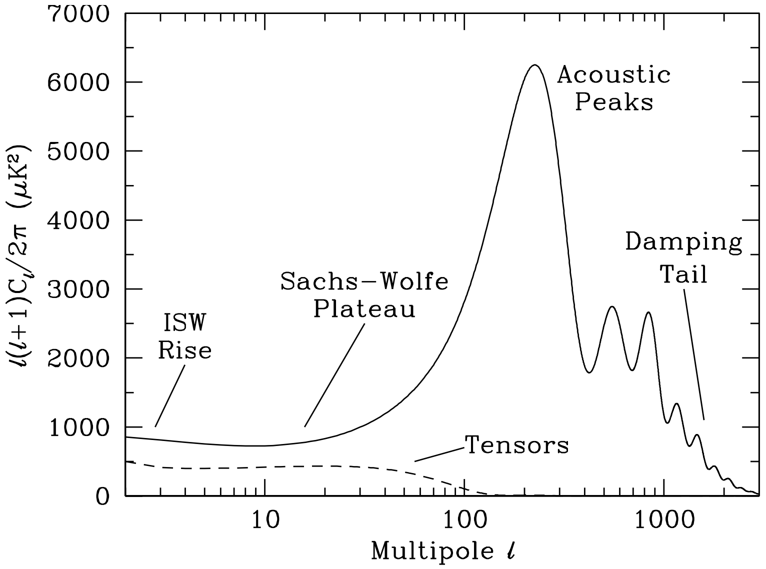

Figure 1.7: Scheme of the theoretically predicted CMB power spectrum; different parts of the spectrum are labelled according to type. Re-plotted here from Scott and Smoot (2010).

related to the gravitationally induced redshift arising from the initial potential fluctuations when photons de-coupled from matter. This region shows the influence of the initial conditions on the shape of the spectrum as it portrays temperature fluctuations before they evolved significantly. The signal at very low multipoles is the result of time variation of the gravitational potential and this rise is designated, as it is integrated over the potential changing in time, by the rise of the integrated Sachs-Wolfe (ISW) effect.

At intermediate scales of $100 \leq \ell \leq 1000$, the observed peak in the spectrum is created by the acoustic oscillations of the primordial fluid before recombination occurred. These oscillations arise from the competing of increasing gravity and counteracting pressure forces in the plasma: photons coupled with baryons felt the growth of gravitational instabilities linked to the dark matter component of the fluid. As the recombination epoch set in, the oscillations became a pattern created by the paths of photons out of the plasma and projected onto the sky we observe. The measurement of the imprint of baryons (Baryon Acoustic Oscillations, or BAOs) can be combined with data from large-scale surveys to evaluate the acceleration of the Universe – see Eisenstein (2005).

The small-scale limit of the CMB power spectrum, at $\ell > 1000$, reflects the finite duration of the recombination epoch. Although photons can start to freely travel through space, beyond the influence of the rest of the primordial fluid, this does not happen instantaneously. Rather, the recombination happens with the gradual increase of the free mean path of the photons, creating a damping tail, or Silk damping region (Silk 1968).

The description presented until now amounts to the characterisation of the primary sources of anisotropy in the CMB power spectrum. There are, however, other events that affect the power spectrum of fluctuations while it travels through space between the last scattering surface and the observer. These created the commonly named secondary anisotropies as they act as sources of contamination to the primary temperature fluctuations.

The strongest source of interaction between the CMB photons and the environment they travel through

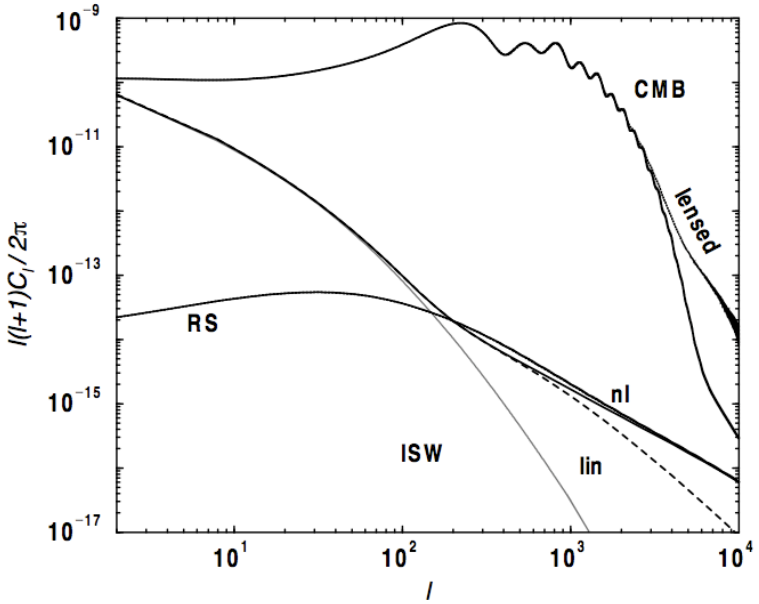

Figure 1.8: Secondary anisotropies plotted against the CMB power spectra. Adapted and reprinted from Cooray and Sheth (2002).

is the thermal Sunyaev-Zel'dovich effect (Sunyaev and Zel'dovich 1970). This signal is created when the photons exchange energy with free electrons in ionised, hot gas trapped in gravitational potential wells, in a scattering event that ultimately traces the distribution of baryonic material in the Universe – the inverse Compton scattering. As one of the phenomena evaluated in this thesis, it will later be discussed in more detail in Chapter 3. Also part of the Sunyaev-Zel'dovich (SZ) formalism is the signal arising due to the bulk motion of the hot gas relative to the rest frame of the propagating photons (Sunyaev and Zeldovich 1980). This kinetic effect, although difficult to measure directly from the spectrum, modifies the power spectrum via a Doppler shift and provides information on the dynamics of galaxy clusters and general motion of gas in the cosmos. See top panel of Figure 1.8 for a comparison between the CMB power spectra and the SZ effect signal.

The passage of the CMB photons through structures in the middle of their growth phase creates another signature in the power spectrum (see bottom plot in Figure 1.8). This late-time integrated Sachs-Wolfe, or Rees-Sciama (RS) effect (Rees and Sciama 1968) evaluates how the gravitational potentials change while the photons are passing through evolving structures and is thus intrinsically related to this stage of structure development.

It is not surprising that the path of the primordial radiation may be affected by the gravitational power of the structures it encounters, creating a lensed signal of the original spectrum. As seen in Figure 1.8 the lensing only significantly changes the spectrum at very small scales. This distortion can be used to probe the cosmological model via its parameters. For details on the effect of gravitational lensing on the CMB spectrum see, e.g. Seljak (1996).

1.4 Structure formation and evolution

The Universe described by the cosmological standard model started as an extremely dense and hot fluid which at some point started to expand. It is believed that after a first inflationary phase where it expanded exponentially, the Universe was governed sequentially by radiation, matter and dark-energy. As the expansion progresses, the primordial plasma cooled down and different energy components de-couple from the fluid. Structures are expected to have originated in the density fluctuations arising in during inflation. Small energy and density perturbations were gravitationally unstable. Such perturbations could be generated by quantum vacuum fluctuations (see, e.g., Liddle and Lyth (2000).) The growth and evolutionary path of these fluctuations until today could then create the large-scale configuration we observe nowadays: a web of filamentary structures which meet at galaxy clusters, populated by many smaller-scale structures, surrounding large voids.

The way small density fluctuations grow into larger structures was first studied by Jeans (1902) while trying to explain the mechanisms through which planets or stars are created in a nebula. According to this framework, the gravitational instabilities in a homogeneous and isotropic self-gravitating fluid will provoke in-fall of the surrounding material, thus locally increasing the density. Lifshitz (1946) introduced this description into General Relativity, devising the first linear perturbation theory.

The linear perturbation theories are adequately used when describing the growth and evolution of small fluctuations. With the rise of densities, this characterisation becomes increasingly inaccurate and higher-order perturbations need to be taken into account as well. The complexity of the configuration will eventually become too high and demand sophisticated techniques to describe the evolution of structures at later times.

In this section, we present a brief overview of the fundamental equations describing the linear growth of matter perturbations and write a few words on the non-linear analysis of structure evolution.

1.4.1 Density fluctuations and structure growth

Density perturbations are typically expressed by the density contrast field δ:

$$\delta(\mathbf{x}, t) = \frac{\rho(\mathbf{x}, t) \, - \, \bar{\rho}(t)}{\bar{\rho}(t)} = \sum \delta_k(\mathbf{k}, t) e^{-\mathrm{i}\mathbf{k}.\mathbf{x}} \tag{1.33}$$

with ρ being the density distribution and $\bar{\rho}$ representing the mean background density. $\mathbf{k}$ is here the wavenumber, depicting the scale in Fourier space. In the second equality, the excess distribution is described as a Fourier series, where:

$$\delta_k \, = \, \frac{1}{V} \int \mathrm{d}^3x \, \delta(\mathbf{x}, t) \, e^{\mathrm{i}\mathbf{k}.\mathbf{x}} \, . \tag{1.34}$$

To describe the evolution of the density fluctuation field, we use the equations of motion describing dark matter dynamics:

$$\frac{\partial \rho}{\partial t} \, \nabla.(\rho \mathbf{v}) \, = \, 0 \tag{1.35}$$

$$\frac{\partial \mathbf{v}}{\partial t} \, + \, (v.\nabla)\mathbf{v} = \, -\nabla \, \left(\phi \, + \, \frac{p}{\rho} \right) \tag{1.36}$$

$$\nabla^2 \Phi = 4\pi G \rho \, . \tag{1.37}$$

These are continuity, Euler and Poisson equations, respectively. $\mathbf{v}$ describes the velocity field which is here assumed to have a negligible dispersion. Combining the three equations within a linear regime, we conclude that, in the matter-dominated epoch, δ of sub-horizon perturbations evolves according to:

$$\ddot{\delta} \, + \, 2H\dot{\delta} \, - \, 4\pi \, G \, \bar{\rho} \, \delta = 0 \tag{1.38}$$

From the two solutions of this relation, one increases with a and describes structure growth:

$$\delta(a) \, = \, \delta_0 \, D_{+}(a) \quad \text{with} \quad D_{+} \, = \, \frac{G(a)}{G(a_0)} \tag{1.39}$$

where D_{+} is the growth factor and a_0 and δ_0 correspond to the values of the scale factor and the density contrast at present day. The growth term is well fit by the formula:

$$G(a) \, \equiv \, a \, \Omega_m \left[\Omega_m^{4/7} \, - \Omega_\Lambda \, + \left(1 + \frac{\Omega_m}{2} \right) \left(1 + \frac{\Omega_\Lambda}{70} \right) \right]^1 \, . \tag{1.40}$$

It is assumed that the primordial density field is a Gaussian random field, as the consequence of the central limit theorem applied to the superposition of quantum fluctuations in the initial field. As the mean of the density contrast is zero by definition, the whole system is to be completely defined by the variance of the field. Analysing the two-point correlation of δ and going to Fourier space, one obtains a simple correspondence between the power spectrum and the variance of δ_k given in (1.34):

$$\left\langle \hat{\delta}(\mathbf{k}) \, \hat{\delta}^*(\mathbf{k}') \right\rangle \, \equiv \, (2\pi)^3 \, P_\delta(k) \, \delta_\mathrm{D}(\mathbf{k} - \mathbf{k}') \, . \tag{1.41}$$

similarly calculated as in (A.4). The evolution of the primordial power spectrum for cold dark matter is well described by the following power law:

$$P_\delta(k) = \begin{cases} A\,k^n & k \ll k_{\rm eq} \\ A\,k^{n-4} & k \gg k_{\rm eq} \end{cases} \tag{1.42}$$

where n is the spectral index of scalar perturbations. A is a constant amplitude and the wavenumber $k_{\rm eq}$ is defined as the horizon scale at which the matter and radiation have equal densities. Moreover, we can define the variance of the density contrast:

$$\sigma_R^2 = 4\pi \int \frac{\mathrm{d}k}{(2\pi)^3}\, W_R^2(k)\, k^2\, P(k) \tag{1.43}$$

where W_R is a window function selecting the scales of interest. Traditionally, this scale is set at 8 h^{-1}Mpc. This parameter, σ_8, quantified the amplitude of cosmic structures.

Until now we have focused on the linear stages of structure growth. However, the evolution of the largest gravitationally bound structures observed in the Universe in equilibrium at present day – the clusters of galaxies – cannot be fully described by linear approximations. The need for a better understanding of how they form leads to the non-linear perturbation evolution techniques presented next.

1.4.2 Non-linear evolution of perturbations

As structures grow, the description of their evolution is no longer accurately evaluated by linear perturbation theory. As the density contrast increases, structures contract. Power will thus be transported towards larger wavenumbers.

To study the evolution of structures beyond the linear regime, N-body numerical simulations are the most powerful tool at our disposal. However, a few analytical approaches can clarify the onset of non-linear structure growth.

The spherical collapse assumes, as the denomination suggests, a spherically symmetric distribution of homogeneous overdensity and is used to estimate the threshold after which the configuration will collapse due to gravity towards its centre, independently of the surrounding influence of other overdensities. The model can also be used to determine the linear density at which the structure becomes large enough to collapse, although it doesn't account for any processes that could establish virial equilibrium. Variations of this method include removing the spherical symmetric assumption, as in the case of the elliptical collapse model.

Another approach to non-linear density growth is the Zel'dovich approximation (Zel'dovich 1970). In this method, particles are described by their co-moving co-ordinates and velocities instead of their overdensities. The initial velocity of these particles is used to define the density and the laws that govern its evolution. This approximation is reasonably accurate for as long as density perturbations are not high and particle trajectories do not cross. The particles do not notice each other's presence in this approximation. Nevertheless, the method successfully mimics the anisotropy of the growing structures that would give rise to the formation of the characteristic cosmic filaments. Moreover, it sheds light on how structures acquire angular momentum.

Nowadays, numerical simulations are widely used to study structure formation and evolution, as technical and methodical improvements allow increasingly large and complex set-ups. Simulations are not bound to many of the assumptions made in the analytical models, which mostly simplify the case-studies and may therefore affect the accuracy of the results and application range of the conclusions drawn. These studies can include a virtually unlimited amount of models (describing adiabatic evolution, including or not the effects of radiative phenomena as cooling or feedback, etc) and track how they affect the evolution of structures.The equations of motion are numerically integrated and the particles trajectories are followed over times, provided a set of initial conditions. For the definition of the initial conditions, the Zel'dovich formalism mentioned above is commonly used.

Chapter 2

The Halo Model revisited

The characterisation of structure and its distribution in the Universe is an ambitious and heavily populated field of work. From analytical approaches like perturbation theory to numerical methods such as N-body simulations of large-scale structure, there are several options for defining cosmological core features that can be used to predict and/or explain observational evidence. For the present study, we choose to use an analytical technique which provides a fairly simple and yet comprehensive, flexible framework to describe the signal of a given cosmological source: the halo model. This technique has been extensively used as the kernel for a great number of studies on dark matter, galaxy and velocity distributions, to name just a few.

Our description of the large scale structure and its overall signal is based on a specialised version of the halo model. Below we list the main characteristics of this tool, starting in Section 2.1 with a brief account of the context and ideas from which it arose. The formalism is reviewed in some detail in Section 2.2 and followed by a few notes on the possibility of extending the model to account for substructure in halos (Section 2.3). We finish this chapter by acknowledging the versatility of the halo model, which allows the study of many properties beyond what was its original intent.

A most detailed account of the halo model specifics can be found, for instance, in the extensive review by Cooray and Sheth (2002).

2.1 Concepts of the original Halo Model

The fundamental ideas of what is now known as the halo model were developed out of the need for a tool to characterise the distribution of galaxies in the universe. Half-way through the last century, Neyman and Scott (1952) theorised that galaxies clustered in halos throughout space and – finding discrete statistics appropriate to describe galaxies – developed a formalism under which halos were to be distinguished by basic properties: their size, inner structure and relative position to such other objects. It wasn't, however, until the last few decades that the collection of a series of results on these particular attributes yielded enough information to allow successful applications of the halo model formalism.

It is most consensual at this point in the history of modern cosmology that the clustered structures we observe in the universe today evolved from perturbations in a primordial, mostly uniform distribution of dark matter. Their distribution in space has been the subject of numerous phenomenological and numerical studies, providing extensive and, on the whole, concordant methods of mimicking this property. A few examples for reference: the mass function predicting halo abundances by Press and Schechter (1974) or Sheth and Tormen (1999), N-body simulations of large-scale structure by Springel et al. (2005) and observational catalogues of galaxies in Miller et al. (2005).

The inner structure of halos has also been described by several groups, being the most remarkable and pervasive models the ones of Navarro et al. (1997), Moore et al. (1999) or Einasto and Haud (1989). All of them parameterise the matter density in dark matter halos in radial distributions and most were mainly motivated by the identical behaviour found in numerical simulations like the above-mentioned while others relied on models developed from luminosity functions. In the former cases, although there is no obvious basis as far as the theoretical framework is concerned, they are nevertheless widely used and observational results of present-day surveys that seem to be in agreement with these fits support their continuous future employment (Umetsu et al. 2011, 2012).

The reasoning behind the process through which halos evolve and relate to others has also been researched intensively. This field bloomed in particular after the study published by White and Rees (1978) on the clustering properties of galaxy halos. This very popular work proposes a hierarchical formation of structures where galaxies should form inside and bear characteristics deeply connected to those of their host dark matter halos. Models of the relation between the large-scale organisation of dark matter halos we see today (through the direct or indirect methods that allow us to trace them) and correspondent observables abound, mostly evolved from the framework described by Mo and White (1996).

As light was shed on the very properties of halos that allow to define the halo model, it could then be used broadly despite a few changes of some original assumptions without changing their fundamental purpose. The discrete approach was adapted to the description of a continuous density distribution within which peaks correspond to halos. The bottom-line of the resulting halo model framework consists then of a description of the universe where all mass is contained in individual halos, characterised by their spatial abundances, a wide range of masses and with given density profiles. Moreover, it relies on a fully analytical technique whose results can be directly compared to both observations and numerical simulations. It is so a valuable alternative modelling tool.

Next, we present the method through which the correlation function of a dark matter halo distribution can be calculated under the halo model formalism.

2.2 Definition of the correlation function and power spectrum

The halo model assumes as one of its most crucial features the fact that all matter is confined to halos, characterised by their masses as well as the way these masses are arranged within them. It furthermore relies on time and spatial distribution of halos along with how these characteristics relate to those of neighbouring halos. The description we present next is a short summary of what can be found in initial chapters of the review by Cooray and Sheth (2002).

We start by defining a general matter distribution as the sum of densities over all halos and their

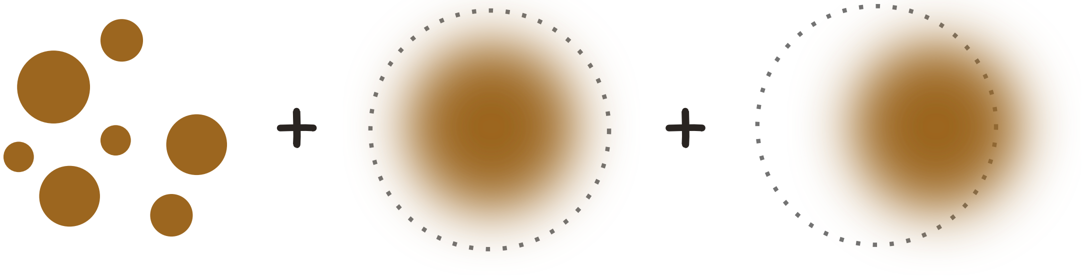

Figure 2.1: Illustration of the halo model ingredients. From left to right: spatial distribution of halos, inner distribution of density and how the density peaks can be off-set from the initially over-dense region (biasing).

positions $\mathbf{x}$:

$$\rho(\mathbf{x}) = \sum_i \rho(\mathbf{x} - \mathbf{x}_i, m_i) = \sum_i m_i \, \rho_\mathrm{n}(\mathbf{x} - \mathbf{x}_i, m_i) \tag{2.1}$$

where ρ_n is the normalised halo density profile which depends on its mass m_i and the distance to the halo centre. The normalisation is defined such that $\int \mathrm{d}\mathbf{x}' \, \rho_\mathrm{n}(\mathbf{x} - \mathbf{x}') = 1$. One can additionally introduce delta functions to achieve a useful mass-integral form:

$$\rho(\mathbf{x}) = \sum_i \int \mathrm{d}m \mathrm{d}\mathbf{x}' \; m \, \delta(m - m_i) \; \rho_\mathrm{n}(\mathbf{x} - \mathbf{x}', m) \, \delta(\mathbf{x}' - \mathbf{x}_i). \tag{2.2}$$

This form allows us to define the number density of halos by averaging the sum over the product of the delta functions:

$$n(m) = \left\langle \sum_i \delta(m - m_i) \, \delta(\mathbf{x}' - \mathbf{x}_i) \right\rangle. \tag{2.3}$$

The mean density of the distribution can then be simply given by a simple formulation:

$$\bar{\rho} = \langle \rho(\mathbf{x}) \rangle = \int \mathrm{d}m \, n(m) \, m \int \mathrm{d}\mathbf{x}' \; \rho_\mathrm{n}(\mathbf{x} - \mathbf{x}', m) = \int \mathrm{d}m \, n(m) \, m. \tag{2.4}$$

The key-function that the halo model stipulates is the two-point correlation function or its Fourier conjugate – the power spectrum – of a given dark matter halo distribution. The two-point correlation function is established as the simple sum of a Poisson term accounting for the contribution of individual halos (commonly named as 1-halo term), and a second term giving the two-point correlation between different halos (the 2-halo term):

$$\xi(\mathbf{x}) = \xi^{1\mathrm{h}}(\mathbf{x} - \mathbf{x}') \, + \, \xi^{2\mathrm{h}}(\mathbf{x} - \mathbf{x}'). \tag{2.5}$$

The two terms are determined as mass and space integrals over the number density of halos and their density profiles:

$$\xi^{1\mathrm{h}}(\mathbf{x} - \mathbf{x}') = \int \mathrm{d}m \, \left(\frac{m}{\bar{\rho}}\right)^2 n(m, z) \int \mathrm{d}\mathbf{y} \; \rho_\mathrm{n}(\mathbf{y}, m) \, \rho_\mathrm{n}(\mathbf{y} + \mathbf{x} - \mathbf{x}', m) \tag{2.6}$$

$$\xi^{2\mathrm{h}}(\mathbf{x} - \mathbf{x}') = \int \mathrm{d}m_1 \, \frac{m_1 n(m_1)}{\bar{\rho}} \int \mathrm{d}m_2 \, \frac{m_2 n(m_2)}{\bar{\rho}} \int \mathrm{d}\mathbf{x_1} \; \rho_\mathrm{n}(\mathbf{x} - \mathbf{x_1}, m_1) \int \mathrm{d}\mathbf{x_2} \; \rho_\mathrm{n}(\mathbf{x} - \mathbf{x_2}, m_2) \; \xi_\mathrm{hh}(\mathbf{x}_1 - \mathbf{x}_2, m_1, m_2) \tag{2.7}$$

where, apart from the spatial number density of halos quantified by the mass function $n(m)$ and the inner structure of the halo, given by the density profile ρ_{n}, we have the two-point correlation between halos 1 and 2. As briefly discussed later on Subsection 2.2.3, in the large-scale regime this can be approximated by the simple product of the bias b of each halo with the correlation function of linearly evolved primordial fluctuations, ξ^{lin}, yielding:

$$\xi_{\mathrm{hh}}(\mathbf{x}_1 - \mathbf{x}_2, m_1, m_2) \approx b(m_1)\, b(m_2)\; \xi^{\mathrm{lin}}(\mathbf{x}_1 - \mathbf{x}_2). \tag{2.8}$$

The presence of many convolutions in these calculations suggests using Fourier transforms. Therefore, the power spectrum is the preferable tool to describe and evaluate two-point correlations. After Fourier-transforming the correlation functions:

$$P(k,z) = P^{1\mathrm{h}}(k,z) \; + \; P^{2\mathrm{h}}(k,z) \tag{2.9}$$

which are dependent on wavenumber k and redshift z. For a given mass distribution, the model yields the following expressions for the 1-halo and 2-halo terms of the 3-dimensional two-point correlation function in Fourier space:

$$P^{1\mathrm{h}}(k,z) = \int \mathrm{d}m \left(\frac{m}{\bar{\rho}}\right)^2 n(m,z)\, u^2(k,m) \tag{2.10}$$

$$P^{2\mathrm{h}}(k,z) = P_{\mathrm{lin}} \int \mathrm{d}m_1 \,\frac{m_1}{\bar{\rho}}\, n(m_1,z)\, u(k,m_1)\, b(m_1) \int \mathrm{d}m_2 \,\frac{m_2}{\bar{\rho}}\, n(m_2,z)\, u(k,m_2)\, b(m_2). \tag{2.11}$$

These integrals over mass ranges depend on $\bar{\rho}$ as the background density appearing in the normalisation of the mass function $n(m)$, the normalised Fourier transform of the density profile $u(k,m)$ and the bias parameter b. P_{lin} refers to the linearly evolved power spectrum of primordial fluctuations.

In this section, we intended solely to present the basic framework of the halo model. The features of the power spectrum of the dark matter halo distribution, computed with the above expressions, are discussed with some detail in Subsection 4.1.1, within the next chapter dedicated to the 3-dimensional power spectra.

It is noteworthy the fact that although, it provides a fairly adequate method to describe the statistics of dark matter distributions, the halo model does have limitations. Most of these arise from simplifying assumptions which are mostly taken for practicality and clarity of thought. The accuracy suffers from these approximations and there are a few concepts that can be improved: the parametrisation of halos according to which there is spherical symmetry; how the dark matter profiles should depend on the concentration distribution as well as on the halo mass; how halo profiles are not completely smooth and may contain lower but independent peaks building an inner-halo substructure. The latter issue will be briefly addressed in Section 2.3.

The subsections ahead give a glimpse of the most commonly chosen models for the distribution, profile and bias of halos on halo model-based studies found in the literature, including the ones chosen for this work.

2.2.1 Mass function

Press and Schechter (1974) derived a simple model, popularly used afterwards, which used the spherical collapse model formalism to describe the mass distribution of halos in space and time. The co-moving

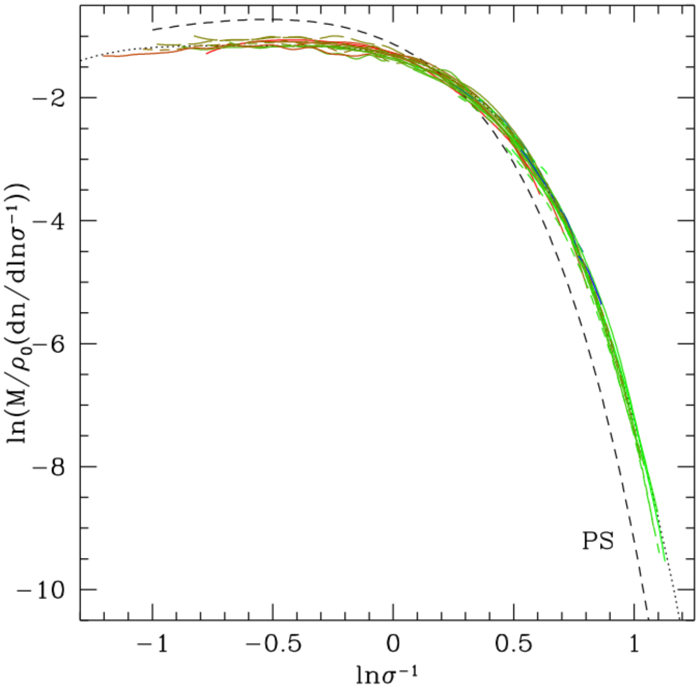

Figure 2.2: Halo mass functions estimated from numerical simulations obtained by Jenkins et al. (2001), plotted against the Press and Schechter (1974) (dashed line) and Sheth and Tormen (1999) (dotted line) results.

number density $n(m)$ of halos of mass m at redshift z was then defined with the help of the co-moving density of the background $\bar{\rho}$, the critical density required for spherical collapse at the given redshift $\delta_{\mathrm{sc}}(z)$ and the variance of the primordial density fluctuation field $\sigma^2(m)$:

$$\frac{m^2\, n(m)}{\bar{\rho}}\, \frac{\mathrm{d}m}{m} = \nu\, f(\nu)\, \frac{\mathrm{d}\nu}{\nu}. \tag{2.12}$$

The parameter ν is defined as $\nu \equiv \delta^2_{\mathrm{sc}}(z)/\sigma^2(m)$, with both quantities being calculated by linearly extrapolating their initial values to present time. The shape of the function is given by:

$$\nu\, f(\nu) = \sqrt{\frac{\nu}{2\pi}}\, \exp\left(-\frac{\nu}{2}\right). \tag{2.13}$$

A better fit to CDM models was later calculated by Sheth and Tormen (1999), taking into account the shape of halos in an elliptical description of the halo collapse. According to this work, the mass function is in better agreement with modern cosmological models when parameterised in the following way:

$$\nu\, f(\nu) = A(p)\, (1 + (q\nu))^{-p}\, \sqrt{\frac{q\nu}{2\pi}}\, \exp\left(-\frac{q\nu}{2}\right) \tag{2.14}$$

where $p \approx 0.3$, $q \approx 0.75$ and $A(p) = (1 + 2^{-p}\, \Gamma(1/2 - p)/\sqrt{\pi})^{-1}$. This approach expanded the Press-Schechter formalism – attainable with $p = 0.5$ and $q = 1$ – into a more flexible model.

With the advent of numerical simulations, the effort to find a mass function that could comprehensively describe the widest possible range of halos in the mass-redshift plane, was significantly simplified. The shape of the mass functions can be compared in Figure 2.2, taken from the study Jenkins et al. (2001), where halo mass profiles from a numerical simulations of large-scale structure are plotted and the average fit is well parameterised into the above mass function, with the following re-arrangement of the formula:

$$f(\sigma, z) \equiv \frac{m}{\bar{\rho}} \frac{\mathrm{d}n(m,z)}{\mathrm{d}\ln\sigma^{-1}}. \tag{2.15}$$

Given the very good general agreement of the mass function by Sheth and Tormen (1999) with the ones found in such studies, we chose to use it in the present work .

2.2.2 Dark matter density profile

One of the most important concepts of the halo model is the continuous distribution of matter whose peaks correspond to halos where matter is confined. In this subsection, we briefly discuss the description of how the matter is arranged within halos. We will here concentrate our description of the halo density profile on the NFW model for it was the chosen one to be used throughout the work whose results are presented in this thesis.

The already classic Navarro, Frenk and White (NFW) profile, first presented in Navarro et al. (1997), is a fully analytical description and one of the most successful versions of the more general model:

$$\rho(r, m) = \frac{\rho_{\mathrm{s}}}{(r/r_{\mathrm{s}})^{\alpha}\ (1 + r/r_{\mathrm{s}})^{\gamma}} \tag{2.16}$$

with $\alpha = 1$ and $\gamma = 2$. This density profile is parameterised by a halo-constant characteristic density ρ_{s} at the scale radius r_{s}, which introduces the dependence of the profile on the concentration c of the halo:

$$r_{\mathrm{s}} \equiv \frac{r_{\mathrm{vir}}}{c} \tag{2.17}$$

where r_{vir} is the halo virial radius and c is the concentration parameter. The characteristic density of a given halo of mass m can be determined by the total mass, a radial integration up to the virial radius:

$$m_{\mathrm{total}} \equiv \int_0^{r_{\mathrm{vir}}} \mathrm{d}r\ 4\pi r^2\ \rho_{\mathrm{s}} \tag{2.18}$$

$$= 4\pi\,\rho_{\mathrm{s}}\,r_{\mathrm{s}}^3 \left[\ln(1+c) - \frac{c}{1+c}\right]. \tag{2.19}$$

As we need to describe the two-point correlation in terms of its Fourier conjugate, it is useful to define the normalised Fourier transform of the density profile:

$$u(k, m) = \frac{\int \mathrm{d}^3\mathbf{x}\ \rho(\mathbf{x}, m)\, e^{\,\mathbf{ik.x}}}{\int \mathrm{d}^3\mathbf{x}\ \rho(\mathbf{x}, m)}. \tag{2.20}$$

On the assumption that halos are spherically symmetric and considering that all mass is contained within the virial radius, the Fourier transform becomes:

$$\int \mathrm{d}^3\mathbf{x}\ \rho(\mathbf{x}, m)\, e^{\,\mathbf{ik.x}} = \int_0^{r_{\mathrm{vir}}} \mathrm{d}r\ 4\pi\, r^2\, \rho(r, m)\, \frac{\sin(kr)}{kr} \tag{2.21}$$

$$= 4\pi\, r_{\mathrm{s}}^3\, \rho_{\mathrm{s}} \left\{ \sin(kr_{\mathrm{s}})\,[\,\mathrm{Si}(\,(1+c)\,kr_{\mathrm{s}}) - \mathrm{Si}(kr_{\mathrm{s}})\,] - \frac{\sin(ckr_{\mathrm{s}})}{(1+c)\,kr_{\mathrm{s}}} \right. \tag{2.22}$$

$$\left. + \cos(kr_{\mathrm{s}})\,[\,\mathrm{Ci}(\,(1+c)\,kr_{\mathrm{s}}) - \mathrm{Ci}(kr_{\mathrm{s}})\,]\, \right\}$$

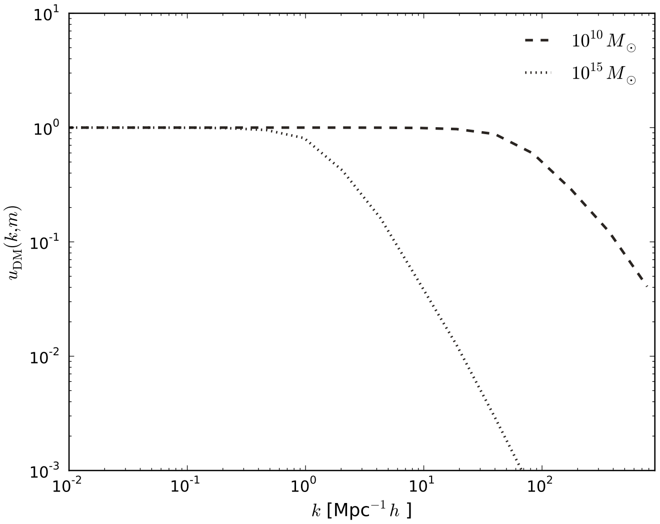

Figure 2.3: Normalised NFW profile and its dependence on the halo mass at redshift zero.

where Si and Ci are sine and cosine integrals, respectively:

$$\mathrm{Si}(x) = \int_0^x \mathrm{d}t\, \frac{\sin(t)}{t} \tag{2.23}$$

$$\mathrm{Ci}(x) = \int_0^x \mathrm{d}t\, \frac{\cos(t)}{t}. \tag{2.24}$$

Figure 2.3 shows the normalised Fourier transform of the NFW profile for halos of different masses at redshift 0. The general behaviour of these curves follows a steeper drop of density for more massive halos on small scales. This means that low mass halos dominate the contribution at small scales or, conversely, that the most massive halos contribute to the total power at the largest scales.

Although this and sibling profiles are not theoretically motivated, they often very accurately describe the distribution of matter around the centres of stable, gravitationally bound structures. Nevertheless, as mentioned earlier in this chapter, not only simulations are in good agreement with these density profiles. Observational data are too supporting this formalism (Umetsu et al. 2011, 2012). For alternative models motivated by observational estimates of the density profile like the works of Einasto and Haud (1989) or Sérsic (1963), the reader is referred, for instance, to the works in Merritt et al. (2006) or Coe (2010) where comparisons in between all classic and recent models are extensively studied. Figure 2.4 shows a glimpse of how the most commonly used models compare with each other and simulations.

2.2.3 Bias

With fairly good descriptions of how halos are distributed spatially and how matter is distributed within halos, we only lack information on how the configuration of dark matter halos is biased relative to that of the mass. It is believed that from the initial fluctuation field, only the configurations with enough density were able to collapse over time. Following the work by Mo and White (1996), the halo bias relation $\delta_{\rm h}$ can

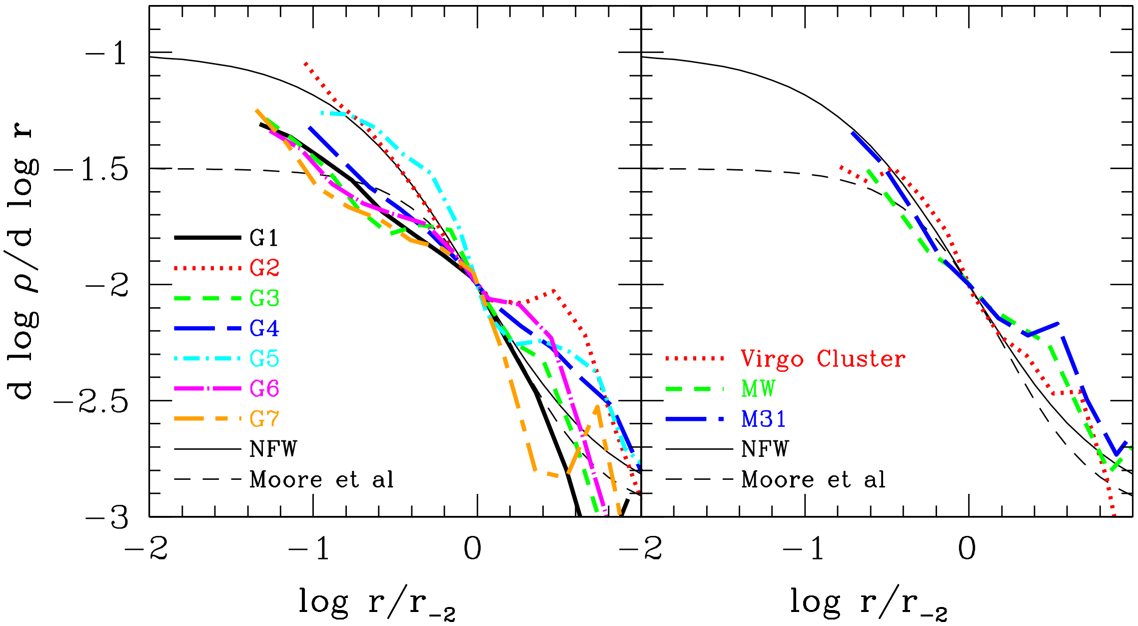

Figure 2.4: Dark matter density profiles of different models compared to simulation results. NFW and model by Moore et al. (1999) are plotted against profiles from simulated halos (left panel) and the estimated profiles of the Milky Way, M31 and the Virgo Cluster (right panel). Plot adapted from Hayashi et al. (2004).

be estimated through the expression:

$$\delta_{\mathrm{h}}(m, z_1 \,|\, m_V, V, z_0) = \frac{N(m, z_1 \,|\, m_V, V, z_0)}{n(m, z_1)V} - 1. \tag{2.25}$$

This overdensity is defined in a conditional manner and dependent on two halo number densities which trace the halo distribution at different redshifts z_0 and z_1 with $z_1 > z_0$. N denotes a conditional mass function of halos with a given mass m at a given collapse redshift z_1, which at redshift z_0 are within a volume V with mass m_V. The above equality contains a link in between the distribution of overdensities and that of the matter, since $M/V = \bar{\rho}(1+\delta)$.

What we need now is to introduce models to describe N, where the obvious choice would be any of the presented earlier in Subsection 2.2.1. n depends on the way halos evolved in between z_0 and the collapse and so the quantity $\delta_{\mathrm{sc}}(z_1)$ needs to be taken into account in order to describe the mass function. The description of ν in Eq. (2.12) can be replace by:

$$\nu_{10} = \frac{\delta_{\mathrm{sc}}(z_1) \; - \; \delta_0(\delta, z_0)}{\sigma^2(m) - \sigma^2(m_v)} \tag{2.26}$$

where $\delta_0(\delta, z_0)$ corresponds to the initial overdensity evolved linearly so that at z_0 it has an overdensity of δ. Plugging the above parameter in model of Eq. (2.14) in Eq. (2.25) and taking first order approximations, one can simply calculate the overdensity resorting to the expression:

$$\delta_{\mathrm{h}} \approx \delta \left(1 + \frac{q\nu - 1}{\delta_{\mathrm{sc}}(z_1)} + \frac{2p/\delta_{\mathrm{sc}}(z_1)}{1 + (q\nu)^p} \right) = b_1(m, z_1)\, \delta \tag{2.27}$$

stating a proportionality between the overdensity of halos and the overdensity of the mass, via the bias parameter b which depends on the halo masses and their virialisation redshifts. This is the result we use in the present work. The halo-halo term in the correlation (2.7), between points in two halos of masses m_1 and m_2 becomes simply:

$$\xi_{\mathrm{hh}}(r, m_1, m_2) \approx b(m_1)\, b(m_2)\; \xi^{\mathrm{lin}}(r) \tag{2.28}$$

with the variable r stating its spatial dependency. Hence, the power spectrum counterpart of this term is calculated through the following approximation:

$$P_{\mathrm{hh}}(k, m_1, m_2) \approx,\, b(m_1)\, b(m_2)\; P^{\mathrm{lin}}(k) \tag{2.29}$$

which can be recognised in Eq. (2.11).

2.3 Substructure and the extention of the Halo Model

The halo model has been extended to account for the existence of substructure in halos, as suggested by observations (e.g. galaxy halos within galaxy clusters halos) and numerical simulations alike (see Springel et al. (2008) or Giocoli et al. (2010a,b) and references therein). Unlike the original premise of the model, halos in simulations of hierarchical clustering do not evolve into a purely smooth and spherically symmetric density distribution of matter.

In the scenario where sub-structure is accounted for, each of the halo terms presented in Eqs. (2.10) and (2.11) is split in two additional components. These describe the contribution of individual sub-halos plus their mutual autocorrelation, in a very similar manner to what is done when describing the spatial distribution of their host halos. Adapting the derivation results by Sheth and Jain (2003):

$$P^{1\mathrm{h}}(k) = P^{1\mathrm{h}}_{\mathrm{ss}}(k) + P^{1\mathrm{h}}_{\mathrm{sc}}(k) + P^{1\mathrm{h}}_{1\mathrm{c}}(k) + P^{1\mathrm{h}}_{2\mathrm{c}}(k) \tag{2.30}$$

$$P^{2\mathrm{h}}(k) = P^{2\mathrm{h}}_{\mathrm{ss}}(k) + P^{2\mathrm{h}}_{\mathrm{sc}}(k) + P^{2\mathrm{h}}_{2\mathrm{c}}(k). \tag{2.31}$$

The sums in the above expressions are the result of two-point correlations between the different elements of a halo, now divided in a smooth component and the clumps that populate it. These correlations are illustrated for the one-halo term in Figure 2.5, and the subscripts in the above equations correspond to:

- ss: smooth-smooth correlation in between two points of smooth components
- sc: smooth-clump correlation in between a point in a smooth component and another in a clump
- 1c: correlation between two points within one halo clump
- 2c: correlation between points of different clumps.

In the case of the 2-halo term, an identical exercise can be done, leading to consider the same kind of correlations, though now with points in two different host halos. This means that the two-halo component of the power spectrum has three instead of four sub-components.

Sheth and Jain (1997) modelled large-scale structure considering the probable occurrence of sub-halos and concluded that the inner structure of halos should have predominance in the signal that arises from clustering, especially on the small-scale regime. On large-scales, however, it is expected that the correlation in between particles from different halos contributes the most to the overall signal.

In the particular case of the work presented in this thesis, the characterisation of structure with host- and sub-halos was tested and decided against. As it will later be shown in Subsection 4.1.3, the inclusion of

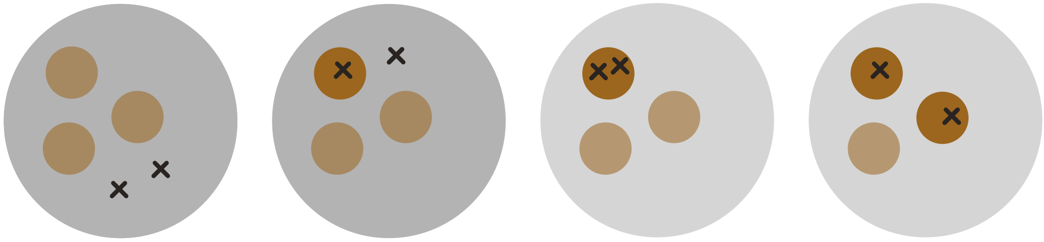

Figure 2.5: Illustration of correlation terms in the extended halo model. Depiction of area points to be correlated are, for the one-halo term, from left to right: smooth-smooth, smooth-clump, 1-clump (points in the same sub-halo) and 2-clump (points in distinct sub-halos) components.

the substructure in the cross-correlation between dark matter and gas does not substantially add insight to the signal source.

2.4 Potential uses of the Halo Model

The halo model provides a versatile method to analytically investigate the statistics of signals arising from virtually all the components of the Universe. Here we list a few of its most important applications while leaving an open door to others.

■ **Galaxies** The work by White and Rees (1978) introduces the notion that galaxies are always enclosed by parent halos and that the properties of the latter are indelibly related to the way galaxies form and evolve. Following the original purpose of the halo model, the study of the galaxy distribution is mostly focused on the questions about the origins mechanisms of clustering. Observations of galaxies from the last decades point to a galaxy-distribution correlation function described by a power law (see, e.g. Connolly et al. (2002)). Although the slope of the power spectrum from dark matter halos can coincide with such a curve on small scales, the nature of the differences found on larger scales is an interesting riddle, one that the halo model might help to decipher. By using the mass functions to describe the distribution of galaxies within halos, the halo model not only provides a method to calculate the respective auto-correlation power spectrum. It additionally allows for cross-correlating the galaxy population with the parent halos via the formalism presented previously in this chapter. With scale-bound characteristics of these spectra, one might hypothesise how small can the mass of a galaxy be, what is the relation between the galaxy distribution and its masses or the mean dark matter mass in regions inhabited by galaxies. Most importantly, clues can be found about the mechanisms that fuel the formation and evolution of galaxies.

■ **Velocities** The study of large-scale velocities under the framework of the halo model is motivated substantially by the ability to discern between the linear and non-linear contributions to the signal. The total velocities (and, more importantly, their dispersions) are typically the sum of a virial component with an intrinsic halo one, and they depend mainly on the halo masses and overdensities. The halo model provides a natural way of explaining the shape of the non-linear distribution of velocities: a Gaussian core with exponential wings. Looking into the separation in between galaxies and their mean velocities, it is possible to analyse the aspects of the gravitational interaction among them and the dependence of this mechanism with scales. Moreover, as the masses and velocities are the main components of this method, it is intuitive and easy to estimate the momentum and its cross-correlations with overdensities or the velocity distribution. It is also possible to examine the redshift-space distortions in the non-linear regime of clustering.

■ **Weak gravitational lensing** One of the two measurable effects to which the next chapter will be dedicated is the weak gravitational lensing, tracing the large-scale structure through the slight light deflection of background sources. Its main observable is the shear, the distortion of lensed galaxies. The projection of the shear is directly related to the 2-dimensional convergence parameter, the angular power spectrum of which is easily obtained via the projection of the expressions presented in Eqs. (2.10) and (2.11). This use of the halo model can shed light upon how the different masses of halos may affect the power spectrum and helps to evaluate the characteristics of the signal from surveys with given physical properties. A more detailed description of this method is found in the next chapters. The formalism used for determining the power spectrum through the halo model can also be used for higher-order statistical studies. In the weak lensing field, these statistics allow the study of non-Gaussianities and provide an alternative method to estimate cosmological parameters or to examine the non-linear evolution of the large-scale structure. Furthermore, it is possible to cross-correlate galaxy and mass distributions by the two-point correlation function of the cosmic shear and galaxies as well as through the foreground-background source correlation. The choice of probe depends on which scale one is interested in studying.

■ **The Sunyaev-Zel'dovich Effect** The thermal form of the Sunyaev-Zel'dovich effect traces the distribution of hot, ionised gas within gravitational potential wells. An effective tracer of large-scale structure, it is a valuable addition to the list of signals which can be evaluated through the halo model. The introduction of baryons in this context does, however, involve cumbersome models and calculations which are not always fully analytical. By defining a gas density model and its temperature profile for a given halo, one can compute the gas pressure power spectrum and project it into the 2D form: the SZ effect power spectrum. From this scheme, it is possible to analyse and infer the different contributions of different masses at different scales. In the core of the study presented in this thesis is the cross-correlation signal in between the gas pressure (evaluated through the SZ effect) and the dark matter distribution (measured via weak lensing). Further, Tte temperature fluctuations created by the movement of clusters through the CMB radiation are studied under the designation of kinetic SZ effect. With the definition of a line-of-sight velocity distribution and matter density it is possible to predict the power spectrum of this phenomenon. Although this is not an easily observable effect, the theoretical approach enables the study how cluster velocities relate to density peaks or estimates of a possible cross-correlation with the thermal effect.

■ **Non-linear Integrated Sachs-Wolfe Effect** The temperature fluctuations due to the integrated Sachs-Wolfe effect, briefly mentioned in Section 1.3.2, are related to the time derivative of the gravitational potential while the light is crossing them. The power spectrum of the ISW can be estimated by using density field and scale factor within the halo model formalism. Conveniently, the power spectrum of the density field variation is directly related to that of the momentum-density field so that further cross-correlations with any of these quantities are quite straightforward. On small scales, the main contributor to this overall effect is the non-linear component, the Rees-Sciama effect. This result is also directly related to the study of the velocity dispersion through the halo model framework.

Chapter 3

Probes of the large-scale structure

FROM ALL THE COSMOLOGICAL OBSERVABLES at our disposal we initially picked those providing complementary information from large-scale structure: the weak gravitational lensing and the Sunyaev-Zel'dovich (SZ) effect. Both measurements trace galaxy clusters through different components, dark matter and hot gas, respectively. Through their shared property, we eventually correlated the two signals in the expectation to gain insight on the way the dark component of halos relates to their baryonic distribution. We further investigated the connection between the SZ effect with the x-ray emission from the same hot gas in large-scale structures, attempting to make use of the different dependences of each phenomenon on the cluster properties.

In this chapter, we review the observables used in this thesis to some detail as well as their description via the halo model. Each section of this chapter starts with the presentation of the basic features of the respective observable effect followed by the auto-correlation power spectrum within the formalism used in this work. Section 3.1 deals with the weak gravitational lensing formalism and Section 3.2 shows the properties and description of the SZ effect framework.

For more details on the theoretical aspects mentioned in this chapter we refer the reader to the following reviews: for weak gravitational lensing, Bartelmann and Schneider (2001) or Refregier (2003) and on the SZ effect, Birkinshaw (1999) or Carlstrom et al. (2002).

3.1 Dark matter and weak lensing

We start our chapter on cosmological phenomena by addressing the measurement that allows the characterisation of the dark matter distribution that forms the large-scale structure. The many historical and theoretical aspects documented in this section can be found on several reviews on the subject of general gravitational lensing (Narayan and Bartelmann 1996; Schneider 1996; Blandford and Narayan 1992) or weak gravitational lensing (Bartelmann and Schneider 2001; Refregier 2003; Mellier 1999).

The deflection of light by the gravitational influence of cosmological objects while following the paths from source to the observer is a corollary of combining Maxwell's works and Einstein's Theory of General Relativity. The idea that the gravitational potential of an object can modify the trajectory of light was not new before Einstein (1915) and Einstein (1936) quantified the deflection of light by the sun or wrote

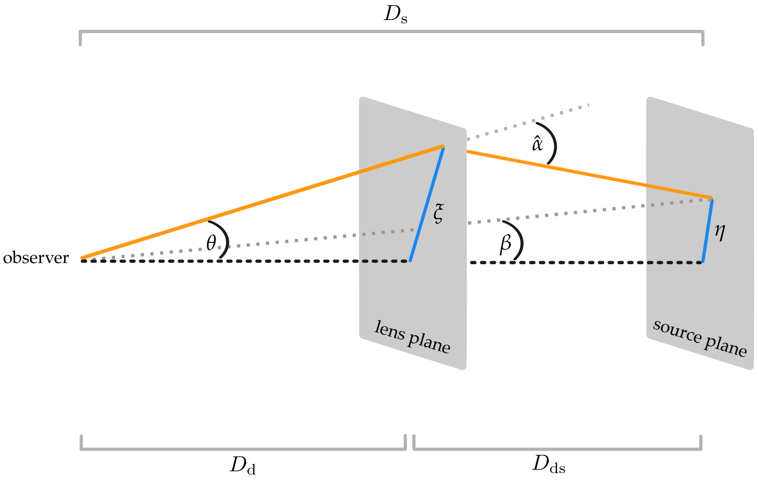

Figure 3.1: Illustration of the gravitational lensing basic mechanism.

down the formalism of the lensing effect of a prototype star, respectively. Not much later, Zwicky (1937a,b) hypothesised that the deflection of light from background sources by galaxies should be observable and stated with certainty the possibility of observations of gravitational lensing by nebulae. Several detections followed these and other publications over the years: gravitational lensing by stars (Dyson et al. 1920; Alcock et al. 1993), then by increasingly large objects (Walsh et al. 1979) until the first observations of lensing by galaxy clusters were successfully obtained (Soucail et al. 1987; Lynds and Petrosian 1986).

Proved to be a effective and powerful probe of the Universe on many scales, gravitational lensing has been used extensively in diverse astrophysical studies. In this section, we introduce the fundamental framework of gravitational lensing and its most important sub-genres, as well as applications. Most importantly to our work, we review the basics of weak gravitational lensing and express this cosmological phenomenon in halo model formalism terms.

3.1.1 Principles of gravitational lensing

The essential concept of gravitational lensing depends on the fact that light travelling throughout the Universe is subjected to the influence of neighbouring objects and their gravitational fields. The deflection of light coming from a given background source by a foreground object acting like a lens is described by basic geometrical considerations. Figure 3.1 shows the basic scheme of the lensing set-up: an observer and a single source with a deflecting object in between the two, along the line-of-sight, an optical axis perpendicular to the planes containing the lens and the source. In this simple example where no other objects are involved, we consider that the position of the source on the source plane is given by:

$$\boldsymbol{\eta} = \frac{D_\mathrm{s}}{D_\mathrm{d}}\boldsymbol{\xi} - D_\mathrm{ds}\,\hat{\boldsymbol{\alpha}}(\boldsymbol{\xi}) \tag{3.1}$$

with D_s, D_d and D_ds representing the distances from observer to source plane, from the observer to the lens (or deflector) plane and between the lens and source planes, respectively. $\hat{\boldsymbol{\alpha}}$ represents the deflection angle, and this value depends on the distance in the lens plane between the optical axis and the deflected light path. To define $\hat{\boldsymbol{\alpha}}$, one can resort to predictions of General Relativity according to which when gravity is weak and so the lensing system stays far outside the Schwarzschild radius R_S - always the case in gravitational lensing, even if lenses are galaxy clusters - the deflection angle created by a point mass M simply becomes:

$$\hat{\alpha} = \frac{4\,GM}{\xi\,c^2}. \tag{3.2}$$

As only small angular separations are being evaluated, the field equations of General Relativity can be linearised and the overall lensing effect arising from several lenses becomes the simple sum of each contribution. Considering a mass distribution, the resulting deflection angle is obtained through the following integral over the entire lens plane:

$$\boldsymbol{\alpha}(\boldsymbol{\xi}) = \int_{\mathrm{IR}^2} \mathrm{d}^2\xi' \, \frac{4\,G\,\Sigma(\boldsymbol{\xi'})}{c^2} \, \frac{\boldsymbol{\xi} - \boldsymbol{\xi}'}{|\boldsymbol{\xi} - \boldsymbol{\xi}'|^2} \tag{3.3}$$

where the quantity $\Sigma(\boldsymbol{\xi'})$ is the surface mass density, a projection of the mass. Replacing physical by angular co-ordinates with $\boldsymbol{\eta} = D_{\mathrm{s}}\boldsymbol{\beta}$ and $\boldsymbol{\xi} = D_{\mathrm{d}}\boldsymbol{\theta}$, the source position from Eq. (3.1) is converted to:

$$\boldsymbol{\alpha}(\boldsymbol{\theta}) = \frac{D_{\mathrm{ds}}}{D_{\mathrm{s}}} \, \hat{\boldsymbol{\alpha}}(D_{\mathrm{d}}\boldsymbol{\theta}) = \frac{1}{\pi} \int_{\mathrm{IR}^2} \mathrm{d}^2\theta' \, \kappa(\boldsymbol{\theta}') \, \frac{\boldsymbol{\theta} - \boldsymbol{\theta}'}{|\boldsymbol{\theta} - \boldsymbol{\theta}'|^2}. \tag{3.4}$$

Here we have defined the dimensionless surface density as:

$$\kappa(\boldsymbol{\theta}) = \frac{\Sigma(D_d\boldsymbol{\theta})}{\Sigma_{\mathrm{cr}}} \quad \text{with} \quad \Sigma_{\mathrm{cr}} = \frac{c^2}{4\pi G} \, \frac{D_{\mathrm{s}}}{D_{\mathrm{ds}} D_{\mathrm{d}}} \tag{3.5}$$

being the critical surface density. The value of Σ_{cr} quantifies the threshold surface density classifying lenses as strong or weak, depending on whether $\kappa \gg 1$ is valid everywhere (therefore creating weak lenses) or $\kappa \ll 1$ for some angles (originating strong deflectors). One can finally define the lens equation as:

$$\boldsymbol{\beta} = \boldsymbol{\theta} - \boldsymbol{\alpha}(\boldsymbol{\theta}). \tag{3.6}$$

The origin of multiple images produced by gravitational lenses is enclosed in this equality: if the solution of this equation is multiple for the same position in the source plane, multiple images are produced by the lens.

The definition of the deflection angle $\boldsymbol{\alpha}(\boldsymbol{\theta})$ presented in Eq. (3.4) can be associated the corresponding deflection potential $\psi(\boldsymbol{\theta})$. With $\boldsymbol{\alpha} = \nabla\psi$:

$$\psi(\boldsymbol{\theta}) = \frac{1}{\pi} \int_{\mathrm{IR}^2} \mathrm{d}^2\theta' \, \kappa(\boldsymbol{\theta}') \, \ln|\boldsymbol{\theta} - \boldsymbol{\theta}'| \,. \tag{3.7}$$

This potential is useful as it satisfies the Poisson equation:

$$\nabla^2\psi = 2\,\kappa(\boldsymbol{\theta}) \,. \tag{3.8}$$

Gravitational lensing not only shifts the light path in the simple way presented above. The deflection of light is differential and that creates an observed image which deviates from that of the source. The value of the surface brightness should however remain conserved, as the number of photons is not perturbed by the deflection and following the reasoning of Liouville's Hamiltonian theorem. Nevertheless, the incoming flux of observed light is changed due to its dependence on angular span. The flux of the source image can be defined as $S = \mu(\boldsymbol{\theta})S_0$, with S_0 being the original source flux and μ the so-called magnification of the image. The magnification is naturally dependent on the variation of the separation β with the angular scale:

$$\mu = |\det A(\boldsymbol{\theta})|^{-1} \quad with \quad A(\boldsymbol{\theta}) = \frac{\partial \boldsymbol{\beta}}{\partial \boldsymbol{\theta}}\,. \tag{3.9}$$

$A(\boldsymbol{\theta})$ effectively characterises the distortions of the observed image of the source and these are described by the following symmetric Jacobian matrix:

$$\begin{aligned} A &= \left(\delta_{ij} - \frac{\partial^2 \psi}{\partial \theta_i \partial \theta_j}\right) &(3.10)\\ &= \begin{pmatrix} 1-\kappa-\gamma_1 & -\gamma_2 \\ -\gamma_2 & 1-\kappa+\gamma_1 \end{pmatrix}. &(3.11)\end{aligned}$$

Here we introduce parameter γ, which depicts the shear of the image:

$$\gamma \equiv \gamma_1 + \mathrm{i}\gamma_2 = |\gamma|\, e^{2\mathrm{i}\phi} \tag{3.12}$$

we the shear components γ_1 and γ_2 described by:

$$\gamma_1 = \frac{1}{2}\left(\psi_{,11} - \psi_{,22}\right) \quad \text{and} \quad \gamma_2 = \psi_{,12}\,. \tag{3.13}$$

The magnification of the source image will then be given by:

$$\mu = \frac{1}{(1-\kappa)^2 - |\gamma|^2} \tag{3.14}$$

while the inverse eigenvalues of A provide the information on its shape: if the source original image is circular, the eigenvalues give the ratio between the axis of an ellipse, which will be the shape of the lensed image. The lines defined by the values for which the determinant of matrix A is null represent critical curves which, in the source plane, correspond to so-called caustics. The closer the light gets to the caustics, the more deformed will be the shape of the image.

As a conclusion, one acknowledges two kinds of distortions of the source radiation by gravitational lensing: the change in the size of the image and the change in the shape of the image relative to that of the source. Next, we briefly discuss the usefullness and some of the applications of these effects.

3.1.2 Gravitational lensing phenomenology

The characteristics of the gravitational lensing phenomenon provide the a practical source of information for several cosmological studies. Lensing is measured through a projected quantity, dependent only on the luminosity and composition of the lens. This effect is highly dependent on the mass content of the source and therefore particularly suitable for detecting and studying the distribution of dark matter in the Universe and growth of collapsed structures. As the observed images get magnified through the deflection, that makes them easier to access even if they belong to remote regions of the Universe which would otherwise remain undetectable (see, e.g. Zheng et al. (2012)). Although it is a rather serendipitous effect as one cannot control where to look through a "lens", it is nonetheless very useful when identified. Moreover, as the effect depends intrinsically on redshift, distance and age of sources and lenses, these properties provide a way

Figure 3.2: Hubble Telescope Image of Abell 370, example of strong gravitational lensing by a galaxy cluster. Image credits: NASA, ESA, the Hubble SM4 ERO Team, and ST-ECF.

to study and constrain cosmological parameters, the Hubble constant or the general characteristics of the source distribution in space and time.

This said, we turn to how the gravitational lensing study field can be sub-divided in three main kinds of phenomena, each of which depends on the scale where the effect occurs. Here we summarise the most important facts about each of these observation classes.

■ **Strong Lensing** As mentioned in the previous section, the occurrence of surface densities equal or above its critical value create powerful lenses. The observational consequences of this kind of lenses are the ones for which gravitational lensing is most well know - the arcs. Figure 3.2 shows an example of this manifestation. The shapes of the observable distortions in the presence of strong gravitational lensing vary depending on how foreground (lens) and background (source) objects are aligned with respect to the observer, so depending on the distance to the caustic lines mentioned previously. In the extreme case when observer, lens and and extended source are all aligned by the optical axis, the giant arcs created by a sufficiently massive deflector might form a circle known as Einstein ring. For point-like sources (e.g. quasars), the distortion creates multiple images instead.

Strong manifestations of gravitational lensing are sources of information for a variety of tasks in cosmological studies. The intrinsic dependence of the gravitational lensing phenomenon on the mass of the deflector object is used to study and quantify its dark-matter distribution (see, e.g. Kochanek and Narayan (1992)). This is done by modelling the relation between the deflection angle and the lens mass for a given observation. Another possible use is the determination of the Hubble constant through the gravitational lensing of variable sources (see Refsdal (1964)): the different lensed images are produced with a time shift that is proportional to the difference in light path lengths and this is proportional to the inverse of the H_0.

■ **Microlensing** On the low-mass end of the scale of gravitational lenses are the microlensing events. These refer to the deflection of light by small objects as stars and are therefore transitional phenomena. The analysis of the magnification of the image of a galactic object by an inner-galactic dark halo occasionally positioned in between the source and the observer can provide information on the distribution and content of mass within the Galaxy (Paczynski 1986). Moreover, in recent years, this technique has proved to be valuable on the detection of extra-solar planets (Albrow et al. 1995; Wambsganß 1997; Sumi et al. 2011). When a star that is being observed through a lens is part of a planetary system, it is possible that a planet happens to position itself between the observer and source. Then, little but measurable changes occur in light-curve, leading to the detection and further characterisation of the planet.

■ **Weak Lensing** When a case of strong gravitational occurs, not only evident distortions are taking place. Smaller distortions of background sources are often observable too, as noticeable in Figure 3.2. These subtle shape deviations classify the lensing manifestation as weak. Common weak gravitational lensing studies deal with the set-up of a massive foreground object placed in front of an ensemble of background sources, from which a series of subtle distortions appears. The inspection of these weakly deformed images allows a statistical evaluation of the dark-matter distribution, which we will proceed with next.

Furthermore, weak gravitational lensing can be used together with strong lensing to more accurately study the distribution of dark matter in massive deflectors. Cluster mass reconstruction with information on these two scales is a very active field at present time (see, e.g. Merten et al. (2009) or Bradač et al. (2006)).

The cross-correlation work presented in this thesis deals with the dark matter distribution and its relation to the signal from baryonic origin in large-scale structures such as galaxy clusters. The choice of weak gravitational lensing presented itself as the most promising source of such information. Extensive reviews with considerably more detail on this subject can be found in e.g. Bartelmann and Schneider (2001) or Refregier (2003).

3.1.3 The weak lensing power spectrum

The weak gravitational lensing effect is commonly described by the convergence parameter κ. This parameter is directly related to the measurable shear, reflected in the observable distortions of the galaxies, as both quantities depend on the second derivatives of the deflection potential (see relations (3.13)):

$$\kappa(\boldsymbol{\theta}) = \frac{1}{2}\left(\frac{\partial^2\psi(\boldsymbol{\theta})}{\partial\theta_1^2} + \frac{\partial^2\psi(\boldsymbol{\theta})}{\partial\theta_2^2}\right) \tag{3.15}$$

which in Fourier space are simply related in the following way:

$$\hat{\kappa}(\mathbf{k}) = -\frac{1}{2}\left(k_1^2 + k_2^2\right)\hat{\psi}(\mathbf{k}) \tag{3.16}$$

$$\hat{\gamma}_1(\mathbf{k}) = -\frac{1}{2}\left(k_1^2 - k_2^2\right)\hat{\psi}(\mathbf{k}) \tag{3.17}$$

$$\hat{\gamma}_1(\mathbf{k}) = -k_1 k_2\,\hat{\psi}(\mathbf{k})\,. \tag{3.18}$$

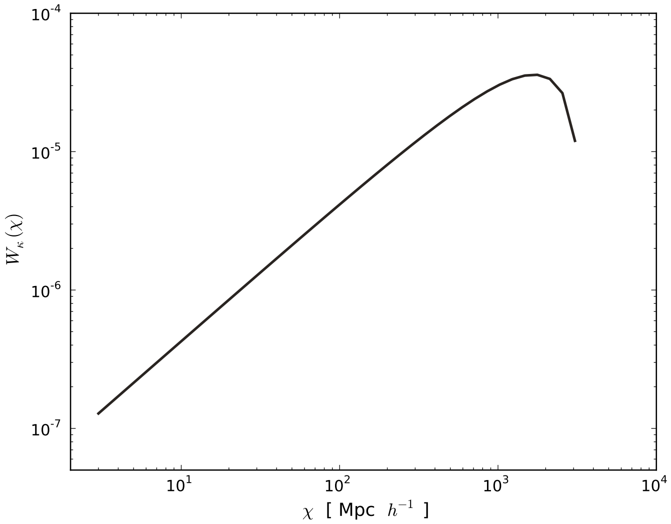

Figure 3.3: Geometrical weight function of the convergence parameter.

After the shear is observed, Eqs. (3.17) and (3.18) are solved for the potential. The two solutions are combined by a minimal-variance estimation. Using relation (3.16), the convergence can then be expressed in terms of a convolution of the shear:

$$\kappa(\boldsymbol{\theta}) = \frac{1}{\pi} \int \mathrm{d}^2\theta' \, \mathrm{Re} \left(D^*(\boldsymbol{\theta} - \boldsymbol{\theta}') \gamma(\boldsymbol{\theta}') \right) \tag{3.19}$$

where D is the complex convolution kernel given by:

$$D(\boldsymbol{\theta}) = \frac{(\theta_2^2 - \theta_1^2) \; 2\mathrm{i}\theta_1\theta_2}{\theta^4} \tag{3.20}$$

and the shear is described as a complex variable as defined in 3.12.

To easily describe the convergence, we can alternatively return to Eq.(3.8) which stipulates a direct relation between κ and the gravitational potential. The potential and the density contrast δ are related by the Poisson equation (1.37). The convergence becomes:

$$\kappa = \frac{3\Omega_\mathrm{m} H_0}{2c^2} \int \mathrm{d}\chi \, \frac{\chi - \chi_s}{\chi_s} \, \frac{\chi}{a} \, \delta = \int \mathrm{d}\chi \; W_\kappa(\chi) \, \delta. \tag{3.21}$$

The distortion level depends of the Hubble constant H_0, the matter density Ω_m and the speed of light c. The integral along co-moving distances is performed over the considered matter distribution through a dimensionless source field, the density contrast δ:

$$\delta = \frac{\rho - \bar{\rho}}{\bar{\rho}} \tag{3.22}$$

and weighted geometrically by the relation:

$$W_\kappa(\chi) = \frac{3\Omega_\mathrm{m} H_0}{2c^2} \, \frac{\chi - \chi_\mathrm{s}}{\chi_\mathrm{s}} \, \frac{\chi}{a} \tag{3.23}$$

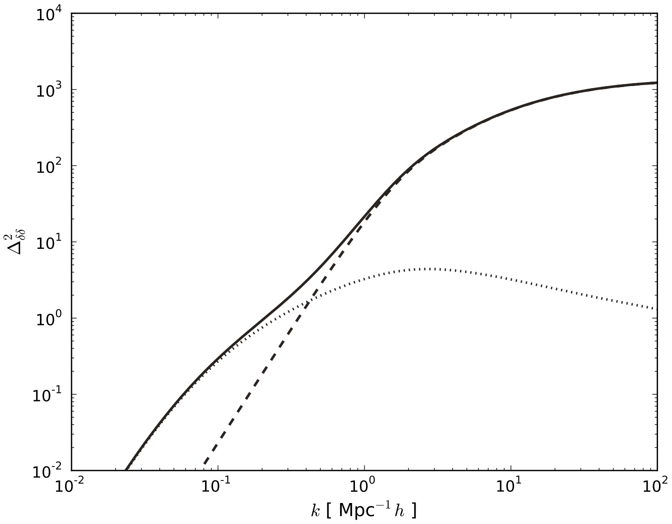

Figure 3.4: Three-dimensional power spectrum of density contrast at redshift 0. Solid line shows the total power spectrum as the result of adding the contributions from the 1-halo term (dashed line) and the 2-halo term (dotted line).

where $\chi_{\rm s}$ is the co-moving distance to the source and a is the scale factor and behaves as shown in Figure 3.3. This geometrically weighs the integral along the line-of-sight by averaging over the source distances. The weight function peaks at the scale of highest lensing efficiency.

The parameterisation of the convergence in the second step of Eq. (3.21) with a weight function and a source field is done with the intention of applying the same method for different signals in a consistent and practical way. This criterion will be used in the next section as well.

Applying the halo model formalism to the weak gravitational lensing phenomenon is rather straight forward. Eqs. (2.10) and (2.11) can be directly used to calculate the power spectrum of the field that is in the origin of the shear/convergence:

$$P_{\delta\delta}(k,z) = P^{\rm 1h}_{\delta\delta}(k,z) \; + \; P^{\rm 2h}_{\delta\delta}(k,z). \tag{3.24}$$

The models chosen to build the dark-matter power spectrum within the halo framework were: the Sheth & Tormen mass function for $n(m)$, the NFW halo profile for normalised Fourier transform density $u(k,m)$ and the Mo & White model for the bias parameter $b(m)$. The linearly evolved primordial power spectrum is computed according to the calculations by Bardeen et al. (1986).

The input of these ingredients in the above-mentioned equations yields the 3-dimensional power spectrum of the density contrast shown in Figure 3.4. The power is presented as a dimensionless quantity, the power spectrum per logarithmic interval in wavenumber, $\Delta = k^3\ P(k)/2\pi^2$. The curves for redshift 0 indicate that both halo terms show the same level of contribution to the total spectrum on relatively large scales, $k \sim 10^{-1}$, below which single halos clearly dominate the source of power revealing its strong dependence on the density profiles chosen. On the other hand, for very large scales, the Poisson term is slightly dominated by halo-halo correlation, mostly influenced by the bias parameter. This result for redshift 0 is in good agreement with those of Cooray (2000) and Cooray and Sheth (2002), where an identical method was used. The total curve amplitudes and the scale dependence of the 1- and 2-halo terms are

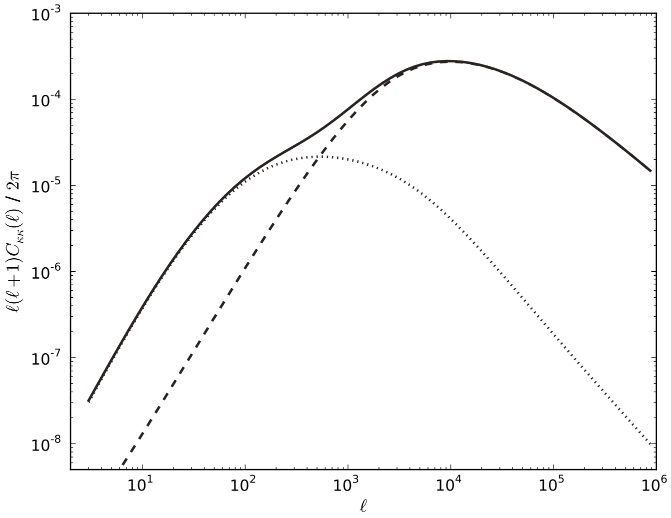

Figure 3.5: Convergence power spectrum, integrated from redshift 0 to 1. Scheme follows that from Figure 3.4.

reasonably similar. Amplitude disparities on the small scale level are related to the implementation of a different halo mass-concentration relation in those works.

The 3-dimensional power spectrum is a valuable result when it comes to testing theory against simulations. The projection of the power spectrum into an angular quantity allows the comparison between theoretical predictions and observations. We apply Limber's approximation (see Appendix) to compute the convergence power spectrum from the density contrast 3-dimensional result. Using the flat-sky approximation and setting the wavenumber as $k = \ell/\chi$, where ℓ is the Fourier position in the sky, we get:

$$C_{\kappa\kappa}(\ell) = \int_0^{\chi_s} \frac{\mathrm{d}\chi}{\chi^2}\, W_\kappa^2(\chi)\, P_{\delta\delta}(\ell/\chi, \chi) \tag{3.25}$$

Figure 3.5 shows the convergence power spectrum integrated from redshift 0 to 1 (meaning that the maximum value of the co-moving distance corresponds to putting the source at $\chi_s = \chi(z = 0)$. The shape of the spectrum is in good agreement with the many studies which can be found in the literature. As the projection is mostly a geometrical weighting of the 3-dimensional counterpart, there are no intense changes in the contribution level of each halo term from the dark-matter power spectrum. The decrease of power on smaller scales reflects the smaller structures ($\sim$ below 1 arcmin) do not contribute as significantly to the overall lensing signal.

3.2 Baryonic physics and the Sunyaev-Zel'dovich effect

The journey of cosmic microwave background (CMB) photons through the Universe can be perturbed in several ways. Gravitational potential fluctuations created by the presence of the web-like large scale structure, composed by dark-matter halos connected by filaments, host most of the Universe's baryonic content. The high-temperature, ionised gas present in these dense regions is responsible for the scattering of the CMB photons through the inverse Compton process, causing a measurable distortion of the CMB's black-body spectrum. This effect, first predicted by Sunyaev and Zel'dovich (1970) and widely observed ever since, forms a powerful probe for the presence of hot baryonic matter.

First observed in the early 1980s, the strongest of the secondary sources of CMB anisotropies has become a reliable and fertile method to study the baryonic content of the Universe and other cosmological subjects of interest. Besides tracing the hot gas in large-scale structures, the unique characteristics of the SZ effect make it suitable to constrain cosmological models, estimate distances or the Hubble constant, all this while not intrinsically depending on the redshift of the sources.

In this section we address the method we use to evaluate the gas component of halos and how it may be useful to constrain cosmological parameters or the evolution of temperature in galaxy clusters. We first introduce the basics of the scattering of photons by a non-relativistic population of electrons and briefly characterise the sub-types of the SZ effect. The ending part of this chapter describes the thermal SZ effect within the halo model framework. For further detail on the SZ effect, the reader is referred to reviews in the literature such as Rephaeli (1995), Birkinshaw (1999) or Carlstrom et al. (2002).

3.2.1 Inverse Compton scattering

The early-20th-century works of Compton on the scattering of X-rays (Compton 1923a,b), following the discovery of the photo-electric effect by Einstein a few years before, describe the simple but fundamental way of how matter and radiation interact. His results showed how a distribution of hot, ionised gas exchanges energy when in contact with photons.

The left panel of Figure 3.6 shows the process known as Compton scattering, an inelastic interaction between a stationary electron and a low-energy photon. The electron receives energy from the photon, whose energy is reduced. The conservation of energy-momentum allows the calculation of the energy shift in the photons when scattered by an electron:

$$\varepsilon' = \frac{\varepsilon}{1 + \frac{\varepsilon}{m_e c^2}\left(1 - \cos\phi_{12}\right)} \tag{3.26}$$

with ϕ_{12} being the angle difference between the incoming and outgoing photon trajectories. ε and ε' are the initial and final energies of the photon, respectively.

Alternatively, one may consider the encounter of a low-energy photon with a high-energy electron. What results from that interaction, under the same assumption of energy-momentum conservation, is the increase of frequency of the photon resulting from an energy transfer by the electron, which loses momentum (right panel of Figure 3.6). This process describes what happens to the CMB photons when they come across distributions of high-energy electrons of the hot, ionised gas trapped in the potential wells of the large-scale structure as filaments and galaxy clusters. Usual analyses include estimating the scattering probability. It is also possible to extend this description to the scattering of a photon spectrum by a given gas distribution which can in turn be used to estimate the intensity of the scattered radiation.

In this work, we present the results of the spectral changes in an electron distribution where no relativistic arguments are considered. In most cases of inverse Compton scattering, to consider a non-relativistic population of electrons is enough to accurately describe the processes involved in the origin of the SZ effect. In most galaxy clusters, the energies do not rise much above the few keV. Energies of about

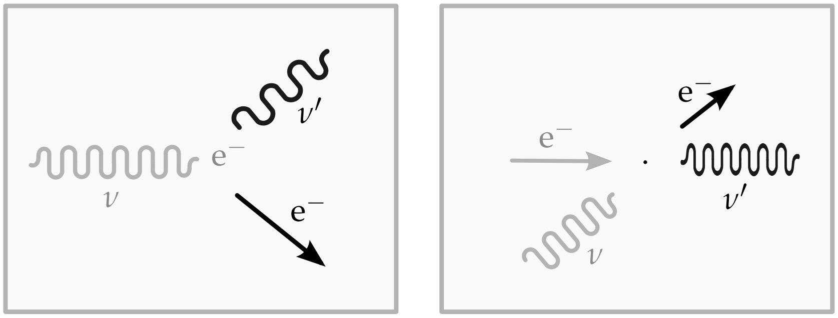

Figure 3.6: On the left: illustration of the Compton scattering. A photon interacts with a low-energy electron at rest. The electron gains the energy lost by the photon ($\nu' < \nu$). On the right: the SZ effect basic mechanism, the inverse Compton scattering. In this case, a low energy photon encounters a high-energy electron and the exchange increases the frequency of the photon ($\nu' > \nu$) while decreasing the energy of the electron.

an order of magnitude higher are necessary for relativistic corrections to become pertinent. For details on this topic see, e.g., conclusion of Section 3.4 in the review by Birkinshaw (1999).

For our purposes, we consider that taking the non-relativistic approach (that the electron energy $\hbar\nu \ll m_\mathrm{e}c^2$) is sufficient and adequate. The short description of the photon spectral dependence lightly follows that presented in, e.g., Weinberg (2008). Consider a gas distribution with a certain photon occupation number N. The Kompaneets equation (Kompaneets 1956, 1957) states that, when Compton scattering occurs, N varies at the following rate:

$$\frac{\partial N}{\partial t} = \frac{n_\mathrm{e}\,\sigma_\mathrm{T}}{m_\mathrm{e}\,c\,\nu^2}\,\frac{\partial}{\partial \nu}\,\left[k_\mathrm{B}\,T_\mathrm{e}\,\nu^4\,\frac{\partial N}{\partial \nu} + \hbar\,\nu\,N\,(1+N)\right] \tag{3.27}$$

where ν is the photon frequency, σ_T is the Thompson cross-section, $m_\mathrm{e}c^2$ corresponds to the electron rest mass, $\hbar$ is the reduced Planck constant, n_e is the electron gas density and T_e its temperature. Considering that N is a function of frequency ν and line-of-sight depth ℓ, and the density and temperature are additionally only dependent of ℓ, the above relation can be re-written simply as:

$$\frac{\partial N}{\partial \ell} = \frac{n_\mathrm{e}(\ell)\,T_\mathrm{e}(\ell)\,k_\mathrm{B}\sigma_\mathrm{T}}{m_\mathrm{e}c^2\nu^2}\,\frac{\partial}{\partial \nu}\left[\nu^4\,\frac{\partial N}{\partial \nu}\right] \tag{3.28}$$

Re-arranging this equality, we get an expression for the variation of N:

$$\Delta N(\nu) = \frac{y}{\nu^2}\,\frac{\partial}{\partial \nu}\left[\nu^4\,\frac{\partial N}{\partial \nu}\right] \tag{3.29}$$

which depends on the so-called Comptonization parameter here introduced:

$$y \equiv \frac{\sigma_\mathrm{T} k_\mathrm{B}}{m_\mathrm{e}c^2}\int \mathrm{d}\ell\, n_\mathrm{e}(\ell)\, k_\mathrm{B}(\ell)\, T_\mathrm{e}(\ell) \tag{3.30}$$

For a black-body radiation with a temperature $\bar{T}$, the photon occupation number is given by:

$$N = \left(\exp^{-1}\left(\hbar\nu/k_\mathrm{B}\bar{T}\right)\right)^{-1} \tag{3.31}$$

and its variation can be re-written to yield the spectral shape of the electron population:

$$\Delta N = y\,\left(\frac{-x + (x^2/4)\,\cot(x/2)}{\sinh^2(x/2)}\right) \tag{3.32}$$

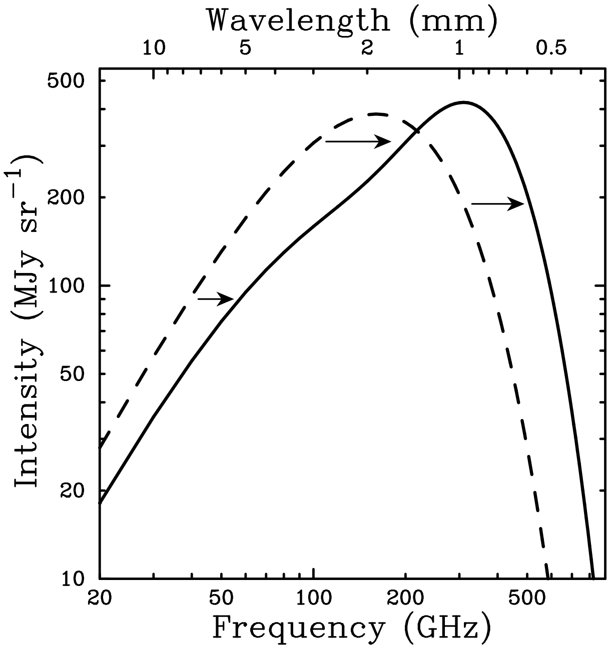

Figure 3.7: The initial CMB spectrum (dashed line) is shifted towards higher energies due to the thermal SZ effect. The result is a decrease of intensity on lower frequencies (the Rayleigh-Jeans regime) and an increase of intensity at higher frequencies (Wien regime). Here, an exaggerated case is shown with the considered cluster being approximately 1000 times more massive than a typical such object. Plot reprinted from Carlstrom et al. (2002).

with $x \equiv \hbar\nu/k_\mathrm{B}\bar{T}$ as the dimensionless frequency/energy. This particular spectral shape makes it easy to identify the SZ effect anisotropy and distinguish it from the underlying CMB radiation. In the limit of very small energies ($x \ll 1$), the Rayleigh-Jeans regime:

$$\Delta N \to \frac{-2y}{x} \quad \text{and} \quad N \to \frac{1}{x} \tag{3.33}$$

meaning a decrement in the low-energy part of the spectrum. Alternatively, in the Wien regime ($x \gg 1$), the energy is increased. The thermal-SZ effect creates a lateral shift towards higher energies and there is a transitional point at which the initial and final spectra show the same intensity (see Figure 3.7.) Another practical property becomes evident from the above relations. The shape of the black-body spectrum is preserved:

$$\frac{\Delta\bar{T}}{\bar{T}} = \frac{\Delta N}{N} = -2y\,. \tag{3.34}$$

and so, reliably easy to identify and select from the overall CMB radiation.

Although this is the phenomenon we are interested in for our study, the very robust SZ effect is not confined to thermal events. Next, we give a brief overview of the different types of the Sunyaev-Zel'dovich effects and how they are practical resources to probe a whole range of different cosmological fields.

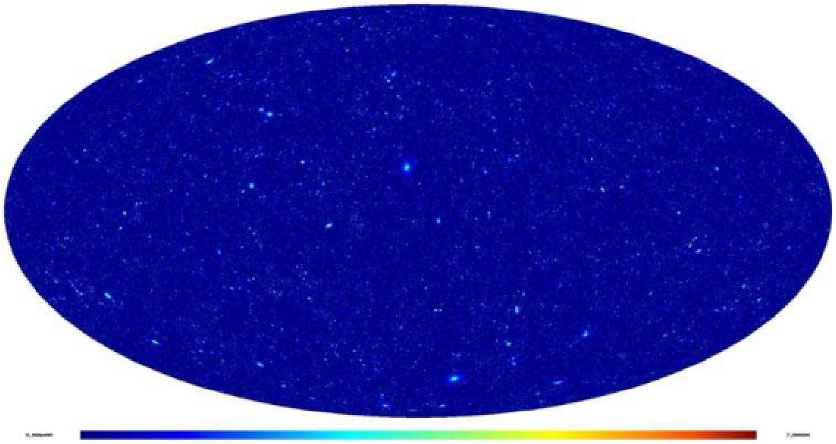

Figure 3.8: Simulated all-sky map of the thermal SZ effect for the Planck mission showing a cluster distribution as well as tracing some filamentary structures. The colour-scale is proportional to $\mathrm{arcsinh}(10^6 \times y)$. Image from Schäfer et al. (2006).

3.2.2 The Sunyaev–Zel'dovich effects and applications

The Sunyaev-Zel'dovich effect – the scattering of CMB photons by the hot ionised gas of large-scale structure – provides a useful and effective method to trace the distribution of baryonic matter in the Universe. This property and the fact that the Comptonisation parameter is a projected measurement (and therefore relatable to the weak gravitational lensing observable) makes it a desirable tool for our study.

Measurements of these events have been performed in the radio, microwave and X-ray wavelengths. Many experiments have been conducted until present day (Wilkinson Microwave Anisotropy Telescope (WMAP), Planck Mission, South Pole Telescope (SPT), Atacama Cosmology Telescope (ACT)), given the robustness and maturity of the method, as well as the increasing technology advances in the detection field. For an extensive review of the employed techniques, we once again refer the reader to the descriptions in Birkinshaw (1999) or Carlstrom et al. (2002).

Here we assess the scope of phenomenology associated with the photon scattering by hot cluster gas and the distinct applications of these sub-effects to the study of baryons.

The thermal SZ effect

After describing the SZ effect formalism from the Kompaneets equation, we have all the tools to characterise the thermal SZ effect: signal originated by thermal interaction of large reservoirs of ionised gas and the crossing of CMB photons. Figure 3.8 shows a simulated all-sky map by Schäfer et al. (2006) of the kind of signal distribution that should be observable with the Planck Surveyor (the actual data results will be published in early 2013). The signal is dominated by the most massive clusters in the sky. The paradigmatic characteristic of this effect is that the observable, the y-Compton parameter, shows no direct dependence on the redshift, making it a particularly suitable tool to study the redshift evolution of structures. The claim of redshift independence does however not take into account how the measurement techniques in spatially unresolved observations – beam-smoothing effects – do indeed depend on the redshift. Further, the thermal SZ effect is a useful source of information on the number density of structures.

Although this can be achieved with X-ray emission, the near independence of the SZ effect on redshift makes it less vulnerable to the diminution of signal because of the distance of clusters. Because the hot electrons in the ionised gas produce X-ray radiation and this measurable signal depends proportional on the square of the electron density, one can combine it with the intensity of the SZ-signal. This allows the elimination of the electron density term and the consequent description of a distance relation which provides a method to estimate the Hubble constant H_0. This parameter is found to depend mostly on the CMB temperature shift and the X-ray determined cluster temperature. The investigation of the intra-cluster medium properties is improved by the dependence of the thermal SZ effect on the electron temperature and density of clusters. Moreover, the very amount of baryonic matter within the dark matter halos that enclose galaxy clusters can be estimated via this effect.

■ **The kinetic SZ effect** The motion of the high-temperature and ionised gas in relation to the CMB radiation also produces distortions in its spectrum and such features are different than those created by the thermal SZ effect. The shift occurs in the same fashion as a Doppler-shift and it is evaluated through the optical depth of the gas distribution, which depends on the Thomson cross-section σ_{T} and electron density n_{e} and has a spectral signature different than that accompanying the Compton parameter. The overall temperature shift depends primarily on the optical depth and the peculiar velocity of the considered object, while it does not depend on the frequency. The kinetic SZ effect was first established in literature by Sunyaev and Zel'dovich (1972); Sunyaev and Zeldovich (1980) and causes very subtle and difficult to detect changes in the spectrum. It was only this year that the attempts to trace the kinetic SZ effect started to be successful (Hand et al. 2012). The estimation of the peculiar velocities of clusters can, for example, be supplemented by observations of gravitational lensing, which provides estimates on the value of other velocity components, given insight on the large-scale structure dynamics.

■ **Polarization** The SZ effect signal can additionally be show polarisation since the CMB irradiating from clusters is partially polarised. Also first referred to in Sunyaev and Zeldovich (1980), this effect depends strongly on cluster optical depths and may be useful to estimate its value. The polarisation of the SZ effect is responsible for a very faint and difficult to detect signal and requires the super-positioning of many clusters along the line-of-sight in order to expect a measurable signal.

3.2.3 The thermal SZ effect power spectrum

The thermal SZ effect is most commonly described by the Compton-y parameter as shown earlier in this section. We here reproduce and re-arrange the terms in the following line-of-sight integral:

$$y = g(x) \int \mathrm{d}\chi \, a \, \frac{k_{\mathrm{B}}\sigma_{\mathrm{T}}}{m_{\mathrm{e}}c^2} \, T_{\mathrm{e}} n_{\mathrm{e}} = \int \mathrm{d}\chi \, W_y(\chi) \, \zeta \tag{3.35}$$

The function $g(x)$ contains the dependence of the effect on the dimensionless frequency $x = h\nu / k_{\mathrm{B}}T$ where ν is the frequency at which temperature T is measured, h and k_B are the Planck and Boltzmann constants, respectively. In our study we consider $g(x)$ to be -2, corresponding to the limit of the Rayleigh-Jeans regime where $h\nu \ll k_{\mathrm{B}}T$. Although we make this assumption, our implementation is not bound to a particular part of the CMB spectrum and can be used in a general way. Given the fact that the Compton parameter is not more than the projection of the gas density times the temperature, one can define a dimensionless source field as the relative perturbation of the pressure:

$$\zeta = \frac{n_\mathrm{e} T_\mathrm{e}}{\bar{n}_\mathrm{e} \bar{T}_\mathrm{e}} \tag{3.36}$$

with the barred parameters corresponding to the mean electron density of the Universe $\bar{n}_\mathrm{e}$ and a mean value for the temperature of an ionised gas $\bar{T}_\mathrm{e}$. We assume $k_\mathrm{B}\bar{T}_\mathrm{e} = 1$ keV and define the mean electron density of the Universe:

$$\bar{n}_\mathrm{e} = \frac{f_\mathrm{b}\, \rho_\mathrm{critical}}{\mu\, m_\mathrm{p}}\,. \tag{3.37}$$

Here f_b is the baryon fraction, ρ_critical is the cosmological critical density, μ gives the effective mass of a particle releasing one electron and m_p is the proton rest-mass.

We define the remaining non-fluctuating terms as a weight function along the line-of-sight:

$$W_y(\chi) = 2\, a(\chi)\, \frac{k_\mathrm{B}\sigma_\mathrm{T}}{m_\mathrm{e}c^2}\, \bar{n}_\mathrm{e}\bar{T}_\mathrm{e}. \tag{3.38}$$

At this point, we have defined two quantities in a formally similar way. Both the convergence and the Compton-y parameter describe essentially the projected values of the two complementary fields we wish to study. In both cases, the defined source terms and weight functions have matching dimensions and therefore play similar parts in the evaluation of both weak lensing and the SZ effect. In the next sections, we show how they can be studied jointly and provide us with knowledge on the correlation level between dark and baryonic matter.

The halo model framework can be used to estimate the power spectrum of the gas-pressure density field ζ. Eqs. (2.10) and (2.11) are here reproduced with the few changes required to assess the baryon distribution instead of the dark-matter component of a halo:

$$P^{1\mathrm{h}}_{\zeta\zeta}(k,z) = \int \mathrm{d}m \left(\frac{m}{\bar{\rho}}\right)^2 n(m,z)\, u^2_\mathrm{gas}(k,m)\, t(m,z) \tag{3.39}$$

$$\begin{aligned} P^{2\mathrm{h}}_{\zeta\zeta}(k,z) = P_\mathrm{lin} &\int \mathrm{d}m_1\, \frac{m_1}{\bar{\rho}}\, n(m_1,z)\, u_\mathrm{gas}(k,m_1)\, t(m_1,z)\, b(m_1) \\ &\int \mathrm{d}m_2\, \frac{m_2}{\bar{\rho}}\, n(m_2,z)\, u_\mathrm{gas}(k,m_2)\, t(m_2,z)\, b(m_2). \end{aligned} \tag{3.40}$$

New in this description is the normalised Fourier transform of the baryon distribution u_gas and a normalised mass-temperature relation.

To model the distribution of baryonic matter in the halos, we use the β-profile to define the density distribution of electrons n_e. This simple model is described by:

$$n_\mathrm{e}(r,m) = \frac{n_\mathrm{e0}}{\left(1 + (r/r_\mathrm{c})^2\right)^{3\beta/2}} \tag{3.41}$$

where n_e0 describing the normalisation of the density and r_c being the core radius. Throughout this study, we always use $\beta = 1$.

To calculate the normalised Fourier transform of the electron density, we use Eq. (2.20) from the previous chapter. For this value of β, the Fourier transform of n_e does not have an analytical solution, hence we

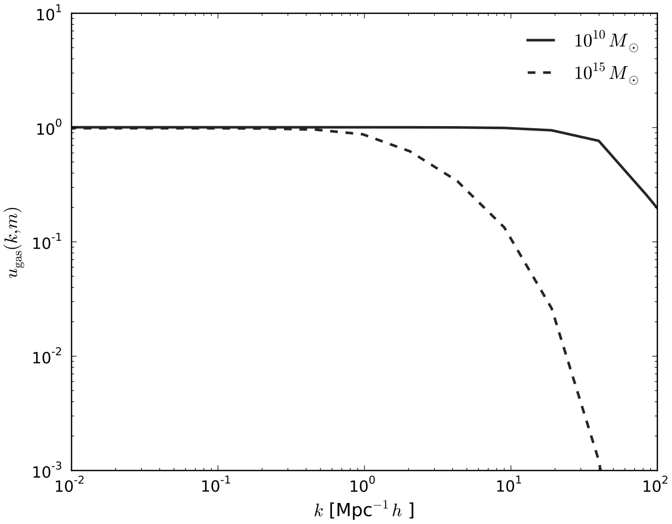

Figure 3.9: Normalised beta profile and its dependence on the halo mass at redshift zero. Value of β is 1.

compute it numerically. Setting $R := r/r_{\rm c}$:

$$\int \mathrm{d}^3\mathbf{x}\; n_{\rm e}(\mathbf{x},m)\, e^{\mathrm{i}\mathbf{k}.\mathbf{x}} = \frac{4\,\pi\, n_{\rm e0}}{k} \int_0^{R_{\rm vir}} \mathrm{d}R\; R\; \sin(kRr_{\rm c})\; \left(1+R^2\right)^{-3/2} . \tag{3.42}$$

On the other hand, the normalisation of the transform (which corresponds to counting the total number of electrons within the halo) can be analytically determined:

$$\int \mathrm{d}^3\mathbf{x}\; n_{\rm e}(\mathbf{x},m) = 4\,\pi\, r_{\rm c}^3 \int_0^{R_{\rm vir}} \mathrm{d}R\; R^2\; \left(1+R^2\right)^{-3/2} \tag{3.43}$$

$$= 4\,\pi\, r_{\rm c}^3 \left(\ln\left(R_{\rm vir} + \sqrt{R_{\rm vir}^2+1}\right) - \frac{R_{\rm vir}}{\sqrt{R_{\rm vir}^2+1}} \right) \tag{3.44}$$

To ensure that the density profile falls to zero at some point, as to avoid computational problems, we force the distribution to have a smooth decrease after a sufficiently large radius. For that purpose, we use the SPH smoothing kernel used in the GADGET-2 code by Springel (2005). The normalised gas density profile is shown in Figure 3.9 for different mass values.

In order to calculate the temperature profile of the gas distribution, we use a simple power-law model for the temperature. For each halo mass, the temperature starts at a minimum temperature plateau and increases with mass and redshift:

$$t(m,z) = \frac{t_{\rm min}}{t_0} + (1+z) \left(\frac{m}{m_0}\right)^{2/3} . \tag{3.45}$$

We use as normalisation temperature $t_0 = 1.16 \times 10^7$ K as it is a typical value to ensure ionisation and as minimum temperature $t_{\rm min} = 1.46 \times 10^7$ K, corresponding to the temperature of a cluster of mass $m_0 = 10^{14} M_\odot$. The remaining ingredients are used as stated for the computation of the power spectrum of the dark matter distribution.

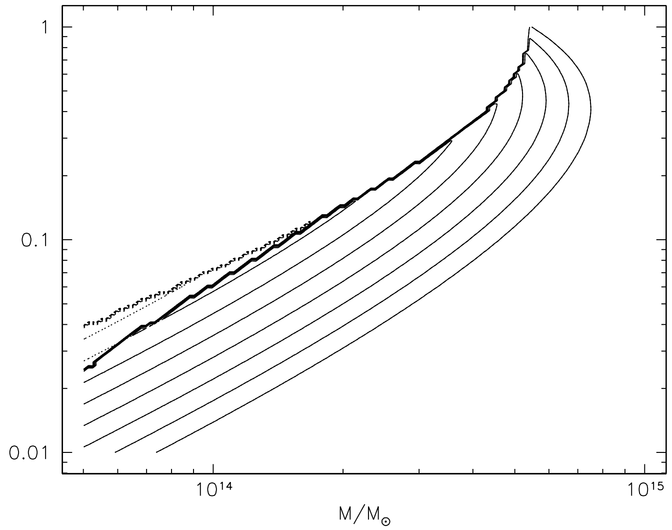

Figure 3.10: Mass-redshift distribution of detectable clusters with Planck. Contours depict the number density of observable clusters and are logarithmically spaced by 0.2 decimal points; the lowest contour corresponds to a number density of $10^{-10.5} {M_\odot}^{-1}$. The dotted contours do not take into account beam convolution nor noise from background fluctuations. In this work, we constrain our mass-redshift integration to the limits inferred from this result. Plot reprinted from Bartelmann (2001).

Additionally, the mass integration is performed in accordance to the mass-redshift cut-offs corresponding to observable-only halos, as described in Bartelmann (2001) and shown in Figure 3.10. This means that for a given redshift, only the potentially measurable halos in a given mass range are taken into account. The effect of a beam is the smoothing of the overall SZ signal, wiping out the low signal peaks. The smoothing is strongest at the low mass and low redshift regime. The beam smoothing will decrease beyond the redshift ~ 1.25, where the angular-diametre distance peaks and all clusters massive enough to be seen at that redshift can be seen throughout the Universe.

Figure 3.11 shows the resulting total power and the contributions from single halos and inter-halo correlations, at redshift 0. The contribution from single halos is the clear dominating source of power on scales smaller than $k \sim 0.2$ while in the large-scale regime, most of the signal comes from halo-halo correlations. The drop of power at the small end of the scales occurs as after a certain size, no matter how massive the halo is, it will become too small to be resolved – as the result of the mass cut explained above – and thus will not contribute to the signal.

With the computed 3-dimensional power spectrum of the baryon distribution, it is easy to compute its projection, the Sunyaev-Zel'dovich power spectrum, again using Limber's and the flat-sky approximations as in Section 3.1.3:

$$C_{yy}(\ell) = \int \frac{\mathrm{d}\chi}{\chi^2} \, W_y^2(\chi) \, P_{\zeta\zeta}(\ell/\chi, \chi) \tag{3.46}$$

The tendency observed at large-scales of the 3-dimensional power spectrum is not present after the projection. As shown in Figure 3.12, where the power spectrum is integrated from 0 to $\chi(z = 1)$ the single-halo contribution becomes the most important source of signal to the total curve on all scales. As

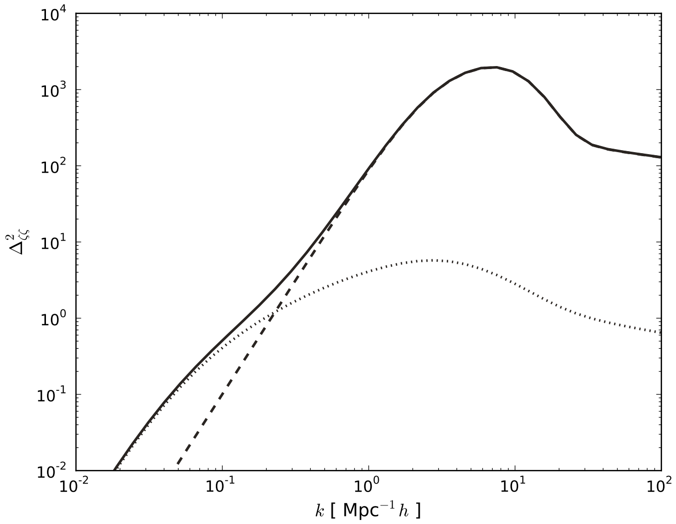

Figure 3.11: Three-dimensional power spectrum of gas pressure distribution at redshift 0. Solid line depicts the total power, dashed and dotted lines correspond to the 1- and 2-halo contributions.

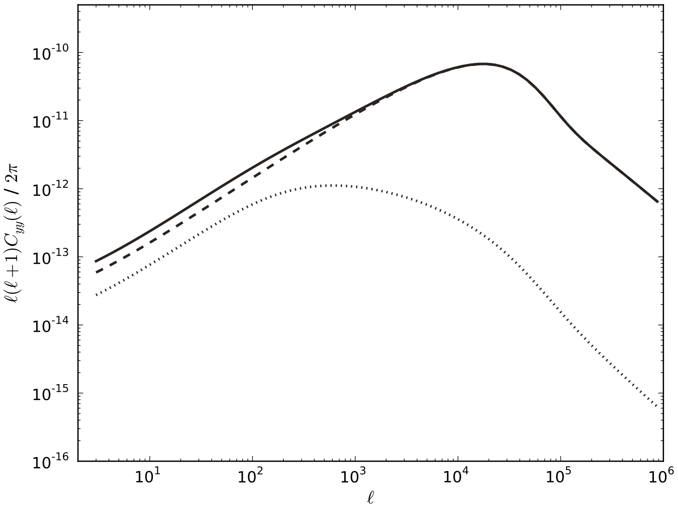

Figure 3.12: Sunyaev-Zel’dovich effect (angular) power spectrum, integrated from redshift 0 to 1. The line-style scheme is the same as in Figure 3.11.

one integrates over large volumes of the Universe, the halo-halo correlation becomes less relevant. The reason why this effect doesn't reflect in the weak gravitational lensing power spectrum is related to how the the geometrical weight functions of Limber's approximation shape the signal. A narrower peak of the lensing weight function case infers a larger contribution of halo-halo correlations.

Chapter 4

The cross-correlation

In the previous chapters we presented the background upon which we define the Universe and how the signal from cosmological sources it can be analytically characterised through the halo model. We furthermore revealed the phenomena we wish to correlate in the hope that the result will shed light on the properties and history of the large-scale structure. Now that our method is presented and all main ingredients are introduced, we are ready to estimate the cross-correlation signal between the weak gravitational lensing and the thermal Sunyaev-Zel'dovich effect.

Section 4.1 recovers the most important aspects of the process of calculating the cross-correlation power spectrum, recalls the assumptions on models and parameters which are taken to compute it and shows the results for both the 3-dimensional power spectrum and its projection. With the latter quantity, we define and determine the correlation function in Section 4.2, from which follows the detailed calculation of the covariance matrix of the cross-correlation power spectrum in Section 4.3.

4.1 The cross-power spectra

The first goal of this work was to successfully specialise the halo model to compute the cross-correlation of interest. Here we show the cross-correlation power spectra between the weak gravitational lensing signal tracing the dark matter distribution in halos and their gas content originating the thermal SZ effect. In the present section, we display the derived expressions and the outcome obtained for the 3-dimensional and angular power spectra by specialising the halo model formalism from Chapter 2 via the results from Chapter 3. Our results should, to some extent, match those of Cooray (2000) or Cooray and Sheth (2002). Differences are expected to arise as we use a different parameterisation of the gas halo density and the normalisation methods are not the same as implemented here. Also, the arbitrary way we calibrate the temperature-mass relation might be a source of disagreement.

4.1.1 3-dimensional spectrum

The auto-correlation spectra of dark-matter and baryon fields are computed directly from Eqs. (2.10) and (2.11) by assigning specific density distributions. $u_{\mathrm{DM}}(k,m)$ and $u_{gas}(k,m)$ with mass-temperature relation $t(m,z)$ respectively set the normalised Fourier-transformed dark matter and electron gas density profiles with a normalised temperature function. The cross-correlation between the dark-matter density fluctuations that create weak gravitational lensing, and the gas density that ultimately gives rise to the thermal SZ effect can be theoretically evaluated by use of a specialised version of the same set of equations, as presented in the following power spectra:

$$P^{1\mathrm{h}}_{\delta\zeta}(k,z) = \int \mathrm{d}m \left(\frac{m}{\bar{\rho}}\right)^2 n(m,z) u_{\mathrm{DM}}(k,m) u_{gas}(k,m) t(m,z) \tag{4.1}$$

$$\begin{aligned} P^{2\mathrm{h}}_{\delta\zeta}(k,z) = \frac{P_{\mathrm{lin}}}{2} &\int \mathrm{d}m_1 \, \frac{m_1}{\bar{\rho}} \, n(m_1,z) \, u_{\mathrm{DM}}(k,m_1) \, u_{gas}(k,m_2) \, t(m_2,z) \, b(m_1) \\ &\int \mathrm{d}m_2 \, \frac{m_2}{\bar{\rho}} \, n(m_2,z) \, u_{\mathrm{DM}}(k,m_2) \, u_{\mathrm{gas}}(k,m_1) \, t(m_1,z) \, b(m_2) \end{aligned} \tag{4.2}$$

with all variables as defined in previous chapters. In our experiment with the halo formalism, we consider a set of assumptions regarding the halo-model ingredients. Here we briefly summarise the models already presented in Chapters 2 and 3. Throughout this work, we assume:

- $n(m,z)$: for the mass function we use the Sheth-Tormen model (Sheth and Tormen 1999), which takes into account elliptical collapse of structures and very well fits numerical simulation results;

- u_{DM}: we choose the NFW (Navarro et al. 1997) profile to characterise the dark matter density distribution. This model is empirically motivated and the computation of the normalised Fourier transform, where the integration is done up to the virial radius, is fully analytical;

- u_{gas}: we take the conventional isothermal β profile to describe baryonic densities. The Fourier transform requires an integration up to the virial radius. The result is not fully analytical and a smooth decrease to zero is added to the gas density, borrowing the properties of the smoothing kernel of the GADGET-2 code (Springel 2005). We adopt a $\beta = 1$;

- $t(m,z)$: the gas temperature is taken to depend on the halo mass as a simple power law of the kind $t(m,z) \propto m^{2/3}(z+1)$ with an arbitrary initial plateau of the order of 10^7K to ensure gas ionisation;

- $b(m,z)$: the biasing level is computed as in Mo and White (1996);

- P^{lin}: the linear power spectrum is obtained by evolving the initial perturbations with the transfer function of Bardeen et al. (1986);

- *Cosmological parameters*: we use the standard ΛCDM model with the seven-year WMAP results (Komatsu et al. 2011), where parameters are estimated through the combination of CMB and BAO data as well as external measurements of the Hubble parameter. Most importantly: matter density $\Omega_m = 0.227$, dark energy density $\Omega_\Lambda = 0.728$, baryon density $\Omega_{\mathrm{b}} = 0.0456$, Hubble constant $H_0 = 70.4$ kms^{-1}Mpc^{-1} and fluctuation amplitude $\sigma_8 = 0.809$.

- *Mass integration*: while performing the mass integration in the calculation of the 3-dimensional power spectrum, we restrict the mass-redshift plane so that only halos that are observable via both weak gravitational lensing and Sunyaev-Zel'dovich effect are taken into account. This follows the work by Bartelmann (2001).

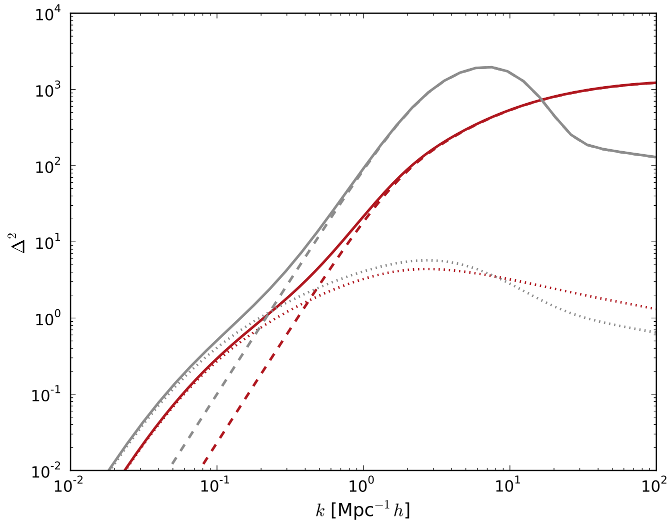

Figure 4.1: Three-dimensional power spectrum of the density contrast (in red) and gas pressure (in black) distributions at redshift 0. Dashed lines correspond to 1-halo terms and dotted lines depict the signal from halo-halo correlations.

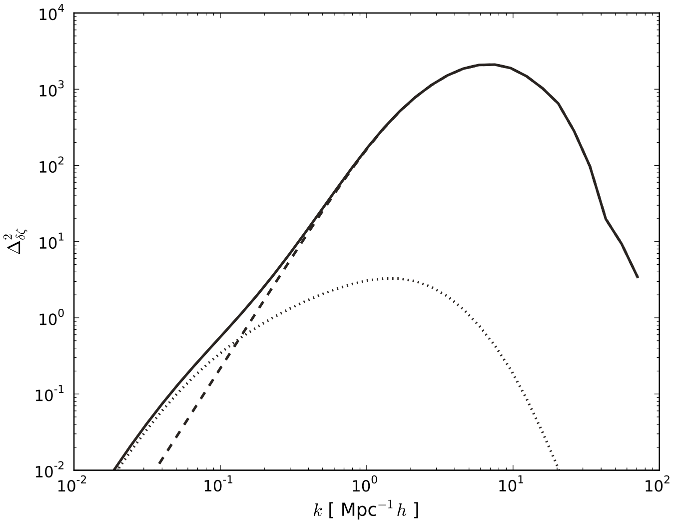

Figure 4.2: Three-dimensional power spectrum of the cross-correlation between dark matter density contrast and gas pressure, at redshift 0. Solid line shows the total power as the sum of the 1-halo term (dashed curve) and 2-halo term (dotted curve).

Figures 4.1 and 4.2 show the three-dimensional auto- and cross-power spectra of dark matter and hot gas at redshift zero, respectively, for the total signal and its one- and two-halo terms contributions.

We re-plot the auto-correlation curves to more closely compare the different features of the dark and baryonic signals, which is relevant to better understand the cross-correlation behaviour. For all signals, the single halo contribution is dominant for the most part of the scale range and the clustering term is mainly relevant at the larger scales. The strong dependence on the 1-halo term as small angular scales is related to how influential is the choice of density model whereas the dominance of the halo-halo correlations in the large scales point to the importance of having an adequate bias model. Only at scales of the order of $k \sim 10^{-1}$ do both halo terms show the same amount of contribution to the signal.

The cross-correlation spectra are more similarly shaped to that of the gas pressure than the dark matter signal, which makes the former seem to bear the strongest features when compared to the latter.

Our results for the 3-dimensional power spectra of auto- and cross-correlation are in general good agreement with those of Cooray (2000) and Cooray and Sheth (2002), where an identical method was used. Minor differences are likely the result from the different choices of inputs other than those picked for the present study, i.e. mainly the model for gas-density profile and the cosmological parameters. Overall, the total curve amplitudes and the scale dependence of the 1- and 2-halo terms are reasonably similar.

The power spectrum obtained in this way provides a valuable tool for the comparison of a theoretical result with that of numerical simulations. The next section will yield the projection of this spectrum, which in turn gives a signal directly comparable to observations.

4.1.2 Angular spectrum

The 3-dimensional description of the signal is directly comparable to results from cosmological simulations. In order to be able to directly test theoretical predictions of the signal with actual observational data it is required that those predictions are projected onto the sky.

To compute the projected two-point correlation function, in Fourier space, we again use Limber's approximation (Limber 1954), according to which the statistics of a given projected quantity can be obtained by integrating over the statistical description of its three-dimensional counterpart. We once more take the flat-sky approximation and set the wavenumber as $k = \ell/\chi$, with ℓ as the Fourier angular position.

Thus, given the power spectrum of the three-dimensional field calculated in the previous section and the definitions of the two effects we aim to cross-correlate – see Eqs. (3.21) and (3.35) – it is rather straightforward to project our results into the angular power spectrum based on the above-mentioned assumption:

$$C_{\kappa\kappa}(\ell) = \int \frac{\mathrm{d}\chi}{\chi^2}\, W_\kappa^2(\chi)\, P_{\delta\delta}(\ell/\chi, \chi) \tag{4.3}$$

$$C_{\kappa y}(\ell) = \int \frac{\mathrm{d}\chi}{\chi^2}\, W_\kappa(\chi)\, W_y(\chi)\, P_{\delta\zeta}(\ell/\chi, \chi)\,. \tag{4.4}$$

These are line-on-sight integrals with all the parameters as previously defined. We choose to extend our integration along co-moving distances up to a source at $\chi_\mathrm{s} = \chi(z = 1)$ because the lensing efficiency peaks at a lower redshift, after which structures become too small to contribute to the overall signal.

Figures 4.3 and 4.4 show the auto- and cross-correlation angular power spectra of/between the weak lensing convergence and the thermal SZ effect, respectively, with total signal (solid line) and halo terms.

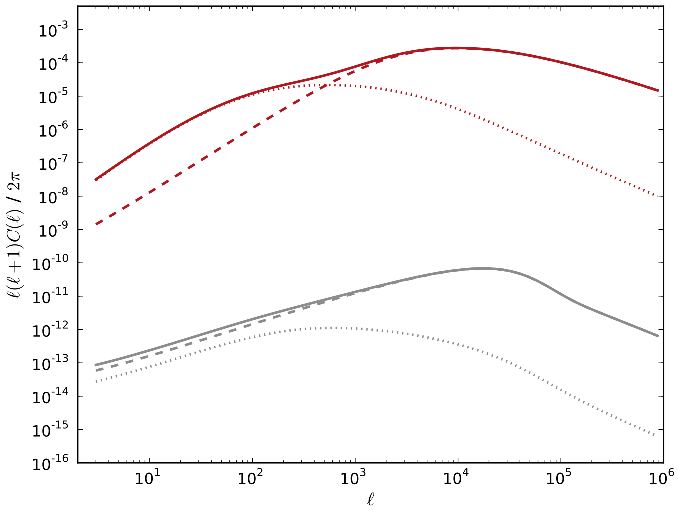

Figure 4.3: Angular power spectra of weak lensing convergence and the SZ effect integrated up to redshift 1. Colour and line-style schemes follow those of Figure 4.1.

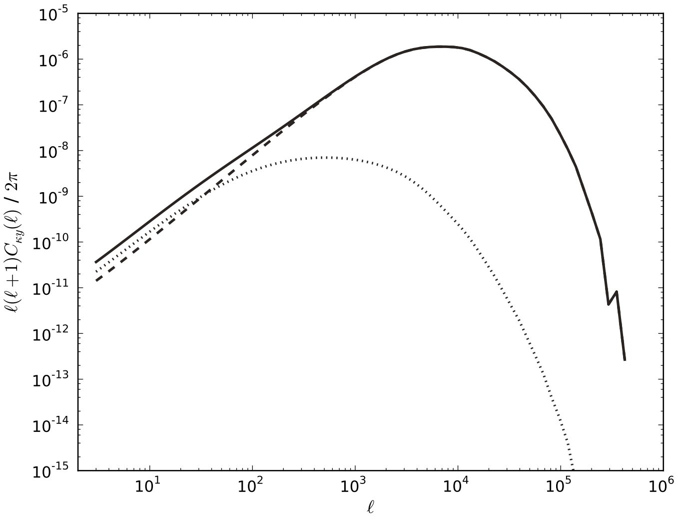

Figure 4.4: Cross-correlation (weak gravitational lensing and the SZ effect) angular power spectrum, integrated from redshift 0 to 1. Line-style is the same as in Figure 4.2.

The auto-correlation spectra are here reproduced once again for the same reasons specified in the previous section: it is easier to compare the amplitudes and shapes of both spectra and infer which signal and scale has the most influence the final cross-correlation curves.

Regarding the cross-power, we observe a minimal contribution of the cross-correlation two-halo term (dotted line) to the total power at low multipole orders, to a total signal otherwise strikingly dominated by the contributions from individual halos (dashed line). After a peak in the cross-correlation at a multipole order near $\ell \sim 10^4$, the value decreases steeply towards smaller scales mainly due to the most massive, and therefore rare, halos, as dictated by the mass function.

In the remaining sections we continue with the statistical evaluation of the angular power spectrum by investigating the limits of correlation and detection for a given survey.

4.1.3 Substructure in the cross-correlation between dark matter and gas

We investigated the effect of introducing substructure into the halo description. However, early results did not seem to add any useful or strikingly different information to that already obtained with the original halo model. Accordingly, we continue our study without a detailed characterisation of the matter distribution interior to the halo.

4.2 Correlation function of the power spectrum

We start our statistical analysis of the cross-correlation signal by leaving the Fourier formalism and returning to the real space. The second-order measurements are computed by assuming that the signal is measured by averaging the convergence and the Compton parameter over circular apertures of radius θ. Either signal is assumed to be convolved with a top-hat beam. This means we are filtering the signal with a quite broad window function, allowing us to probe the correlation level in a wide range of angles and, most importantly, to potentially measure a substantial amount of signal.

In this effort, we follow Schneider et al. (2002) and references therein, using the formalism applied to the computation of the shear dispersion measurements to define the correlation function with an integrand which depends linearly on the angular cross-correlation power spectrum calculated in the previous section:

$$\xi(\theta) = \int_0^\infty \frac{\mathrm{d}\ell\,\ell}{2\pi}\,\frac{4\,J_1^2(\ell\theta)}{(\ell\theta)^2}\,C_{\kappa y}(\ell) \tag{4.5}$$

where J_1 is the Bessel function of the first kind and order 1. It arises from the convolution of the power spectrum with a top-hat filter. Although choosing different convolution profiles would return different functions, the results wouldn't change significantly. This calculation yields Fig. 4.5 where the correlation function of the total weak lensing/SZ cross-correlation power spectrum integrated from redshift 0 to 1 is shown.

As the correlation function is just the conversion of the Fourier space angular power spectrum quantity into the real space, the overall behaviour of the signal is not profoundly changed: the cross-correlation level is higher at smaller scales and lower for large angles.

We follow the definition of the correlation function with the calculation of the covariance matrix of the power spectrum which will provide the errors of our estimations.

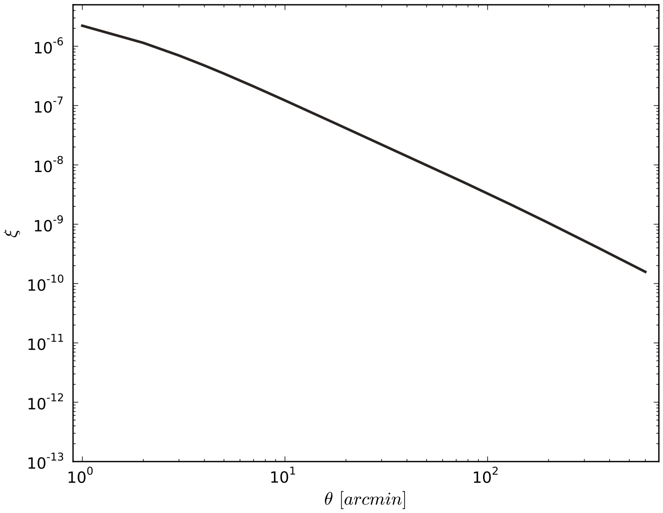

Figure 4.5: Cross-correlation function between weak lensing and the SZ effect.

4.3 Covariance matrix of the correlation function and correlated errors

In this section, we will use the framework shown in Joachimi et al. (2008) to compute the covariance matrix of our cross-correlation power spectrum. Although the reasoning behind this method is similar to that of the shear estimation, we need to adapt the formalism to our particular case of having two different observables: the shear and the Compton parameter. Following this method, we first define the signal estimators and subsequently derive the power spectrum estimator. This is the one ingredient necessary to the calculation of the covariance matrix which then becomes possible. In the end, some words are devoted to how correlated errors are computed from the covariance matrix. We thoroughly present our calculations in order to make all steps clear and free-of-doubt.

4.3.1 Definitions: signal estimators

■ **Weak Lensing** Take $\varepsilon := \gamma + \epsilon^{\mathrm{s}}$ as an estimator of the shear γ, with ϵ^{s} being the intrinsic ellipticity of an observed galaxy and therefore a source of noise to the lensing signal. We consider the estimator to be unbiased since averaging over all angles yields:

$$\langle \varepsilon \rangle = \langle \gamma \rangle + \langle \epsilon^{\mathrm{s}} \rangle = \langle \gamma \rangle \tag{4.6}$$

The Fourier transform of the shear estimator is given by:

$$\begin{aligned}\hat{\varepsilon} &= \sum_{i=1}^{N} \varepsilon_i \, e^{i\bar{\ell}.\bar{\theta}_i} \\ &= \sum_{i=1}^{N} \gamma_i \, e^{i\bar{\ell}.\bar{\theta}_i} + \sum_{i=1}^{N} \epsilon_i \, e^{i\bar{\ell}.\bar{\theta}_i} \\ &= \int \mathrm{d}^2\theta \, \sum_{i=1}^{N} \delta^{(2)}(\bar{\theta} - \bar{\theta}_i) \, \gamma(\bar{\theta}) \, e^{i\bar{\ell}.\bar{\theta}} + \sum_{i=1}^{N} \epsilon_i \, e^{i\bar{\ell}.\bar{\theta}_i} \qquad (4.7)\end{aligned}$$

where ε_i and θ_i are the ellipticity and position of the i-th galaxy, respectively. ℓ corresponds to the Fourier conjugate of the position in the sky. Shear is measured within circular apertures but it can be described as a continuous field which is the reason for the appearance of the delta function in the following definition:

$$n(\bar{\theta}) := \sum_{i=1}^{N} \delta^{(2)}(\bar{\theta} - \bar{\theta}_i). \qquad (4.8)$$

Separately carrying out the above integral:

$$\begin{aligned}\int \mathrm{d}^2\theta \, n(\bar{\theta}) \, \gamma(\bar{\theta}) \, e^{i\bar{\ell}.\bar{\theta}_i} &= \int \mathrm{d}^2\theta \int \frac{\mathrm{d}^2\ell_1}{(2\pi)^2} \int \frac{\mathrm{d}^2\ell_2}{(2\pi)^2} \, \hat{n}(\bar{\ell}_1) \, e^{-i\bar{\ell}_1.\bar{\theta}} \, \hat{\gamma}(\bar{\ell}_2) \, e^{-i\bar{\ell}_2.\bar{\theta}} \, e^{i\bar{\ell}.\bar{\theta}} \\ &= \int \frac{\mathrm{d}^2\ell_1}{(2\pi)^2} \int \frac{\mathrm{d}^2\ell_2}{(2\pi)^2} \, \hat{n}(\bar{\ell}_1) \, \hat{\gamma}(\bar{\ell}_2) \int \mathrm{d}^2\theta \, e^{i(\bar{\ell}-\bar{\ell}_1-\bar{\ell}_2).\bar{\theta}} \\ &= \int \frac{\mathrm{d}^2\ell_1}{(2\pi)^2} \int \frac{\mathrm{d}^2\ell_2}{(2\pi)^2} \, \hat{n}(\bar{\ell}_1) \, \hat{\gamma}(\bar{\ell}_2) \, (2\pi)^2 \, \delta(\bar{\ell} - \bar{\ell}_1 - \bar{\ell}_2) \\ &= \int \frac{\mathrm{d}^2\ell_2}{(2\pi)^2} \, \hat{n}(\bar{\ell} - \bar{\ell}_2) \, \hat{\gamma}(\bar{\ell}_2) \\ &= \int \frac{\mathrm{d}^2\ell'}{(2\pi)^2} \, \hat{n}(\bar{\ell} - \bar{\ell}') \, \hat{\gamma}(\bar{\ell}') \, . \qquad (4.9)\end{aligned}$$

With this result, the shear estimator in Fourier space is finally given by:

$$\hat{\varepsilon}(\bar{\ell}) = \int \frac{\mathrm{d}^2\ell'}{(2\pi)^2} \, \hat{n}(\bar{\ell} - \bar{\ell}') \, \hat{\gamma}(\bar{\ell}') \; + \; \sum_{i=1}^{N} \epsilon_i \, e^{i\bar{\ell}.\bar{\theta}_i} \qquad (4.10)$$

with $\hat{n}(\bar{\ell}) = \int \mathrm{d}^2\theta \, n(\bar{\theta}) \, e^{i\bar{\ell}.\bar{\theta}} = \sum_{i=1}^{N} e^{i\bar{\ell}.\bar{\theta}_i}$. Its ensemble average is:

$$\begin{aligned}\left\langle \hat{n}(\bar{\ell}) \right\rangle &= \left\langle \sum_{i=1}^{N} e^{i\bar{\ell}.\theta_i} \right\rangle = \sum_{i=1}^{N} \left\langle e^{i\bar{\ell}.\theta_i} \right\rangle \\ &= N \left\langle e^{i\bar{\ell}.\theta_i} \right\rangle = \; N \, \frac{1}{A} \int_A \mathrm{d}^2\theta \, \Pi(\bar{\theta}) \, e^{i\bar{\ell}.\bar{\theta}} \qquad (4.11)\end{aligned}$$

Here, the survey area is given by A and N is the number of galaxies at a position θ_i. Further:

$$\Pi(\bar{\theta}) = \begin{cases} 1 & \text{in survey area} \\ 0 & \text{outside} \end{cases} \qquad (4.12)$$

so that $A = \int_A \mathrm{d}^2\theta \, \Pi(\bar{\theta})$. The Fourier transform of the aperture is then given by

$$\hat{\Pi}(\bar{\ell}) = \int_{\mathrm{I\!R}} \mathrm{d}^2\theta \, \Pi(\bar{\theta}) \, e^{i\bar{\ell}.\bar{\theta}} = \int_A \mathrm{d}^2\theta \, \Pi(\bar{\theta}) \, e^{i\bar{\ell}.\bar{\theta}} \qquad (4.13)$$

For $\sqrt{A} \gg 2\pi/\ell$:

$$\int_A \mathrm{d}^2\theta\, \Pi(\bar{\theta})\, e^{i\bar{\ell}.\bar{\theta}} \longrightarrow (2\pi)^2\, \delta(\bar{\ell}) \tag{4.14}$$

This result yields that $\langle \hat{n}(\bar{\ell}) \rangle = \bar{n}\, \hat{\Pi}(\bar{\ell})$ is, in this regime, given by

$$\langle \hat{n}(\bar{\ell}) \rangle = (2\pi)^2 \bar{n} \delta(\bar{\ell}) \tag{4.15}$$

Up to this point, we have just repeated the calculations performed by Kaiser (1998).

Sunyaev-Zel'dovich effect The definition of the SZ effect is rather easier to assess than that of the weak gravitational lensing. We define a SZ measurement as $\eta := y + n_y$ where y is the intrinsic Compton parameter and n_y is the noise contributed by unresolved clusters. Additionally, we assume that the noise contribution is a non-vanishing one:

$$\langle \eta(\bar{\theta}) \rangle = \langle y(\bar{\theta}) \rangle + n_y(\bar{\theta}) \tag{4.16}$$

$\langle \eta(\bar{\theta}) \rangle$ is a biased estimator.

4.3.2 Estimator of the cross-correlation power spectrum

Having calculated the shear and Compton parameter estimators, respectively Eqs. (4.10) and (4.16), and the average of the aperture distribution given by Eq. (4.15), we are now ready to compute the estimator cross-correlation power spectrum for weak lensing and the Sunyaev-Zel'dovich effect. The calculation follows:

$$\begin{aligned}
\langle \hat{\varepsilon}(\bar{\ell}) \hat{\eta}(\bar{\ell}')^* \rangle &= \left\langle \left[\int \frac{\mathrm{d}^2\ell'}{(2\pi)^2}\, \hat{n}(\bar{\ell} - \bar{\ell}')\, \hat{\gamma}(\bar{\ell}') + \sum_{i=1}^{N} \epsilon_i\, e^{i\bar{\ell}.\bar{\theta}_i} \right] \left[\hat{y}^*(\bar{\ell}) + \hat{n}_y^*(\bar{\ell}) \right] \right\rangle \\
&= \int \frac{\mathrm{d}^2\ell'}{(2\pi)^2} \langle \hat{n}(\bar{\ell} - \bar{\ell}') \rangle \langle \hat{\gamma}(\bar{\ell}')\, \hat{y}^*(\bar{\ell}) \rangle \\
&\quad + \int \frac{\mathrm{d}^2\ell'}{(2\pi)^2} \langle \hat{n}(\bar{\ell} - \bar{\ell}') \rangle \left\langle \hat{\gamma}(\bar{\ell}')\, \hat{n}_y^*(\bar{\ell}) \right\rangle .
\end{aligned} \tag{4.17}$$

At this point, we assumed that the intrinsic ellipticities from shear measurements do not correlate with any of the components of the SZ effect observations, i.e. $\left\langle \epsilon_i^{\mathrm{s}}\, \hat{y}^* \right\rangle = 0 = \left\langle \epsilon_i^{\mathrm{s}}\, \hat{n}_y^* \right\rangle$. However, even though they are not individually accounted by SZ measurements, unresolved sources might produce a lensing signal, meaning that a cross-correlation term in between weak lensing and SZ noise is needed to fully describe the power spectrum. Using the result from (4.15) we continue the calculation:

$$\begin{aligned}
\langle \hat{\varepsilon}(\bar{\ell}) \hat{\eta}(\bar{\ell}')^* \rangle &= \bar{n} \int \mathrm{d}^2\ell'\, \delta(\bar{\ell} - \bar{\ell}') \langle \hat{\gamma}(\bar{\ell}')\, \hat{y}^*(\bar{\ell}) \rangle \\
&\quad + \bar{n} \int \mathrm{d}^2\ell'\, \delta(\bar{\ell} - \bar{\ell}') \left\langle \hat{\gamma}(\bar{\ell}')\, \hat{n}_y^*(\bar{\ell}) \right\rangle \\
&= \bar{n}\, (2\pi)^2\, \delta(0) \left[P_{\gamma y} + P_{\gamma n_y} \right] \\
&= A\bar{n} \left(P_{\gamma y} + P_{\gamma n_y} \right)
\end{aligned} \tag{4.18}$$

with, $(2\pi)^2\delta(\bar{\ell}) = \int \mathrm{d}^2\theta e^{i\bar{\ell}.\bar{\theta}}$ so that $(2\pi)^2\delta(0) = A$. The above results allow the definition of an unbiased estimator for the cross-correlation power spectra:

$$\tilde{P}_{\gamma y} := \frac{1}{A\bar{n}} \langle \hat{\varepsilon}\hat{\eta}^* \rangle - P_{\gamma n_y} \, . \tag{4.19}$$

4.3.3 Covariance of the cross-correlation power spectrum

We have now all the necessary ingredients to compute the covariance of the power spectrum. We have defined an unbiased power spectrum estimator $\tilde{P}$, i.e. $\langle \tilde{P} \rangle = P$, so the covariance is given by:

$$\mathrm{Cov} = \langle (\tilde{P} - P)(\tilde{P} - P)' \rangle - PP' \, . \tag{4.20}$$

Applying this expression to our particular case using the result of Eq. (4.19) , we get:

$$\begin{aligned} \mathrm{Cov} &= \left\langle \left[\frac{1}{A\bar{n}} \langle \hat{\varepsilon}\hat{\eta}^* \rangle - P_{\gamma n_y} \right] \left[\frac{1}{A\bar{n}} \langle \hat{\varepsilon}\hat{\eta}^* \rangle - P_{\gamma n_y} \right]' \right\rangle - P_{\gamma y} P'_{\gamma y} \\ &= \frac{1}{(A\bar{n})^2} \left\langle \hat{\varepsilon}\hat{\eta}^* \hat{\varepsilon}' \hat{\eta}'^* \right\rangle + P_{\gamma n_y} P'_{\gamma n_y} \\ &\quad - \frac{1}{A\bar{n}} \left(\langle \hat{\varepsilon}\hat{\eta}^* \rangle P'_{\gamma n_y} + \left\langle \hat{\varepsilon}' \hat{\eta}'^* \right\rangle P_{\gamma n_y} \right) - \, P_{\gamma y} P'_{\gamma y} \, . \end{aligned} \tag{4.21}$$

According to Wick's theorem, we can decompose the four-point correlation of the first term:

$$\left\langle \hat{\varepsilon}\hat{\eta}^* \hat{\varepsilon}' \hat{\eta}'^* \right\rangle = \left\langle \hat{\varepsilon}\hat{\eta}^* \hat{\varepsilon}' \hat{\eta}'^* \right\rangle_c + \langle \hat{\varepsilon}\hat{\eta}^* \rangle \left\langle \hat{\varepsilon}' \hat{\eta}'^* \right\rangle + \left\langle \hat{\varepsilon}\hat{\varepsilon}' \right\rangle \left\langle \hat{\eta}^* \hat{\eta}'^* \right\rangle + \left\langle \hat{\varepsilon}\hat{\eta}'^* \right\rangle \left\langle \hat{\varepsilon}' \hat{\eta}^* \right\rangle \tag{4.22}$$

where the subscript 'c' indicates the connected four-point correlator which we here assume to be negligible. We are then left with terms concerning two-point correlators only. These are related to power spectra $P_{\mathrm{x}} = P_{\mathrm{x}}(\ell)$, with the index 'x' refering to the correlated fields and given by the following expressions:

$$\begin{aligned} \langle \hat{\varepsilon}\hat{\eta}^* \rangle &= A\bar{n} \left(P_{\gamma y} + P_{\gamma n_y} \right) & (4.23) \\ \langle \hat{\varepsilon}\hat{\eta}'^* \rangle &= (2\pi)^2 \, \delta(\ell - \ell') \, \bar{n} \left(P_{\gamma y} + P_{\gamma n_y} \right) & (4.24) \\ \langle \hat{\varepsilon}\hat{\varepsilon}' \rangle &= (2\pi)^2 \, \delta(\ell + \ell') \, \bar{n}^2 \, P_{\gamma\gamma} + \bar{n}\sigma_\epsilon^2 \, (2\pi)^2 \, \delta(\ell + \ell') & (4.25) \\ \langle \hat{\eta}^* \hat{\eta}'^* \rangle &= (2\pi)^2 \, \delta(\ell + \ell') \, (P_{yy} + P_{n_y n_y}) \, . & (4.26) \end{aligned}$$

with σ_ϵ corresponding to the dispersion of intrinsic ellipticities. Introducing these equalities in expression (4.21), we obtain:

$$\begin{aligned} \mathrm{Cov} = \frac{1}{(A\bar{n})^2} \Big[& (A\bar{n})^2 (P_{\gamma y} + P_{\gamma n_y})(P_{\gamma y} + P_{\gamma n_y})' \\ & + \big((2\pi)^2 \, \delta(\ell + \ell') \, \bar{n}^2 \, P_{\gamma\gamma} \\ & \quad + \bar{n}\sigma_\epsilon^2 \, (2\pi)^2 \, \delta(\ell + \ell') \big) (2\pi)^2 \, \delta(\ell + \ell') \, (P_{yy} + P_{n_y n_y}) \\ & + \Big((2\pi)^2 \, \delta(\ell - \ell') \, \bar{n} (P_{\gamma y} + P_{\gamma n_y}) \Big)^2 \Big] \\ + P_{\gamma n_y} P'_{\gamma n_y} & - \left(P_{\gamma y} + P_{\gamma n_y} \right) P'_{\gamma n_y} - \left(P_{\gamma y} + P_{\gamma n_y} \right)' P_{\gamma n_y} - P_{\gamma y} P'_{\gamma y} \, . \end{aligned} \tag{4.27}$$

Carrying out the calculation a little further, we are left with a covariance which is the sum of two terms. One term corresponds to the product of the auto-correlation spectra of weak lensing and SZ effect and the other hosts the cross-correlation power spectrum:

$$\begin{aligned} \mathrm{Cov} = \frac{1}{(A\bar{n})^2} \Big[&\left((2\pi)^2 \, \delta(\ell + \ell') \, \bar{n}^2 \, P_{\gamma\gamma} + \bar{n}\sigma_\epsilon^2 \, (2\pi)^2 \, \delta(\ell + \ell') \right) \cdot \\ &(2\pi)^2 \, \delta(\ell + \ell') \, (P_{yy} + P_{n_y n_y}) \Big] \\ + &\frac{1}{(A\bar{n})^2} \left((2\pi)^2 \, \delta(\ell - \ell') \, \bar{n} (P_{\gamma y} + P_{\gamma n_y}) \right)^2 \; . \end{aligned} \tag{4.28}$$

Averaging over ℓ-bands, the covariance becomes:

$$\begin{aligned} \int_{A_\ell} \mathrm{d}^2\ell \int_{A_{\ell'}} \mathrm{d}^2\ell' \; \mathrm{Cov} = & \frac{1}{(A\bar{n})^2} \int \frac{\mathrm{d}^2\ell}{A_\ell} \int \frac{\mathrm{d}^2\ell'}{A_{\ell'}} \Big[(2\pi)^4 \, \delta^{(2)}(\ell + \ell') \, \bar{n}^2 \, P_{\gamma\gamma} \\ & + \; (2\pi)^4 \, \bar{n} \, \sigma_\epsilon^2 \, \delta^{(2)}(\ell + \ell') \Big] \cdot (P_{yy} + P_{n_y n_y}) \\ & + \frac{1}{(A\bar{n})^2} \int \frac{\mathrm{d}^2\ell}{A_\ell} \int \frac{\mathrm{d}^2\ell'}{A_{\ell'}} \left((2\pi)^2 \, \delta(\ell - \ell') \, \bar{n} (P_{\gamma y} + P_{\gamma n_y}) \right)^2 \; . \end{aligned} \tag{4.29}$$

For the covariance of the cross-power not to be zero, $\ell = \ell'$ must be satisfied. Furthermore, the transformation $\ell \to -\ell'$ should not change the result if the bands are defined by the modulus of the wave vector. Given that $(2\pi)^2 \, \delta(0) = A$, the integration becomes:

$$\begin{aligned} \mathrm{Cov}(\ell, \ell') = & \delta_{\ell\ell'} \, \frac{1}{(A\bar{n})^2 \, A_\ell^2} \int \mathrm{d}^2\ell \Big[(2\pi)^4 \, \bar{n}^2 \, \delta(0) \, P_{\gamma\gamma} + (2\pi)^4 \, \bar{n} \, \delta(0) \, \sigma_\epsilon^2 \Big] (P_{yy} + P_{n_y n_y}) \\ & + \delta_{\ell\ell'} \, \frac{1}{(A\bar{n})^2 \, A_\ell^2} \int \mathrm{d}^2\ell \left((2\pi)^2 \, \delta(0) \, \bar{n} (P_{\gamma y} + P_{\gamma n_y}) \right)^2 \\ = & \delta_{\ell\ell'} \frac{(2\pi)^2}{A {A_\ell}^2} \int \mathrm{d}^2\ell \left(P_{\gamma\gamma} + \frac{\sigma_\epsilon^2}{\bar{n}} \right) \left(P_{yy} + P_{n_y n_y} \right) \\ & + \; \delta_{\ell\ell'} \frac{(2\pi)^2}{A {A_\ell}^2} \int \mathrm{d}^2\ell \left(P_{\gamma y} + P_{\gamma n_y} \right)^2 \; . \end{aligned} \tag{4.30}$$

Introducing the band power, the covariance of the cross-correlation power spectrum is finally completely described by:

$$\mathrm{Cov}(\ell, \ell') = \; \delta_{\ell\ell'} \frac{(2\pi)^2}{A A_\ell} \left[\left(\bar{P}_{\gamma\gamma} + \frac{\sigma_\epsilon^2}{\bar{n}} \right) \left(\bar{P}_{yy} + \bar{P}_{n_y n_y} \right) + \left(\bar{P}_{\gamma y} + \bar{P}_{\gamma n_y} \right)^2 \right] . \tag{4.31}$$

The barred values correspond to band power spectra and $A_\ell = 2\pi\ell\Delta\ell$.

Finally, taking the covariance to real space using the definition of the correlation function of the cross-correlation power spectrum:

$$\xi(\theta) = \int_0^\infty \frac{\ell \mathrm{d}\ell}{2\pi} \, P_{\gamma y}(\ell) \; J_1(\ell\theta) \tag{4.32}$$

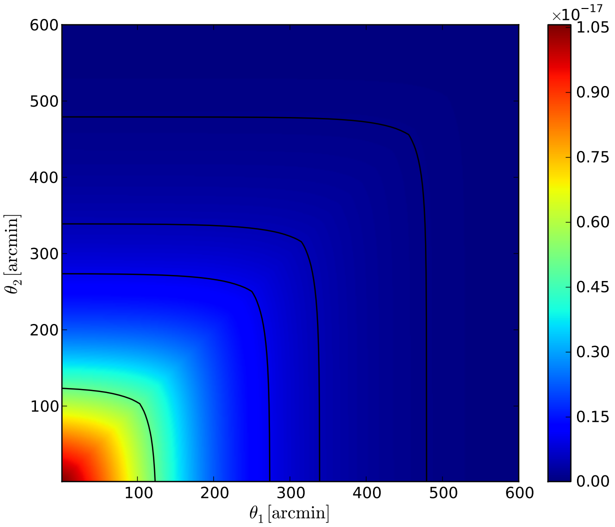

Figure 4.6: Covariance matrix of the cross-correlation power spectrum between weak lensing and the SZ effect. Contours are linearly spaced and range from a minimum value of 10^{-18} up to 10^{-15}.

we get that the transformation of the covariance into real space becomes:

$$\begin{aligned}\left\langle \Delta\xi(\theta)\,\Delta\xi(\theta')\right\rangle &= \int \frac{\ell \mathrm{d}\ell}{2\pi} \int \frac{\ell' \mathrm{d}\ell'}{2\pi}\ \mathrm{Cov}\ J_1(\ell\theta)\,J_1(\ell'\theta') \\ &= \int \frac{\ell \mathrm{d}\ell}{2\pi A}\left[\left(\bar{P}_{\gamma\gamma} + \frac{\sigma_\epsilon^2}{\bar{n}}\right)\left(\bar{P}_{yy} + \bar{P}_{n_y n_y}\right) + \left(\bar{P}_{\gamma y} + \bar{P}_{\gamma n_y}\right)^2\right]\cdot \\ &\qquad J_1(\ell\theta)\,J_1(\ell\theta') \end{aligned} \tag{4.33}$$

Given the dependence of the above quantity on the measurement specifications, we consider the following parameters: a survey covering a field area $A = 1000$ square degrees, a galaxy background density $\bar{n} = 30$ arcmin^{-1} and an ellipticity dispersion of $\sigma_\epsilon = 0.3$. The choice of area range was inspired by the possibility of overlap of ranges reached by present and future weak lensing and SZ effect surveys such as the ongoing South Pole Telescope measures (Williamson et al. 2011), the *Planck* mission (Planck Collaboration et al. 2011a) or the upcoming *Euclid* space telescope (Laureijs et al. 2011).

In Figure 4.6 we present our estimate of the covariance matrix of the lensing-SZ cross-correlation power spectrum. It shows a very broad distribution of uncertainties as proven by the lack of an obvious diagonal feature, unlike what happens in the shear-only power covariance matrix. This is due to the fact that the shot-noise term embodied by $\sigma_\epsilon^2/\bar{n}$ dominates the source of error in the shear calculation. In our case, the shear power spectrum is coupled with the SZ effect spectrum and is subsequently added to the cross-term, diminishing the influence of shot-noise in the covariance matrix values.

4.3.4 Correlated errors

The correlated errors are obtained directly from the covariance matrix and are useful to evaluate the error bars associated with each angular bin in the calculation of the correlation function. These will be

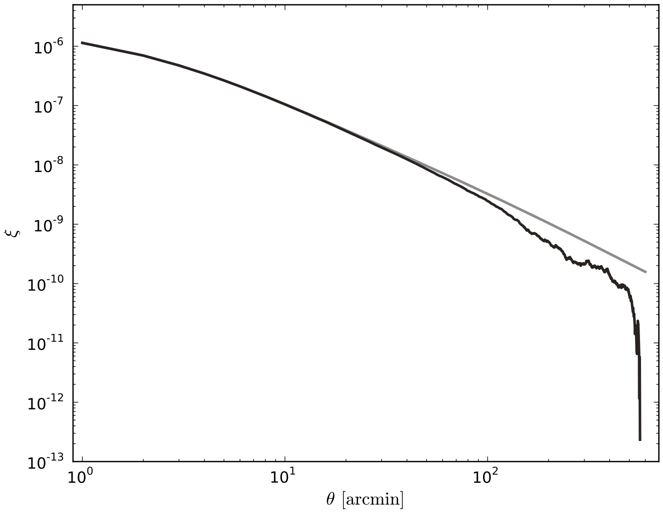

Figure 4.7: Perturbed correlation function of the fiducial model.

of particular use in the next chapter, when we focus on how the cross-correlation signal depends on the redshift. Moreover, in order to do likelihood analysis with our data, we need to perturb the model we are testing and for that task we also use the correlated errors.

The covariance matrix of a given correlation function contains the dispersion of the values of said function. To compute the correlated errors, we calculate the eigenvalues of the covariance matrix and perturb them with a Gaussian distribution of randomly generated numbers centred in zero, meaning that the average of the error distribution should vanish, and rotate the errors back to the original frame.

Figure 4.7 shows how our fiducial model can be perturbed by a set of correlated errors which were computed in this way.

Chapter 5

Redshift dependence of the cross-correlation signal

FOLLOWING THE COMPUTATION of the cross-correlation power spectrum, we investigated the dependence of the signal with redshift. By gaining insight on how dark and hot baryonic matter correlate in redshift one can better understand the evolution of structures through the observable signal of the cross-correlation. Through the redshift dependence of the signal, we aim to trace the thermal evolution of gas and thus, structure growth.

In Section 5.1, we start by looking into the degree of dependence on redshift presented by the auto-correlation signal, both for a dark matter and a gas distribution. Afterwards we inspect the cross-correlation 3-dimensional signal for different redshift values. We then integrate the auto- and cross- power spectra in redshift bins, in Section 5.2, to compare the contribution to the signal from different distance intervals. Finally, we evaluate the correlation function of the cross-correlation power spectrum in redshift bins and compute the correspondent correlated errors.

5.1 Redshift dependence of the 3-dimensional spectra

To create the power spectrum data, we compute the values of halo terms 1 and 2 for a range of redshifts and store them in an information object with dimensions of $[spectra \times wavenumber\ range \times redshift\ range]$.

Figure 5.1 shows the total 3-dimensional power spectrum (top panel) as well as the 1- and 2- halo contributions (middle and bottom panels, respectively) of the dark matter (on the left) and the gas distributions (on the right). The dark-matter density signal will overall decrease with increasing redshift. The shapes of the total and halo terms remain fundamentally unchanged by the variation of z.

However, the power of the baryonic distribution behaves somewhat more eccentrically with the increase of redshift: the halo-halo correlation is negligibly affected up to wavenumbers of about $k \sim 1$ after which the signal increases with redshift; the contribution of individual halos presents an inversion of this trend as for wavenumbers below a few $\mathrm{Mpc}^{-1}\,h$ the signal is weaker for higher redshifts. At the small scales limit, as redshift increases, the 1-halo term (and consequently, the total power) tends to become constant. As a result of the combination of both halo terms, the shape of the overall power varies to some degree. This is due to the peculiar behaviour of the angular-diameter distance as it increases until redshift 1.25, reaching a broad peak and then decreasing towards higher redshifts (see Section 1.2.2.)

Figure 5.2 shows the variation with redshift of the total and halo terms cross-correlation signal between the dark matter and gas distributions. Here, the 1-halo term increases its contribution at larger redshifts while the less influent two-halo term presents the opposite trend. The total signal is however clearly dominated by the power from individual halos and therefore the two share the spectrum shape with the exception of some minor deviations caused by the halo-halo correlation at very large scales. It seems like the cross-correlation spectrum will borrow more characteristics from the baryon distribution signal while, at the same time, presenting smoother curves. Since the gas has finite pressure, it develops a core which smoothens it the dark matter cusp.

5.2 Redshift-binned signal and correlated errors

We further computed the angular power spectrum in sequential redshift bins to evaluate the contribution to the signal from sources within different redshift intervals. The results are presented in Figure 5.3. In all cases, the large scale regime is dominated by sources which are closer to the observer, a trend that is more intense in the SZ spectrum with the closest bin being the largest contribution up to $\ell \sim 200$. This is a natural projection effect as closer sources appear larger in the sky. For the convergence power spectrum, past the large scales regime, the signal arises mostly from the intermediate redshifts, an effect intrinsic to the geometrical sensitivity of gravitational lensing itself. The intermediate bin is prevalent in the SZ power for a brief range of intermediate scales and the farthest bin dominates the source of power in the small scale limit. This too is a particular feature of the SZ effect, as it arises mostly from the smaller and much more abundant clusters. The behaviour of the cross-correlation power spectrum curves is very close to that of the SZ effect, indicating that the dependence on scales, source characteristics and redshift ranges is more closely related to the gas distribution than the dark matter abundance and sensitive to the imposed mass cut-off.

We computed the correlation function via Eq (4.5) and investigated the influence of the redshift on the observed signal signal. Figure 5.4 shows the correlation function of the measures in the different redshift ranges within the interval of redshift 0 to 1. The correspondent correlated errors per angular bin, calculated from the covariance matrix data as explained in 4.3.4, are also plotted. To compute the errors, we used the same survey parameters and assumptions as presented in Sections 4.3.3. For very small angles, there is a slight predominance of the signal originated from sources at the intermediate redshift range for very small angles, while above approximately 4 arcminutes the closest sources give the highest contribution to the correlation. The correlation signal steadily decreases with the increase of angle.

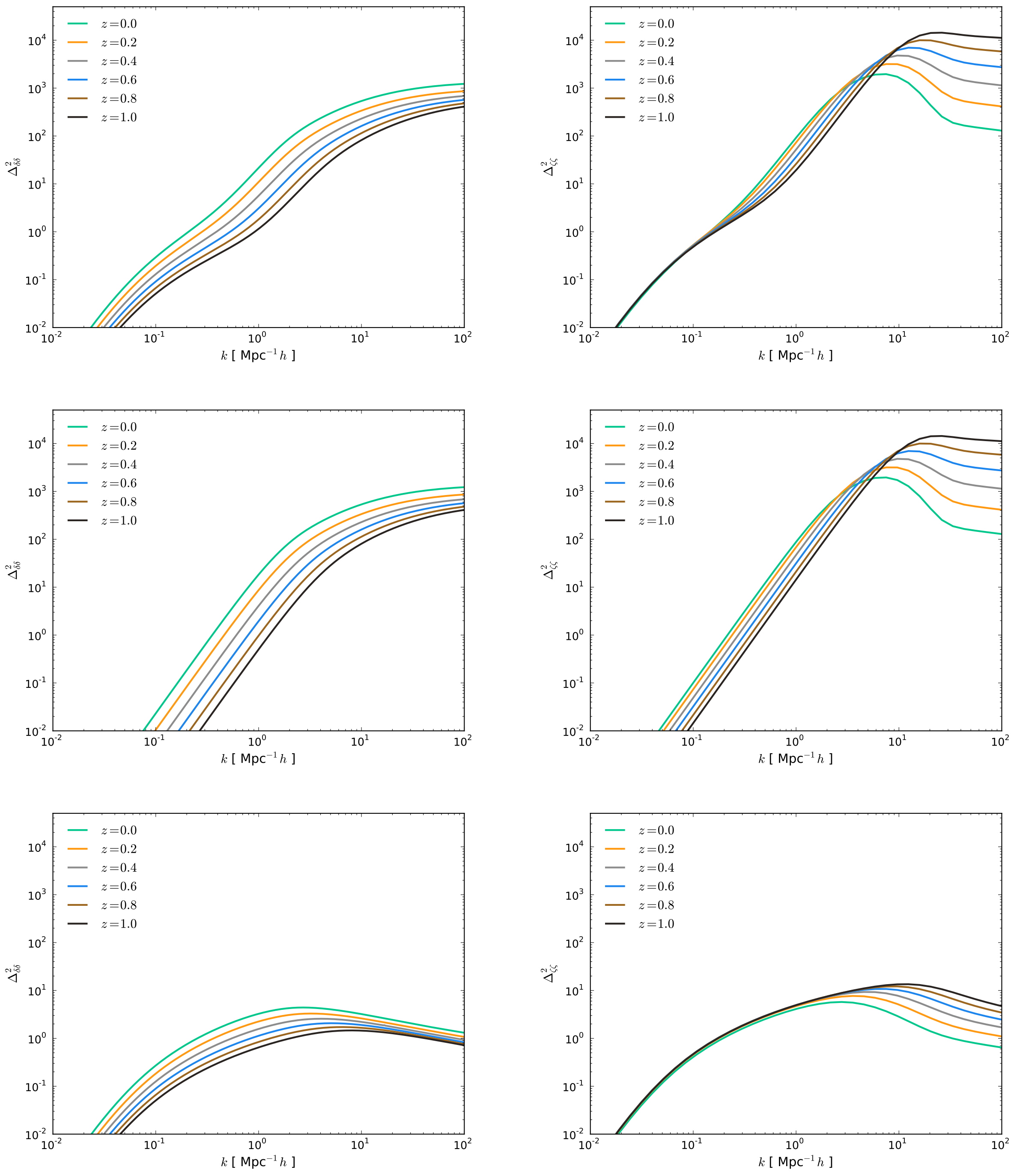

Figure 5.1: Variation of the 3-dimensional dark-matter density (left panel) and gas pressure (right panel) auto-correlation power spectra with redshift. Top plots show the total power spectra for different redshift values; middle and bottom plots show the variation of 1- and 2-halo term contributions, respectively.

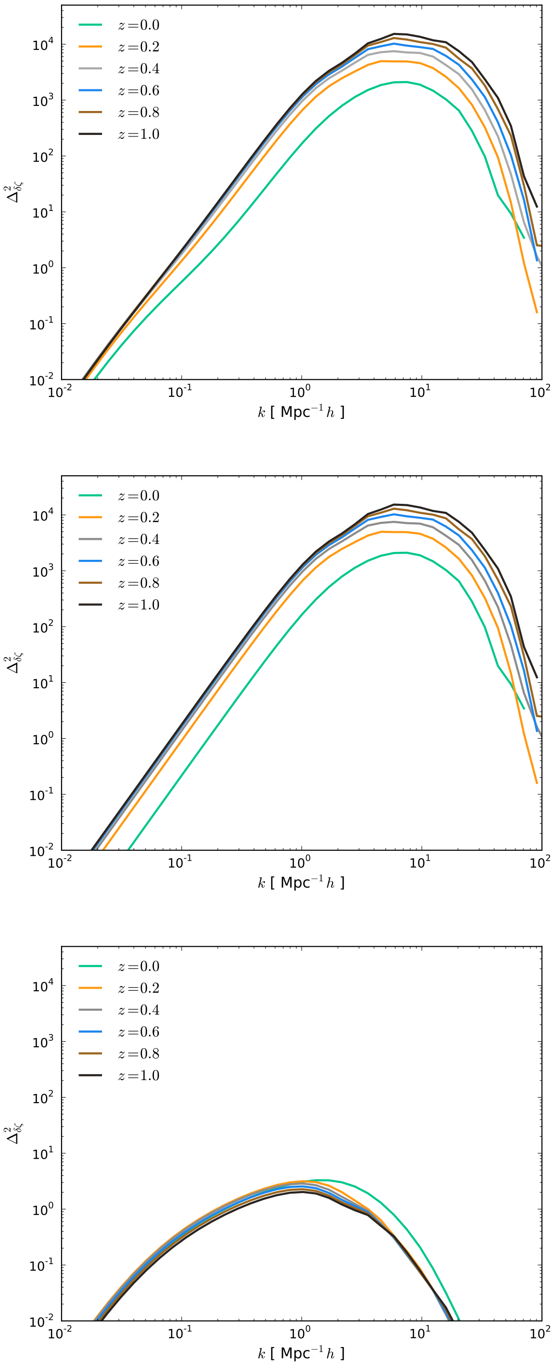

Figure 5.2: Variation of the 3-dimensional cross-correlation power spectrum with redshift. Top panel shows the total signal and middle and bottom panels correspond to the 1- and 2- halo terms, respectively.

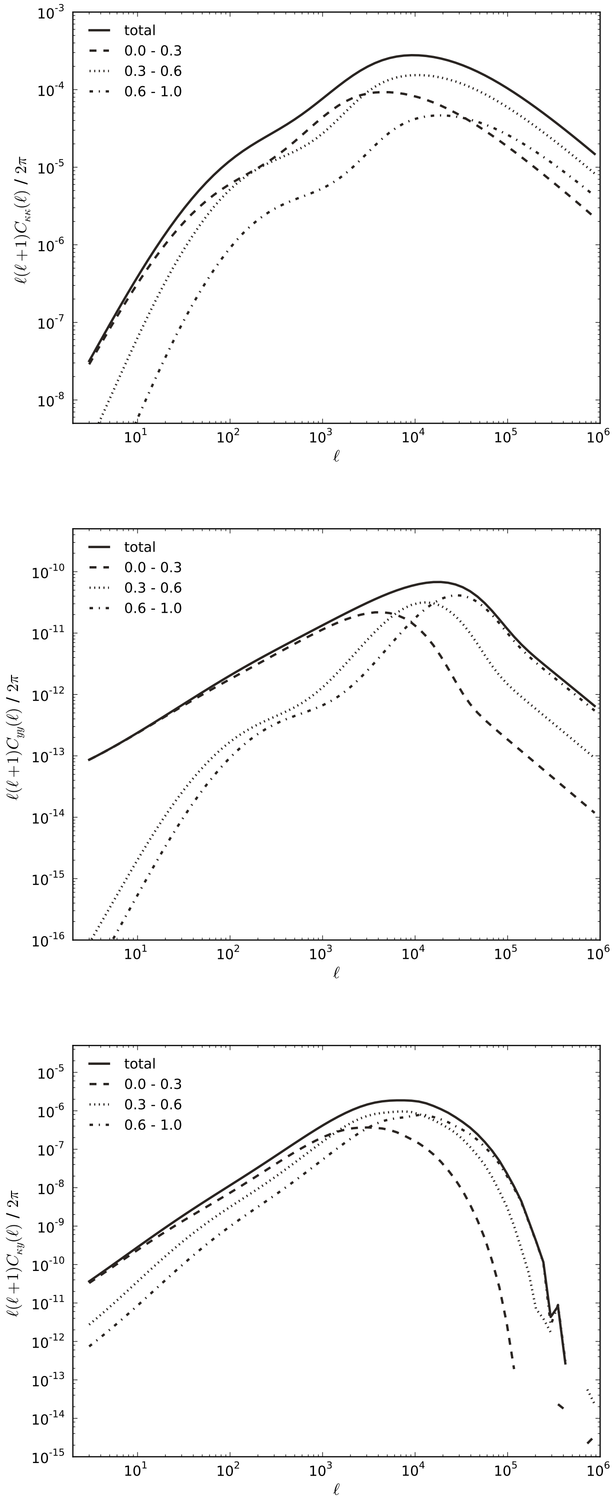

Figure 5.3: Redshift binned angular power spectrum. The top plot depicts the convergence power spectrum, the middle plot corresponds to the Sunyaev-Zel'dovich power spectrum and the bottom plot depicts the cross-correlation. All curves are the sum of both halo terms. Redshift ranges from 0 to a maximum of 1 and the bins are limited as shown in the legends.

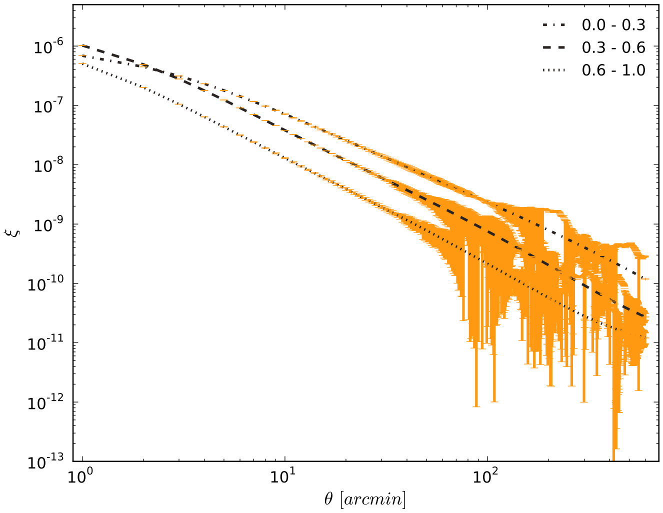

Figure 5.4: Redshift binned correlation function of the cross-correlation power spectrum with correlated errors. We assume a survey area of 1000 square degrees, a galaxy background density of 30 $\bar{n}$ = 30 arcmin^{-1} and an ellipticity dispersion of $\sigma_\epsilon = 0.3$.

Chapter 6

Constraints on cosmological parameters

THIS CHAPTER IS DEVOTED TO assessing if the statistical analysis of the cross-correlation power spectrum between the cosmic shear and the baryonic distribution thermal imprint in the CMB radiation may be able to constrain the parameters of the cosmological model. First, we take a look at how the cross-spectrum is affected by the change of these two parameters, by simply varying one of them at a time, for which the results and plots are presented in Section 6.1. The correlation function and corresponding covariance matrix computed in the previous sections allow an attempt to investigate constraints on the parameter plane we naturally focus on given our raw signals: $\Omega_{\rm m}$– σ_8. The analysis of the χ^2 (or likelihood) distribution and the Fisher-Matrix from the likelihood distribution are calculated in Section 6.2.

6.1 How the parameters affect the spectra

As a first step towards understanding how different cosmological parameters affects the cross-correlation signal, we vary the matter density parameter $\Omega_{\rm m}$ while the fluctuation amplitude σ_8 is kept fixed and vice-versa. Figure 6.1 shows the 3-dimensional (top panel) and angular (bottom panel) power spectra of the fiducial model – with $\Omega_{\rm m} = 0.272$ and $\sigma_8 = 0.809$ – and the spectra computed with the extreme values of the cosmological parameters:

$$\begin{aligned}(\,\Omega_{\rm m}^{min}, \Omega_{\rm m}^{max}) =& (\,\Omega_{\rm m}^{fid}(1-50\%)\,,\,\Omega_{\rm m}^{fid}(1+50\%))\\ (\,\sigma_8^{min}, \sigma_8^{max}) =& (\,\sigma_8^{fid}(1-20\%)\,,\,\sigma_8^{fid}(1+20\%))\end{aligned}$$

All spectra is presented as a ratio with the fiducial model signal. Most curves show minor deviations from the fiducial model when the cosmological parameters are varied. The deviations from the fiducial model are more evident with the variation of σ_8, were an increased value of the fluctuation amplitude translates into an increase in signal while the converse is also true. In the matter density case, we observe an increase of power with smaller values of $\Omega_{\rm m}$ in the small-scale regime. The opposite behaviour is found on the curves for the variation of the spectra with σ_8, with more obvious deviations from the fiducial values, for most of the angular range. With the projection from the three-dimensional to the angular power spectrum, the tendency found in the 3D spectra for the $\Omega_{\rm m}$ variation changes, as the weight function depends on the matter density explicitly and proportionally.

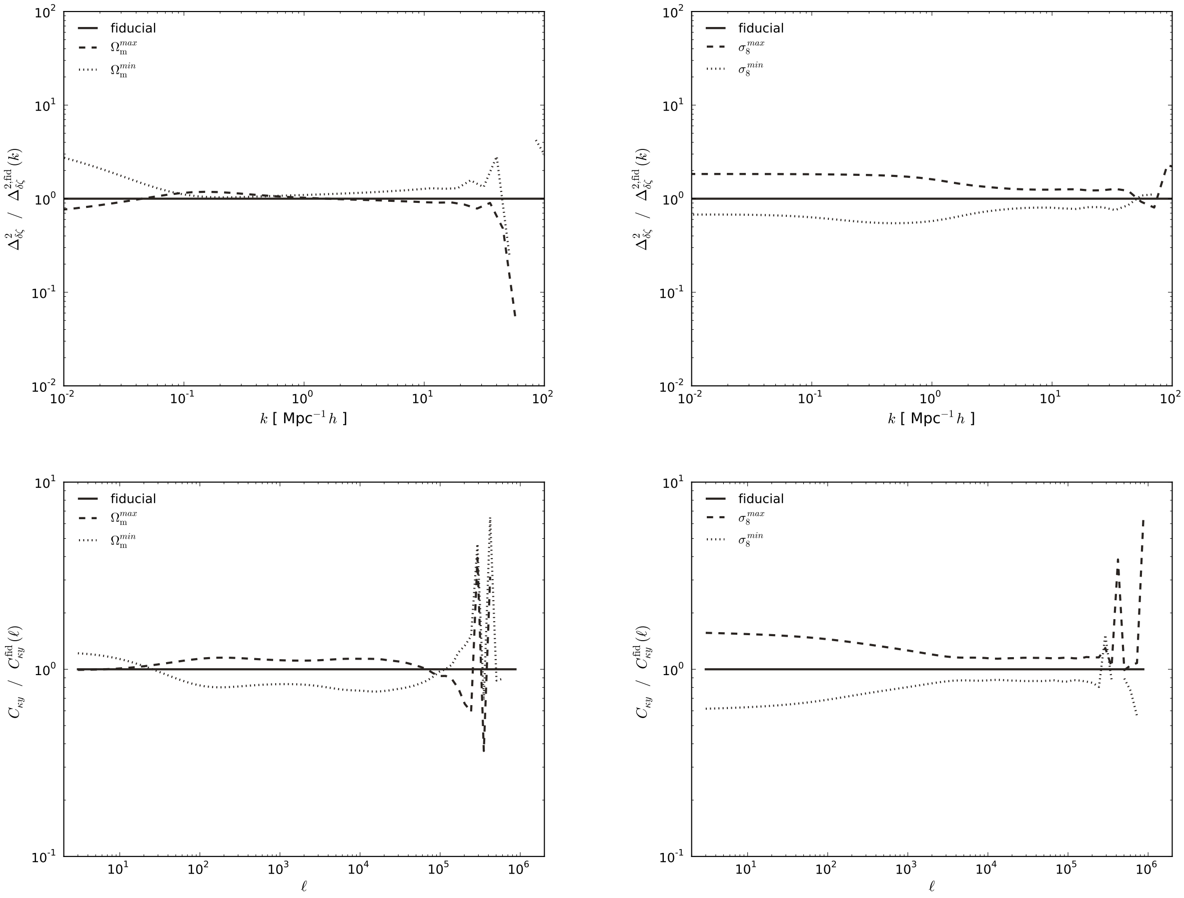

Figure 6.1: Dependence of the 3-dimensional (top panel) and angular (bottom panel) cross-correlation power spectra on cosmological parameters. All plots show the ratio between the spectra with alternative parameters and that of the fiducial model. On the left, $\Omega_{\rm m}$ is varied while σ_8 remains fixed to the fiducial value and one the right σ_8 changes, maintaining the fiducial value for $\Omega_{\rm m}$.

The angular power spectrum for different σ_8 values shows minor shifts in amplitude from the fiducial model, maintaining the tendency of the 3D power spectrum for the same amplitude fluctuation levels. Overall, these results reflect what is already known from the literature: the spectra of both signals (weak lensing and SZ effect) increase with higher values of these cosmological parameters. A high matter density naturally and a higher clustering level means more mass and more structures to contribute to the final signal.

6.2 Likelihood and Fisher analysis

We consider that our data is given by two-dimensional cross-correlation functions whose underlying model is specified by the cosmological parameters (and the background galaxy distribution.) We estimate the χ^2 distribution, as defined in Schneider et al. (2002), which depends directly on the correlation function (4.5) and on the inverse of the covariance matrix (4.33) from the cross-correlation power spectrum:

$$\chi^2(p) = \sum_{ij} \left(\xi_i(p) - \xi_i^{\text{fid}} \right) \text{Cov}_{ij}^{-1} \left(\xi_j(p) - \xi_j^{\text{fid}} \right) \tag{6.1}$$

p illustrates the set of parameters we vary, ξ^{fid} is the correlation function of our fiducial model perturbed by correlated errors, mimicking the data, as shown in Section 4.3.4 and the indices label the correlation function angular bins.

In the computation of the likelihood, we vary the values of matter density Ω_{m} and fluctuation amplitude σ_8 while keeping all other cosmological parameters fixed. Nonetheless, we further assume a spatially-flat Universe, meaning that our models obey $\Omega_{\text{m}} + \Omega_\Lambda = 1$.

Following the formalism presented in Fisher (1935) and adapted to our calculation, we can compute the Fisher matrix of the χ^2 distribution by estimating the expectation value of its second-order derivative with the cosmological parameters, at the minimum value of χ^2:

$$F_{ij} = \frac{1}{2} \frac{\partial^2 \chi^2}{\partial p_i \, \partial p_j} \tag{6.2}$$

meaning that the Fisher matrix is the expectation value of the lowest-order non-vanishing term in the Taylor expansion of the χ^2 distribution in the model parameters:

$$\chi^2 = \chi_{\text{min}} + \left(F_{ij} \delta p_i \, \delta p_j \right) |_{\chi_{\text{min}}} \tag{6.3}$$

Our results are jointly shown in Figure 6.2, where (6.1) and (6.3) are depicted against one another. Unlike what happens in the case of weak lensing, the signal doesn't have a very defined dependence on the Ω–σ_8 plane. The contours of the χ^2 distribution hint for a high level of non-Gaussian-like features. To better understand the shape of the χ^2 function, we show the contour plot evaluated at more levels than the previous one. In Figure 6.3 we confirm that the distribution is indeed somewhat tilted. This behaviour explains why the expansion of the χ^2 up to its second derivative does not yield small Fisher-matrix contours, as the curvature is not straightforward.

Moreover, we conclude that this cross-correlation is not suitable to estimate or constrain the cosmological parameter space. The Sunyaev-Zel'dovich power spectrum is typically very sensitive to the value of σ_8. This effect is however damped by the lack of angular resolution in the weak gravitational lensing signal.

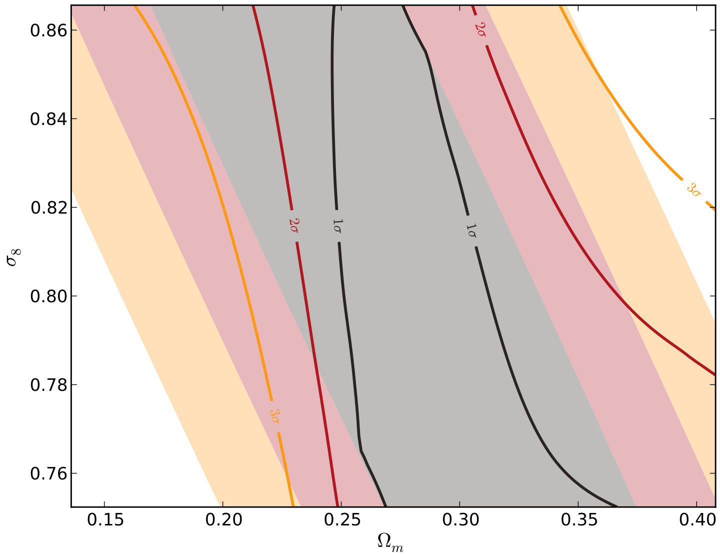

Figure 6.2: Fisher matrix ellipses plotted against χ^2 contours. The confidence levels of the χ^2 contours colour-match those of the filled ellipses. those of the

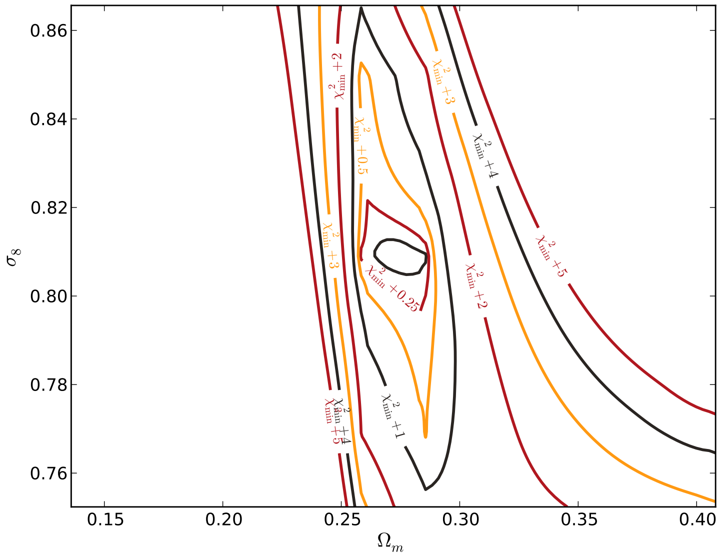

Figure 6.3: A more refined depiction of the χ^2 distribution contours showing the eccentric behaviour of the function.

We conclude that the lack of cosmological sensitivity rather opens ways to study parameters characterising the evolution of the cluster population.

Chapter 7

Heating history of baryons

In this chapter, we an effort to further use the potential of this cross-correlation to give us information on the structure evolution; particularly on how the gas temperature in cluster-sized halos evolved over time, and the behaviour of gas. We further modelled our description of the temperatures in gas halos by introducing a term that sorts hot halos. In Section 7.1 we present this heating term and investigate the effect it has on the 3-dimensional and angular power spectra. We additionally bin the signal into two redshift bins to infer how the signal is distributed along the line-of-sight integration.

7.1 Additional modelling of the cluster temperature

The halo mass-redshift space contributing to the cross-correlation signal is further constrained by considering collapsed structures only. For that purpose, an additional term is introduced to the temperature power law, taking into account whether a halo of a given mass has already reached its virial temperature after formation at a given redshift.

We assume that the heating of the gas is not instantaneous, but rather takes a certain multiple or fraction of the free-fall time:

$$\tau_{\mathrm{ff}} = \sqrt{\frac{1}{G\rho}} \tag{7.1}$$

with G being the gravitational constant. ρ can be taken as the scale density introduced as the density within the scale radius, as previously defined in Subsection 2.2.2. Here, we reproduce and re-arrange Eq. (2.18), which provides an expression for the scale density:

$$\begin{aligned} m_{200} &= \int_0^{r_{200}} \mathrm{d}r\ 4\pi r^2\ \rho_{\mathrm{s}} \\ &= 4\pi\,\rho_{\mathrm{s}}\,r_{\mathrm{s}}^3\,\left[\ln(1+c)\ -\ \frac{c}{1+c}\right] \\ &\equiv 4\pi\,\rho_{\mathrm{s}}\,r_{\mathrm{s}}^3\,\log C(c) \end{aligned} \tag{7.2}$$

At the same time,

$$\begin{aligned} m_{200} &= 200\, \frac{4\pi}{3}\, r_{200}^3\, \rho_{\mathrm{cr}} \qquad (7.3) \\ &= \frac{4\pi}{3}\, 200\, c^3\, r_{\mathrm{s}}^3\, \frac{3H^2}{8\pi G}. \qquad (7.4) \end{aligned}$$

Combining both of the above results, we can describe the scale density as:

$$\begin{aligned} \rho_{\mathrm{s}} &= \frac{200}{3}\, \frac{c^3}{\log C(c)}\, \frac{3H^2}{8\pi G} \qquad (7.5) \\ &\equiv \delta_{\mathrm{s}}\, \frac{3H^2}{8\pi G}. \end{aligned}$$

It is now possible to the free-fall time in the following way:

$$\begin{aligned} \tau_{\mathrm{ff}} &= \sqrt{\frac{1}{G\,\rho_{\mathrm{s}}}} = \sqrt{\frac{1}{\frac{3H^2}{8\pi G}\,\delta_{\mathrm{s}}}} \qquad (7.6) \\ &= \sqrt{\frac{8\pi}{3}}\, \frac{H_0}{H}\, \frac{1}{H_0}\, \frac{1}{\sqrt{\delta_{\mathrm{s}}}} \end{aligned}$$

and by introducing $\tau_{\mathrm{Hubble}} = 1/H_0$, we can express the free-fall time in units of the present Hubble time:

$$\frac{\tau_{\mathrm{ff}}}{\tau_{\mathrm{Hubble}}} = \sqrt{\frac{8\pi}{3\delta_{\mathrm{s}}}}\, \frac{H_0}{H}. \qquad (7.7)$$

We plug this description of the free-fall time in Eqs. (4.1) and (4.2) by multiplying the temperature-mass function by a heating factor:

$$t_{\mathrm{heat}}(m, z, f) = \exp\left(-f\, \frac{\Delta_t}{\tau_{\mathrm{ff}}}\right) \qquad (7.8)$$

where Δ_t is the difference between the halo redshift and its collapse redshift. The formation redshift is estimated by following the prescription by Navarro et al. (1997). This term introduces a new variable, a ratio f between the heating and free-fall time-scales, into the estimation of the signal, one that allows us to get insight on the dependence of the signal on the heating history of the baryonic matter present in dark matter halos.

Figure 7.1 shows the variation of the heating factor with mass and redshift, for different values of the factor f as labelled. t_{heat} will weight the temperature increasingly with the halo mass, as well as with redshift. For the fiducial model computed in this work, f is zero. Deviations from the fiducial value mean an increasingly sharp cut in the less massive structures.

In Figure 7.2, we plot the total 3-dimensional cross-correlation power spectra for different values of parameter f at fixed redshift zero. We find that the signal decreases very significantly with increasing f values, meaning that constraining the integration to collapsed halos only will seriously affect the power spectrum. The same behaviour is found on the curves of the angular power spectra (see Figure 7.3.) A small but noticeable decrease of contribution by the 2-halo term to the total power on the large-scale regime is also observed.

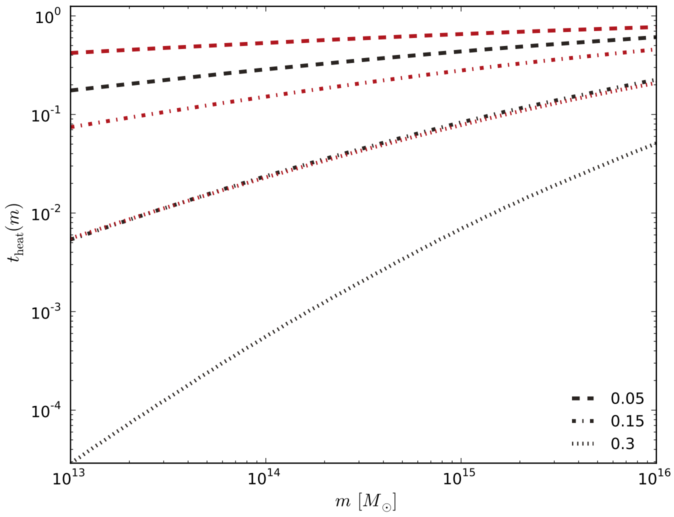

Figure 7.1: Heating factor variation with mass, redshift and factor f. Black lines correspond to redshift 0 and red lines to redshift 1. The legend indicates the value of the parameter f.

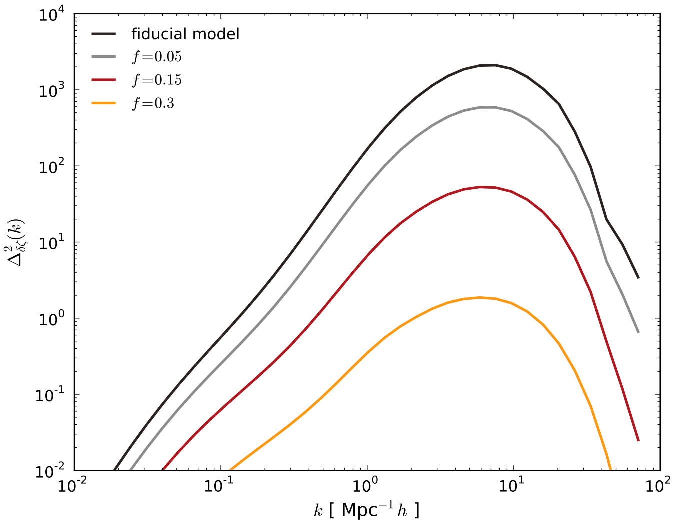

Figure 7.2: Variation of the total 3-dimensional cross-correlation power spectrum with f values. Power spectrum taken at redshift 0.

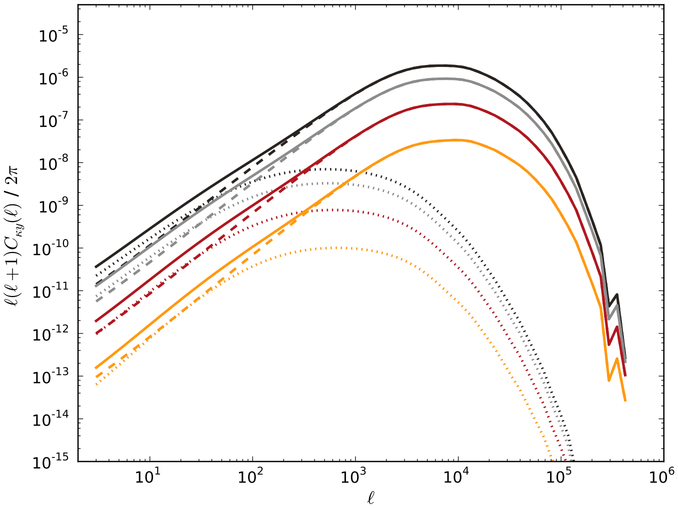

Figure 7.3: Variation of the cross-correlation angular power spectrum with f values. Solid lines portray the total signal, dashed and dotted lines show the 1- and 2-halo terms. Black lines depict the fiducial model with $f = 0$. Grey, red and yellow lines show the angular spectra for f of increasing values: 0.05, 0.15 and 0.3, respectively.

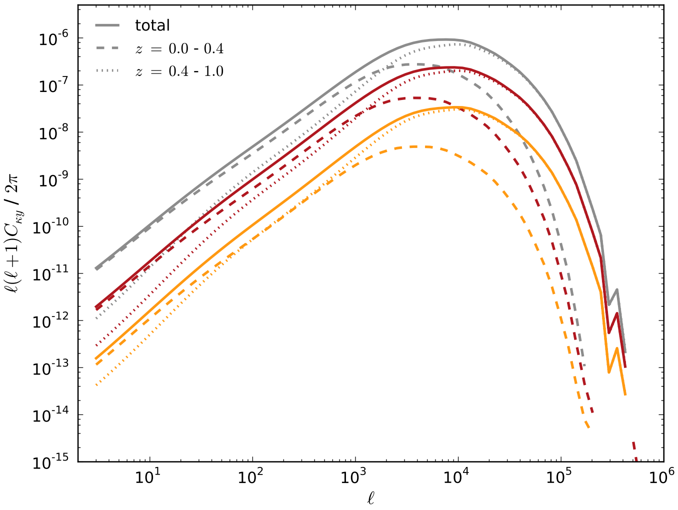

Figure 7.4: Cross-correlation signal within two redshift bins as labelled. Total lines are depicted as solid curves. Greylines correspond to f = 0.05, red lines have f = 0.15 and yellow lines are the spectrum with f = 0.3.

We further analysed the dependence of the signal in redshift by integrating the 3-dimensional power spectrum in two different redshift bins from redshift 0 to 1. We plot our findings in Figure 7.4. For every f value, most of the signal is collected in the farthest redshift bin, with the closest bin contributing more in the large-scale range. The latter contribution becomes less intense as the value of f increases.

After inspecting the above results, we conclude that the overall signal is highly sensitive to slight variations of the factor f. This behaviour points to the fact that to undergo tests on the constraining power of this model in the cosmological parameter space, one would need to only very slightly vary the value of f around the fiducial model value and carefully sample the area around it.

Conclusions and further work

To wrap up this thesis, we review the main steps of our work as well as the most important interpretations of our results. We further speculate on the investigations which naturally follow the method presented in this thesis.

Our present picture of the Universe can be characterised by the spatial distribution of halos, spread in filamentary structures that cross each other in nodes composed of halo clusters. Outside of this configuration there are only large volumes of mostly empty space. This image is supported both by observations of galaxies and galaxy clusters as well as by cosmological numerical simulations which begin with the Gaussian initial conditions of an early state in structure evolution, allowing a system of particles to evolve, while governed by the laws of gravitation.

We set out to carry this study motivated by the still largely undefined characteristics of the behaviour of structures throughout their formation and evolution periods. In order to investigate the nature of the changes that occur during halo growth and collapse, a large number of observational, theoretical and numerical techniques have been extensively used to model the evolution of structures. One of these methods is the so-called halo model which provides an analytic framework to compute the two-point correlation function of a given density field. This formalism, reviewed in Chapter 2, was based on an early attempt to statistically illustrate the galaxy distribution, and originally developed to describe the distribution of dark matter. In the model, the correlation function is the result of adding a Poisson term, accounting for the contribution to the signal by individual halos, and a halo-halo term, representing the correlations between halos. These terms are the product of a mass integration over the models describing the distribution, structure and biasing of halos.

The analytic estimation of the correlation function makes the halo model an additional source of insight to understand conclusions from numerical and observational data: the correlation function can be directly compared to results from simulations, while it can also be projected into an angular signal which is directly analysed against observations.

The halo model parameterises the computation of the two-point correlation function such that it is rather straightforward to adapt the framework in order to describe a cross-correlation signal. In this thesis, we took advantage of the good description of dark matter halos by the halo model, and cross-correlate the dark matter signal with that arising from the halo gas component. The resulting two-point correlation function – or its Fourier conjugate, the 3-dimensional power spectrum – relates the signals from a dark matter density-contrast distribution with the gas pressure within each halo. Projecting this cross-correlated signal into the angular power spectrum, while choosing adequate geometrical weight functions, yields the cross-correlation power spectrum between two phenomena: the weak gravitational lensing (accounting for the dark component of halos) and the thermal Sunyaev-Zel'dovich effect (tracing the gas component.)

In Chapter 3, we introduced the two effects and computed the auto-correlation 3-dimensional power spectra of each of them making use of the halo model formalism. We stated the models we choose to parameterise the halo description with. In addition to the commonly assumed models that are extensively used in such studies, we constrain our mass integration to only account for halos which are observed through both weak lensing and the thermal SZ effect. We verified the resulting spectra to be in accordance with the findings of previous studies where the halo model was used with the same purpose. Additionally, we projected the power spectrum into its angular signal by applying Limber's Equation (see Appendix A). The general behaviour of the power spectra curves reveals that the term related to individual halos (1-halo term) is the most significant source of signal overall, with the halo-halo correlations (2-halo term) being important only in the regime of large scales. The differential dependence of the signal on large and small scales discloses how the choice of the bias and density models strongly influences the power, respectively.

We specialised the halo model formalism to cross-correlate the dark matter and gas distributions. The 3-dimensional and angular cross-correlation signals, were presented in Chapter 4. The behaviour of the resulting spectra shows a smoothed signal which borrows characteristics from both the dark matter and the gas spectra. Overall, the halo-halo correlations become less decisive to the total signal and the observational limit imposes a decrease on small scales as halos become too small to be resolved. Further statistical analysis was performed by using the angular power spectrum of the cross-correlation. We computed the correlation function by integrating the angular spectrum over a top-hat filter. This function was used in the derivation of the covariance matrix: the expression for the matrix in real space relates the correlation functions with the angular auto- and cross-correlation power spectra of weak gravitational lensing and the SZ effect. The covariance matrix was then computed for a hypothetical survey with realistic parameters, yielding a strikingly non-diagonal result. With the covariance matrix we computed correlated errors of the correlation function which would be of use later on in our study.

The next step in our analysis was to investigate the signal evolution by inspecting the dependence of the cross-correlation power spectrum on redshift. In Chapter 5, we first looked into the changes sustained by the 3-dimensional auto- and cross-correlation power spectra. As expected, the overall signal increases with redshift. The most remarkable features reside in the gas pressure spectra, which show a stark increase of signal towards a stable amount of signal (imprint of the angular-diameter distance) in the small-scale regime while maintaining the amplitudes in the very large scales. The cross-correlation signal exhibits a behaviour very close that of the gas distribution, although with smoother curves (presents smooth peaks); this is explained by the structural differences of the halo densities of gas and dark matter, as well as by the fact that weak lensing lacks the angular resolution for resolving the gas distribution. We additionally projected the 3-dimensional spectra integrating over different redshift bins. Again, we performed this analysis in the auto- and cross-correlation cases. Again to no surprise, we found that the signal from different redshift bins is bound to increased contributions from different scales. The large-scale regime is dominated by the closer sources of power, as they occupy wider angles in the sky by the projection effect. The peak of the cross-correlation power relies on sources within intermediate redshift scales and the contribution at small-scales by the farthest sources is an inherited feature from the SZ effect. To conclude the redshift analysis, we computed the correlation function obtained in Chapter 4 in the same redshift bins and calculated the correlated errors associated to them. The signal mostly arises from intermediate redshifts and invariably decreases with the increase of scales, as naturally does the amplitude of the errors.

We further use the cross-correlation power spectrum in an attempt to constrain the cosmological parameter space by doing likelihood and Fisher analyses in Chapter 6. The cosmological parameter space is not well constrained by the cross-correlation signal between dark matter and gas pressure. This is due to the limiting nature of the angular resolution in the weak lensing signal, which severely damps the strong dependence of the SZ effect signal on the fluctuation amplitude given by σ_8. Although the cross-correlation signal is not suitable to make assumptions on the underlying cosmological model, it hints at the possibility of characterising the intrinsic properties of the cluster population.

The closing chapter of this thesis was devoted to a further constraint of the mass-redshift plane: we introduced a term to include only hot structures. We delay the heating of the gas assuming that the heating time-scale is a multiple of the free-fall time-scale. We analysed the signal for different values of the parameter f, characterising the ratio between the heating and free-fall time-scales, and how that signal is distributed in redshift and we found out that relatively small variations of the parameter induce rather intense amplitude changes. Further work with this modelling method would include the tentative evaluation of the constraining power of f against cosmological parameters. For this, a field of extremely small deviations from the fiducial value $f = 0$ should be sampled.

The halo model is constructed in such a manner that it allows to test a wide range of signals arising from the different components of the cosmological paradigm. Choosing different models to describe these components is a way to gain insight into how they affect the signal and, most importantly, on how they perform against observations. Many possible cross-correlations can be investigated with the halo model, as shown in Cooray (2000); Cooray and Sheth (2002). A natural transition from this work could be to build the cross-correlation between the SZ effect and the X-ray emission from galaxy clusters. Both signals depend on the same halo components but do, however, depend on the gas pressure in different ways. This distinction can be useful to further evaluate the thermal history of baryons within collapsed structures.

Appendix A

Random fields and Limber's Equation

We describe the formalism that allows the simple projection of the power spectrum into its angular description, which we used extensively in this work. The original framework was devised by Limber (1954) after which the projection relations are named. Presented here is the derivation of the equation following Bartelmann and Schneider (2001).

■ **Properties of a random field** The definition of a random field $g(x)$ comes with several properties. First of all, the average of the field is zero: $\langle\, g(x)\,\rangle = 0$, $\forall x$. Secondly, the field is homogeneous, meaning that $g(x)$ and a translation given by $g(x+y)$ are not statistically distinguishable. The field is also isotropic, for $g(x)$ and $g(\mathcal{R}x)$ share the same statistical properties, with $\mathcal{R}$ standing for a rotation matrix of dimension n. The two-point correlation function of the field is given by:

$$\langle\, g(x)\, g^*(y)\,\rangle = C_{gg}(|\, x - y\,|) \tag{A.1}$$

where C_{gg} is a real number even if $g \in \mathbb{C}$. The Fourier pair of the field is given by:

$$g(x) = \int_{\mathbb{R}^n} \frac{\mathrm{d}^n k}{(2\pi)^n}\, \hat{g}(k)\, e^{\mathbf{i}\mathbf{x}.k} \quad \text{and} \quad \hat{g}(k) = \int_{\mathbb{R}^n} \mathrm{d}^n x\, g(x)\, e^{-\mathbf{i}\mathbf{x}.k} \tag{A.2}$$

so that the correlation function in Fourier space is given by:

$$\langle\, \hat{g}(k)\, \hat{g}^*(k')\,\rangle = \int_{\mathbb{R}^n} \mathrm{d}^n x\, e^{\mathbf{i}\mathbf{x}.k} \int_{\mathbb{R}^n} \mathrm{d}^n x'\, e^{-\mathbf{i}\mathbf{x}'.k'}\, \langle\, g(x)\, g^*(x')\,\rangle\,. \tag{A.3}$$

Using (A.1) and replacing $x' = x + y$, this relation becomes:

$$\langle\, \hat{g}(k)\, \hat{g}^*(k')\,\rangle = \int_{\mathbb{R}^n} \mathrm{d}^n x\, e^{\mathbf{i}\mathbf{x}.k} \int_{\mathbb{R}^n} \mathrm{d}^n y\, e^{-\mathrm{i}(\mathbf{x}+\mathbf{y}).k'}\, C_{gg}(|\, y\,|) \tag{A.4}$$

$$= (2\pi)^n\, \delta_{\mathrm{D}}(k - k') \int_{\mathbb{R}^n} \mathrm{d}^n y\, e^{-\mathbf{i}\mathbf{y}.k}\, C_{gg}(|\, y\,|) \tag{A.5}$$

with δ_{D} standing for Dirac's delta function. The power spectrum of an homogeneous and isotropic field g is then defined as:

$$P_g(|k|) = \int_{\mathbb{R}^n} \mathrm{d}^n y\, e^{-\mathbf{i}\mathbf{y}.k}\, C_{gg}(|\, y\,|) \tag{A.6}$$

thus yielding a direct relation between the two-point correlation function and the power spectrum:

$$\langle\, \hat{g}(k)\, \hat{g}^*(k')\,\rangle \equiv (2\pi)^n\, \delta_{\rm D}(k-k')\, P_g(|k|). \tag{A.7}$$

Limber's Equation The objective of this equation is to establish a relation between the two-point correlation function (or power spectrum) of a homogeneous, isotropic, 3-dimensional random field and its projection in 2D. We define a 3D field characterised by a density contrast dependent on a radial and angular co-ordinates r and θ as well as on a function of the r such that $\delta[f_k(r)\theta, r]$. θ is a 2-dimensional vector. We set the density contrast as having two different projections along the light-cone corresponding to an observer at $r = 0$ and $t = t_0$:

$$g_i(\theta) = \int {\rm d}r\, q_{\rm i}\, \delta[f_k(r)\theta, r] \tag{A.8}$$

with i = 1,2 and r ranging from zero to a given scale $r_{\rm H}$ standing for the horizon, the limit of the integration. Then the correlation function if given by:

$$C_{12}(\theta) = \langle\, g_1(\theta)\, g_2(\theta')\,\rangle \tag{A.9}$$

$$= \int {\rm d}r\, q_1(r) \int {\rm d}r' q_2(r')\ \langle \delta[f_k(r)\theta, r]\, \delta[f_k(r')\theta', r']\rangle \tag{A.10}$$

In the large-scale regime, where $k \to 0$, the density contrast power spectrum decreases proportionally with k, so we can assume that there is a coherence scale $L_{\rm coh}$ beyond which there are no fluctuations. For the correlation not to be zero, we need to take into account only the scales for which $|r - r'| \lesssim L_{\rm coh}$ stands, within the horizon distance. We assume that weight functions $q_{\rm i}$ do not vary substantially in over a scale $\Delta r \le L_{\rm coh}$. With such assumptions, and setting $f_k(r') \approx f_k(r)$ and $q_2(r') = q_2(r)$, the correlation function becomes:

$$C_{12}(\theta) = \int {\rm d}r\, q_1(r)\, q_2(r) \int {\rm d}(\Delta r)\ C_{gg}(\sqrt{f_k^2\theta^2 + (\Delta r)^2}, r) \tag{A.11}$$

This is Limber's Equation, relating the two-point correlation of the projected field to that of the 3-dimensional field. Another useful form of this equation is achieved when going into Fourier space: providing the relation between the two-point correlation and the projection of the 3-dimensional power spectrum. Replacing the density contrasts of Eq. (A.10) with (A.3), we get:

$$C_{12}(\theta) = \int {\rm d}r\, q_1(r) \int {\rm d}r'\, q_2(r') \int \frac{{\rm d}^3k}{(2\pi)^3} \int \frac{{\rm d}^3k'}{(2\pi)^3} \tag{A.12}$$

$$\langle\, \hat{\delta}(k,r)\, \hat{\delta}^*(k',r')\,\rangle \exp(-{\rm i}\, f_k(r)\, \mathbf{k}_\perp.\boldsymbol{\theta})\ \exp({\rm i}\, f_k(r')\, \mathbf{k}'_\perp.\boldsymbol{\theta})\ \exp(-{\rm i}\, k_3\, r)\ \exp({\rm i}\, k'_3\, r') \tag{A.13}$$

where $k_\perp$ is a 2-dimensional vector perpendicular to the line-of-sight. Using (A.4) we introduce P_δ into the above relation:

$$C_{12}(\theta) = \int {\rm d}r\, q_1(r)\, q_2(r) \int \frac{{\rm d}^3k}{(2\pi)^3}\ P_\delta(|k|, r)\ \exp(-{\rm i}\, f_k(r)\, \mathbf{k}_\perp.(\boldsymbol{\theta} - \boldsymbol{\theta}'))\ \exp(-{\rm i}\, k_3\, r) \int {\rm d}r'\ \exp({\rm i}\, k'_3\, r') \tag{A.14}$$

This result implies that only $2\pi\delta_{\mathrm{D}}(k_3)$ (solution of the last integral) will contribute to the projected correlation function; performing the integration over k_3, the correlation becomes:

$$C_{12}(\theta) = \int \mathrm{d}r\, q_1(r)\, q_2(r) \int \frac{\mathrm{d}^2 k_\perp}{(2\pi)^2}\, P_\delta(|k_\perp|, r)\, \exp(-\mathrm{i}\, f_k\, \mathbf{k}_\perp.\boldsymbol{\theta}) \tag{A.15}$$

$$= \int \mathrm{d}r\, q_1(r)\, q_2(r) \int \frac{\mathrm{d}k}{(2\pi)}\, J_0[\, f_k(r)\theta k\,]\,. \tag{A.16}$$

Following both the definition of power spectrum (A.6) and (A.2), we can finally relate projected power $P_{12}(\ell)$ as:

$$P_{12}(\ell) = \int \mathrm{d}^2\theta\, C_{12}(\theta) e^{\mathrm{i}\boldsymbol{\ell}.\boldsymbol{\theta}} = \int \mathrm{d}r\, q_1(r)\, q_2(r) \int \frac{\mathrm{d}^2 k_\perp}{(2\pi)^2}\, P_\delta(k_\perp, r)\, (2\pi)^2\, \delta_{\mathrm{D}}(\boldsymbol{\ell} - f_k(r)\mathbf{k}_\perp) \tag{A.17}$$

yielding the Fourier space version of Limber's Equation, used in this thesis:

$$P_{12}(\ell) = \int \mathrm{d}r\, \frac{q_1(r)\, q_2(r)}{f_k(r)^2}\, P_\delta(\ell / f_k(r), r)\,. \tag{A.18}$$

List of Figures

List of Tables

Acknowledgments

The closing stretch of any thesis is a compendium of lists and, for me, none is more relevant than this one.

I acknowledge the financial support of the **International Max Planck Research School for Astronomy and Cosmic Physics at the University of Heidelberg** and the **Heidelberg Graduate School of Fundamental Physics**.

I thank **Prof. Luca Amendola** for kindly agreeing to be the second corrector of this thesis and **Profs. Eva Grebel** and **Hans-Christian Schultz-Coulon** for their availability to be part of my defence committee.

I deeply thank **Matthias Bartelmann** for the opportunity to attempt a career in Physics but mostly for the patience and support that made me feel so much more confident after each meeting. His kindness and savoir faire kept me going through the many occasions when all I could think about was giving up.

I thank all the colleagues at the Institut für Theoretische Astrophysik that in one way or another contributed to my work or general sanity. I especially wish to express my gratitude to **Björn Malte Schäfer** and **Matteo Maturi** for being available to help me with my everyday work problems and to **Carlo Giocoli** for prodiving me with his code and thus a good head start. As a source of distraction, silliness and friendship, I thank in particular the company of **Christian Angrick**, **Federica Capranico**, **Alexander Gelsin**, **Alessandra Grassi**, **Gero Jürgens** and **Eleonora Sarli**.

The people I am about to mention are dear friends who have stayed close to me, and to my heart, before and/or during the last 4 years. Since I do not know if I will ever again be able to thank them on paper for being in my life and making me a happier person, I will now take my chance. To **Elisabete da Cunha** I thank for the two balconies, the smell and taste of homely food and fun dinner parties. I thank **Mischa Gerstenlauer**, for the companionship and for reminding me of the reasons why bicycles are important and useful. I might get one, one day. I thank **Alexander Karim** for always being such a fun, understanding and devoted friend. I thank **Benoît Knecht**, my dear partner of relaxing drinks, cafe-studying and movie day-dreaming. **Julian Merten**, for the traditions he helped me start, be it the Bar Centrale beer, the Bundesliga Saturdays or the slaps in my face. And for being a sweet and constant friend, even from the distance of his new home, all the way across an entire ocean and continent. The sweet and caring nature of **Milica Mićić** made my days at work, and beyond, more pleasant and worthy. I thank **Adi Zitrin**, my wonderful office mate who provides me with fun evenings, uplifting company and extraordinary cities to visit.

A very special thank you to **Catarina Cruzeiro** and **Carolina Rodrigues** for always making me feel truly at home when I stay at theirs. To **Gonçalo Gregório** who, with his wonderful crew in Porto, always recharges my batteries with craziness and laughter. **Filipe Gomes**, my dear, dear friend, relentlessly and unconditionally there for me. And it is because of **Mafalda Dias** that, for the last ten years, I have been more of a dreamer and paradoxically a more pragmatic person. Together with **Sandra Castiço**, she always supplied me with inspiration, optimism and the (by now incurable) need for wonder.

Para com o meu pai **António**, a minha mãe **Alcina** e minha irmã **Lena**, tenho uma extraordinária dívida de gratidão pelo apoio, calor familiar constante e amor incondicionais.

Finally, in a last, warmest of thank you notes, I address *the* one person who made it possible for this thesis to ever be real. My heart is immersed in all he has given me throughout these years. I would need a whole other list to thank him properly. Dearest **Emanuel**, my lover and my love.

Ana Valente | Heidelberg | October 2012

References

M. Albrow, P. Birch, J. A. R. Caldwell, R. Martin, J. Menzies, J.-W. Pel, K. Pollard, P. D. Sackett, K. C. Sahu, P. Vreeswijk, A. Williams, and M. Zwaan. PLANET (Probing Lensing Anomalies NETwork). In *American Astronomical Society Meeting Abstracts*, volume 27 of *Bulletin of the American Astronomical Society*, page 117.04, December 1995.

C. Alcock, C. W. Akerlof, R. A. Allsman, T. S. Axelrod, D. P. Bennett, S. Chan, K. H. Cook, K. C. Freeman, K. Griest, S. L. Marshall, H.-S. Park, S. Perlmutter, B. A. Peterson, M. R. Pratt, P. J. Quinn, A. W. Rodgers, C. W. Stubbs, and W. Sutherland. Possible gravitational microlensing of a star in the Large Magellanic Cloud. *Nature*, 365:621–623, October 1993. doi: 10.1038/365621a0.

R. A. Alpher, H. Bethe, and G. Gamow. The Origin of Chemical Elements. *Physical Review*, 73:803–804, April 1948. doi: 10.1103/PhysRev.73.803.

R. Amanullah, C. Lidman, D. Rubin, G. Aldering, P. Astier, K. Barbary, M. S. Burns, A. Conley, K. S. Dawson, S. E. Deustua, M. Doi, S. Fabbro, L. Faccioli, H. K. Fakhouri, G. Folatelli, A. S. Fruchter, H. Furusawa, G. Garavini, G. Goldhaber, A. Goobar, D. E. Groom, I. Hook, D. A. Howell, N. Kashikawa, A. G. Kim, R. A. Knop, M. Kowalski, E. Linder, J. Meyers, T. Morokuma, S. Nobili, J. Nordin, P. E. Nugent, L. Östman, R. Pain, N. Panagia, S. Perlmutter, J. Raux, P. Ruiz-Lapuente, A. L. Spadafora, M. Strovink, N. Suzuki, L. Wang, W. M. Wood-Vasey, N. Yasuda, and T. Supernova Cosmology Project. Spectra and Hubble Space Telescope Light Curves of Six Type Ia Supernovae at $0.511 < z < 1.12$ and the Union2 Compilation. *The Astrophysical Journal*, 716:712–738, June 2010. doi: 10.1088/0004-637X/716/1/712.

D. J. Bacon, A. R. Refregier, and R. S. Ellis. Detection of weak gravitational lensing by large-scale structure. *MNRAS*, 318:625–640, October 2000. doi: 10.1046/j.1365-8711.2000.03851.x.

J. M. Bardeen, J. R. Bond, N. Kaiser, and A. S. Szalay. The statistics of peaks of Gaussian random fields. *The Astrophysical Journal*, 304:15–61, May 1986. doi: 10.1086/164143.

M. Bartelmann. Lensing Sunyaev-Zel'dovich clusters. *Astronomy & Astrophysics*, 370:754–764, May 2001. doi: 10.1051/0004-6361:20010322.

M. Bartelmann. The dark Universe. *Reviews of Modern Physics*, 82:331–382, January 2010. doi: 10.1103/RevModPhys.82.331.

M. Bartelmann and P. Schneider. Weak gravitational lensing. *Physics Reports*, 340:291–472, January 2001. doi: 10.1016/S0370-1573(00)00082-X.

M. Birkinshaw. The Sunyaev-Zel'dovich effect. *Physics Reports*, 310:97–195, March 1999. doi: 10.1016/S0370-1573(98)00080-5.

R. D. Blandford and R. Narayan. Cosmological applications of gravitational lensing. *Annual Review of Astronomy and Astrophysics*, 30:311–358, 1992. doi: 10.1146/annurev.aa.30.090192.001523.

N. W. Boggess, J. C. Mather, R. Weiss, C. L. Bennett, E. S. Cheng, E. Dwek, S. Gulkis, M. G. Hauser, M. A. Janssen, T. Kelsall, S. S. Meyer, S. H. Moseley, T. L. Murdock, R. A. Shafer, R. F. Silverberg, G. F. Smoot, D. T. Wilkinson, and E. L. Wright. The COBE mission - Its design and performance two years after launch. *The Astrophysical Journal*, 397:420–429, October 1992. doi: 10.1086/171797.

M. Bradač, D. Clowe, A. H. Gonzalez, P. Marshall, W. Forman, C. Jones, M. Markevitch, S. Randall, T. Schrabback, and D. Zaritsky. Strong and Weak Lensing United. III. Measuring the Mass Distribution of the Merging Galaxy Cluster 1ES 0657-558. *The Astrophysical Journal*, 652:937–947, December 2006. doi: 10.1086/508601.

J. E. Carlstrom, G. P. Holder, and E. D. Reese. Cosmology with the Sunyaev-Zel'dovich Effect. *Annual Review of Astronomy and Astrophysics*, 40:643–680, 2002. doi: 10.1146/annurev.astro.40.060401.093803.

D. Coe. Dark Matter Halo Mass Profiles. *ArXiv e-prints*, May 2010.

A. H. Compton. A Quantum Theory of the Scattering of X-rays by Light Elements. *Physical Review*, 21: 483–502, May 1923a. doi: 10.1103/PhysRev.21.483.

A. H. Compton. The Spectrum of Scattered X-Rays. *Physical Review*, 22:409–413, November 1923b. doi: 10.1103/PhysRev.22.409.

A. J. Connolly, R. Scranton, D. Johnston, S. Dodelson, D. J. Eisenstein, J. A. Frieman, J. E. Gunn, L. Hui, B. Jain, S. Kent, J. Loveday, R. C. Nichol, L. O'Connell, M. Postman, R. Scoccimarro, R. K. Sheth, A. Stebbins, M. A. Strauss, A. S. Szalay, I. Szapudi, M. Tegmark, M. S. Vogeley, I. Zehavi, J. Annis, N. Bahcall, J. Brinkmann, I. Csabai, M. Doi, M. Fukugita, G. S. Hennessy, R. Hindsley, T. Ichikawa, Ž. Ivezić, R. S. J. Kim, G. R. Knapp, P. Kunszt, D. Q. Lamb, B. C. Lee, R. H. Lupton, T. A. McKay, J. Munn, J. Peoples, J. Pier, C. Rockosi, D. Schlegel, C. Stoughton, D. L. Tucker, B. Yanny, and D. G. York. The Angular Correlation Function of Galaxies from Early Sloan Digital Sky Survey Data. *The Astrophysical Journal*, 579:42–47, November 2002. doi: 10.1086/342787.

A. Cooray. Large scale pressure fluctuations and the Sunyaev-Zel'dovich effect. *Physical Review D*, 62(10): 103506, November 2000. doi: 10.1103/PhysRevD.62.103506.

A. Cooray and R. Sheth. Halo models of large scale structure. *Physics Reports*, 372:1–129, December 2002. doi: 10.1016/S0370-1573(02)00276-4.

M. Davis, G. Efstathiou, C. S. Frenk, and S. D. M. White. The evolution of large-scale structure in a universe dominated by cold dark matter. *The Astrophysical Journal*, 292:371–394, May 1985. doi: 10.1086/163168.

R. H. Dicke, P. J. E. Peebles, P. G. Roll, and D. T. Wilkinson. Cosmic Black-Body Radiation. *The Astrophysical Journal*, 142:414–419, July 1965. doi: 10.1086/148306.

S. Dodelson. *Modern cosmology*. 2003.

O. Doré, F. R. Bouchet, Y. Mellier, and R. Teyssier. Cluster physics from joint weak gravitational lensing and Sunyaev-Zel'dovich data. *Astronomy & Astrophysics*, 375:14–24, August 2001. doi: 10.1051/0004-6361:20010759.

F. W. Dyson, A. S. Eddington, and C. Davidson. A Determination of the Deflection of Light by the Sun's Gravitational Field, from Observations Made at the Total Eclipse of May 29, 1919. *Royal Society of London Philosophical Transactions Series A*, 220:291–333, 1920. doi: 10.1098/rsta.1920.0009.

J. Einasto and U. Haud. Galactic models with massive corona. I - Method. II - Galaxy. *Astronomy & Astrophysics*, 223:89–106, October 1989.

A. Einstein. Zur Elektrodynamik bewegter Körper. *Annalen der Physik*, 322:891–921, 1905. doi: 10.1002/andp.19053221004.

A. Einstein. Erklarung der Perihelionbewegung der Merkur aus der allgemeinen Relativitatstheorie. *Sitzungsber. preuss.Akad. Wiss., vol. 47, No.2, pp. 831-839, 1915*, 47:831–839, 1915.

A. Einstein. Die Grundlage der allgemeinen Relativitätstheorie. *Annalen der Physik*, 354:769–822, 1916. doi: 10.1002/andp.19163540702.

A. Einstein. Lens-Like Action of a Star by the Deviation of Light in the Gravitational Field. *Science*, 84:506–507, December 1936. doi: 10.1126/science.84.2188.506.

D. J. Eisenstein. Dark energy and cosmic sound [review article]. *New Astronomy Reviews*, 49:360–365, November 2005. doi: 10.1016/j.newar.2005.08.005.

K. A. Fisher. Statistical Tests. *Nature*, 136:474, September 1935. doi: 10.1038/136474b0.

A. Friedman. Über die Möglichkeit einer Welt mit konstanter negativer Krümmung des Raumes. *Zeitschrift fur Physik*, 21:326–332, December 1924. doi: 10.1007/BF01328280.

C. Giocoli, M. Bartelmann, R. K. Sheth, and M. Cacciato. Halo model description of the non-linear dark matter power spectrum at k much greater than $1\mathrm{Mpc}^{-1}$. *MNRAS*, 408:300–313, October 2010a. doi: 10.1111/j.1365-2966.2010.17108.x.

C. Giocoli, G. Tormen, R. K. Sheth, and F. C. van den Bosch. The substructure hierarchy in dark matter haloes. *MNRAS*, 404:502–517, May 2010b. doi: 10.1111/j.1365-2966.2010.16311.x.

A. H. Guth. Inflationary universe: A possible solution to the horizon and flatness problems. *Physical Review D (Particles and Fields)*, 23:347–356, January 1981. doi: 10.1103/PhysRevD.23.347.

N. Hand, G. E. Addison, E. Aubourg, N. Battaglia, E. S. Battistelli, D. Bizyaev, J. R. Bond, H. Brewington, J. Brinkmann, B. R. Brown, S. Das, K. S. Dawson, M. J. Devlin, J. Dunkley, R. Dunner, D. J. Eisenstein, J. W. Fowler, M. B. Gralla, A. Hajian, M. Halpern, M. Hilton, A. D. Hincks, R. Hlozek, J. P. Hughes, L. Infante, K. D. Irwin, A. Kosowsky, Y.-T. Lin, E. Malanushenko, V. Malanushenko, T. A. Marriage, D. Marsden, F. Menanteau, K. Moodley, M. D. Niemack, M. R. Nolta, D. Oravetz, L. A. Page, N. Palanque-Delabrouille,

K. Pan, E. D. Reese, D. J. Schlegel, D. P. Schneider, N. Sehgal, A. Shelden, J. Sievers, C. Sifón, A. Simmons, S. Snedden, D. N. Spergel, S. T. Staggs, D. S. Swetz, E. R. Switzer, H. Trac, B. A. Weaver, E. J. Wollack, C. Yeche, and C. Zunckel. Evidence of Galaxy Cluster Motions with the Kinematic Sunyaev-Zel'dovich Effect. *Physical Review Letters*, 109(4):041101, July 2012. doi: 10.1103/PhysRevLett.109.041101.

E. Hayashi, J. F. Navarro, C. Power, A. Jenkins, C. S. Frenk, S. D. M. White, V. Springel, J. Stadel, and T. R. Quinn. The inner structure of ΛCDM haloes - II. Halo mass profiles and low surface brightness galaxy rotation curves. *MNRAS*, 355:794–812, December 2004. doi: 10.1111/j.1365-2966.2004.08359.x.

D. A. Howell. Type Ia supernovae as stellar endpoints and cosmological tools. *Nature Communications*, 2: 350, June 2011. doi: 10.1038/ncomms1344.

E. Hubble. A Relation between Distance and Radial Velocity among Extra-Galactic Nebulae. *Proceedings of the National Academy of Science*, 15:168–173, March 1929. doi: 10.1073/pnas.15.3.168.

J. H. Jeans. The Stability of a Spherical Nebula. *Royal Society of London Philosophical Transactions Series A*, 199:1–53, 1902. doi: 10.1098/rsta.1902.0012.

A. Jenkins, C. S. Frenk, S. D. M. White, J. M. Colberg, S. Cole, A. E. Evrard, H. M. P. Couchman, and N. Yoshida. The mass function of dark matter haloes. *MNRAS*, 321:372–384, February 2001. doi: 10.1046/j.1365-8711.2001.04029.x.

B. Joachimi, P. Schneider, and T. Eifler. Analysis of two-point statistics of cosmic shear. III. Covariances of shear measures made easy. *Astronomy & Astrophysics*, 477:43–54, January 2008. doi: 10.1051/0004-6361: 20078400.

N. Kaiser. Weak Lensing and Cosmology. *The Astrophysical Journal*, 498:26, May 1998. doi: 10.1086/305515.

C. S. Kochanek and R. Narayan. LensClean - an algorithm for inverting extended, gravitationally lensed images with application to the radio ring lens PKS 1830-211. *The Astrophysical Journal*, 401:461–473, December 1992. doi: 10.1086/172078.

E. W. Kolb and M. S. Turner. *The early universe.* 1990.

E. Komatsu, K. M. Smith, J. Dunkley, C. L. Bennett, B. Gold, G. Hinshaw, N. Jarosik, D. Larson, M. R. Nolta, L. Page, D. N. Spergel, M. Halpern, R. S. Hill, A. Kogut, M. Limon, S. S. Meyer, N. Odegard, G. S. Tucker, J. L. Weiland, E. Wollack, and E. L. Wright. Seven-year Wilkinson Microwave Anisotropy Probe (WMAP) Observations: Cosmological Interpretation. *The Astrophysical Journal Supplements*, 192:18, February 2011. doi: 10.1088/0067-0049/192/2/18.

A. S. Kompaneets. *Zh. Éksp. Teor. Fiz.*, 31:876, 1956.

A. S. Kompaneets. *Sov. Phys.*, 4:730, 1957.

R. Laureijs, J. Amiaux, S. Arduini, J. . Augueres, J. Brinchmann, R. Cole, M. Cropper, C. Dabin, L. Duvet, A. Ealet, and et al. Euclid Definition Study Report. *ArXiv e-prints*, October 2011.

G. Lemaître. Expansion of the universe, A homogeneous universe of constant mass and increasing radius accounting for the radial velocity of extra-galactic nebulae. *MNRAS*, 91:483–490, March 1931.

A. Liddle. *An Introduction to Modern Cosmology, Second Edition*. May 2003.

A. R. Liddle and D. H. Lyth. *Cosmological Inflation and Large-Scale Structure*. April 2000.

E. M. Lifshitz. *Sov. Phys. JETP*, 10:116, 1946.

D. N. Limber. The Analysis of Counts of the Extragalactic Nebulae in Terms of a Fluctuating Density Field. II. *The Astrophysical Journal*, 119:655, May 1954. doi: 10.1086/145870.

R. Lynds and V. Petrosian. Giant Luminous Arcs in Galaxy Clusters. In *Bulletin of the American Astronomical Society*, volume 18 of *Bulletin of the American Astronomical Society*, page 1014, September 1986.

D. H Lyth. Introduction to Cosmology. *ArXiv Astrophysics e-prints*, December 1993.

J. C. Mather, D. J. Fixsen, R. A. Shafer, C. Mosier, and D. T. Wilkinson. Calibrator Design for the COBE Far-Infrared Absolute Spectrophotometer (FIRAS). *The Astrophysical Journal*, 512:511–520, February 1999. doi: 10.1086/306805.

Y. Mellier. Probing the Universe with Weak Lensing. *Annual Review of Astronomy and Astrophysics*, 37: 127–189, 1999. doi: 10.1146/annurev.astro.37.1.127.

D. Merritt, A. W. Graham, B. Moore, J. Diemand, and B. Terzić. Empirical Models for Dark Matter Halos. I. Nonparametric Construction of Density Profiles and Comparison with Parametric Models. *The Astronomical Journal*, 132:2685–2700, December 2006. doi: 10.1086/508988.

J. Merten, M. Cacciato, M. Meneghetti, C. Mignone, and M. Bartelmann. Combining weak and strong cluster lensing: applications to simulations and MS 2137. *Astronomy & Astrophysics*, 500:681–691, June 2009. doi: 10.1051/0004-6361/200810372.

C. J. Miller, R. C. Nichol, D. Reichart, R. H. Wechsler, A. E. Evrard, J. Annis, T. A. McKay, N. A. Bahcall, M. Bernardi, H. Boehringer, A. J. Connolly, T. Goto, A. Kniazev, D. Lamb, M. Postman, D. P. Schneider, R. K. Sheth, and W. Voges. The C4 Clustering Algorithm: Clusters of Galaxies in the Sloan Digital Sky Survey. *The Astronomical Journal*, 130:968–1001, September 2005. doi: 10.1086/431357.

H. J. Mo and S. D. M. White. An analytic model for the spatial clustering of dark matter haloes. *MNRAS*, 282:347–361, September 1996.

B. Moore, S. Ghigna, F. Governato, G. Lake, T. Quinn, J. Stadel, and P. Tozzi. Dark Matter Substructure within Galactic Halos. *The Astrophysical Journal Letters*, 524:L19–L22, October 1999. doi: 10.1086/312287.

V. F. Mukhanov and G. V. Chibisov. Quantum fluctuations and a nonsingular universe. *Soviet Journal of Experimental and Theoretical Physics Letters*, 33:532, May 1981.

D. Munshi, P. Valageas, L. van Waerbeke, and A. Heavens. Cosmology with weak lensing surveys. *Physics Reports*, 462:67–121, June 2008. doi: 10.1016/j.physrep.2008.02.003.

D. Munshi, S. Joudaki, P. Coles, and J. Smidt. Cross-correlating Sunyaev-Zel'dovich and Weak Lensing Maps. *ArXiv e-prints*, November 2011.

R. Narayan and M. Bartelmann. Lectures on Gravitational Lensing. *ArXiv Astrophysics e-prints*, June 1996.

J. F. Navarro, C. S. Frenk, and S. D. M. White. A Universal Density Profile from Hierarchical Clustering. *The Astrophysical Journal*, 490:493, December 1997. doi: 10.1086/304888.

J. Neyman and E. L. Scott. A Theory of the Spatial Distribution of Galaxies. *The Astrophysical Journal*, 116: 144, July 1952. doi: 10.1086/145599.

J. H. Oort. Some Problems Concerning the Structure and Dynamics of the Galactic System and the Elliptical Nebulae NGC 3115 and 4494. *The Astrophysical Journal*, 91:273, April 1940. doi: 10.1086/144167.

B. Paczynski. Gravitational microlensing by the galactic halo. *The Astrophysical Journal*, 304:1–5, May 1986. doi: 10.1086/164140.

P. J. E. Peebles. Large-scale background temperature and mass fluctuations due to scale-invariant primeval perturbations. *The Astrophysical Journal Letters*, 263:L1–L5, December 1982. doi: 10.1086/183911.

P. J. E. Peebles and J. T. Yu. Primeval Adiabatic Perturbation in an Expanding Universe. *The Astrophysical Journal*, 162:815, December 1970. doi: 10.1086/150713.

A. A. Penzias and R. W. Wilson. A Measurement of Excess Antenna Temperature at 4080 Mc/s. *The Astrophysical Journal*, 142:419–421, July 1965. doi: 10.1086/148307.

Planck Collaboration, P. A. R. Ade, N. Aghanim, M. Arnaud, M. Ashdown, J. Aumont, C. Baccigalupi, M. Baker, A. Balbi, A. J. Banday, and et al. Planck early results. I. The Planck mission. *Astronomy & Astrophysics*, 536:A1, December 2011a. doi: 10.1051/0004-6361/201116464.

Planck Collaboration, P. A. R. Ade, N. Aghanim, M. Arnaud, M. Ashdown, J. Aumont, C. Baccigalupi, A. Balbi, A. J. Banday, R. B. Barreiro, and et al. Planck early results. VIII. The all-sky early Sunyaev-Zeldovich cluster sample. *Astronomy & Astrophysics*, 536:A8, December 2011b. doi: 10.1051/0004-6361/201116459.

W. H. Press and P. Schechter. Formation of Galaxies and Clusters of Galaxies by Self-Similar Gravitational Condensation. *The Astrophysical Journal*, 187:425–438, February 1974. doi: 10.1086/152650.

M. J. Rees and D. W. Sciama. Large-scale Density Inhomogeneities in the Universe. *Nature*, 217:511–516, February 1968. doi: 10.1038/217511a0.

A. Refregier. Weak Gravitational Lensing by Large-Scale Structure. *Annual Review of Astronomy and Astrophysics*, 41:645–668, 2003. doi: 10.1146/annurev.astro.41.111302.102207.

S. Refsdal. On the possibility of determining Hubble's parameter and the masses of galaxies from the gravitational lens effect. *MNRAS*, 128:307, 1964.

Y. Rephaeli. Comptonization Of The Cosmic Microwave Background: The Sunyaev-Zeldovich Effect. *Annual Review of Astronomy and Astrophysics*, 33:541–580, 1995. doi: 10.1146/annurev.aa.33.090195.002545.

R. K. Sachs and A. M. Wolfe. Perturbations of a Cosmological Model and Angular Variations of the Microwave Background. *The Astrophysical Journal*, 147:73, January 1967. doi: 10.1086/148982.

B. M. Schäfer, C. Pfrommer, M. Bartelmann, V. Springel, and L. Hernquist. Detecting Sunyaev-Zel'dovich clusters with Planck - I. Construction of all-sky thermal and kinetic SZ maps. *MNRAS*, 370:1309–1323, August 2006. doi: 10.1111/j.1365-2966.2006.10552.x.

P. Schneider. Cosmological Applications of Gravitational Lensing. In E. Martinez-Gonzalez and J. L. Sanz, editors, *The Universe at High-z, Large-Scale Structure and the Cosmic Microwave Background*, volume 470 of *Lecture Notes in Physics, Berlin Springer Verlag*, page 148, 1996. doi: 10.1007/BFb0102585.

P. Schneider, L. van Waerbeke, M. Kilbinger, and Y. Mellier. Analysis of two-point statistics of cosmic shear. I. Estimators and covariances. *Astronomy & Astrophysics*, 396:1–19, December 2002. doi: 10.1051/0004-6361:20021341.

D. Scott and G. F. Smoot. Cosmic Microwave Background Mini-review. *ArXiv e-prints*, May 2010.

U. Seljak. Gravitational Lensing Effect on Cosmic Microwave Background Anisotropies: A Power Spectrum Approach. *The Astrophysical Journal*, 463:1, May 1996. doi: 10.1086/177218.

U. Seljak, J. Burwell, and U.-L. Pen. Sunyaev-Zeldovich effect from hydrodynamical simulations: Maps and low order statistics. *Physical Review D*, 63(6):063001, March 2001. doi: 10.1103/PhysRevD.63.063001.

J. L. Sérsic. Influence of the atmospheric and instrumental dispersion on the brightness distribution in a galaxy. *Boletin de la Asociacion Argentina de Astronomia La Plata Argentina*, 6:41, 1963.

R. K. Sheth and B. Jain. The non-linear correlation function and density profiles of virialized haloes. *MNRAS*, 285:231–238, February 1997.

R. K. Sheth and B. Jain. Substructure and the halo model of large-scale structure. *MNRAS*, 345:529–538, October 2003. doi: 10.1046/j.1365-8711.2003.06974.x.

R. K. Sheth and G. Tormen. Large-scale bias and the peak background split. *MNRAS*, 308:119–126, September 1999. doi: 10.1046/j.1365-8711.1999.02692.x.

J. Silk. Cosmic Black-Body Radiation and Galaxy Formation. *The Astrophysical Journal*, 151:459, February 1968. doi: 10.1086/149449.

G. F. Smoot, C. L. Bennett, A. Kogut, E. L. Wright, J. Aymon, N. W. Boggess, E. S. Cheng, G. de Amici, S. Gulkis, M. G. Hauser, G. Hinshaw, P. D. Jackson, M. Janssen, E. Kaita, T. Kelsall, P. Keegstra, C. Lineweaver, K. Loewenstein, P. Lubin, J. Mather, S. S. Meyer, S. H. Moseley, T. Murdock, L. Rokke, R. F. Silverberg, L. Tenorio, R. Weiss, and D. T. Wilkinson. Structure in the COBE differential microwave radiometer first-year maps. *The Astrophysical Journal Letters*, 396:L1–L5, September 1992. doi: 10.1086/186504.

G. Soucail, B. Fort, Y. Mellier, and J. P. Picat. A blue ring-like structure, in the center of the A 370 cluster of galaxies. *Astronomy & Astrophysics*, 172:L14–L16, January 1987.

V. Springel. The cosmological simulation code GADGET-2. *MNRAS*, 364:1105–1134, December 2005. doi: 10.1111/j.1365-2966.2005.09655.x.

V. Springel, S. D. M. White, A. Jenkins, C. S. Frenk, N. Yoshida, L. Gao, J. Navarro, R. Thacker, D. Croton, J. Helly, J. A. Peacock, S. Cole, P. Thomas, H. Couchman, A. Evrard, J. Colberg, and F. Pearce. Simulations of the formation, evolution and clustering of galaxies and quasars. *Nature*, 435:629–636, June 2005. doi: 10.1038/nature03597.

V. Springel, J. Wang, M. Vogelsberger, A. Ludlow, A. Jenkins, A. Helmi, J. F. Navarro, C. S. Frenk, and S. D. M. White. The Aquarius Project: the subhaloes of galactic haloes. *MNRAS*, 391:1685–1711, December 2008. doi: 10.1111/j.1365-2966.2008.14066.x.

T. Sumi, K. Kamiya, D. P. Bennett, I. A. Bond, F. Abe, C. S. Botzler, A. Fukui, K. Furusawa, J. B. Hearnshaw, Y. Itow, P. M. Kilmartin, A. Korpela, W. Lin, C. H. Ling, K. Masuda, Y. Matsubara, N. Miyake, M. Motomura, Y. Muraki, M. Nagaya, S. Nakamura, K. Ohnishi, T. Okumura, Y. C. Perrott, N. Rattenbury, T. Saito, T. Sako, D. J. Sullivan, W. L. Sweatman, P. J. Tristram, A. Udalski, M. K. Szymański, M. Kubiak, G. Pietrzyński, R. Poleski, I. Soszyński, Ł. Wyrzykowski, K. Ulaczyk, and Microlensing Observations in Astrophysics (MOA) Collaboration. Unbound or distant planetary mass population detected by gravitational microlensing. *Nature*, 473:349–352, May 2011. doi: 10.1038/nature10092.

R. A. Sunyaev and I. B. Zeldovich. The velocity of clusters of galaxies relative to the microwave background - The possibility of its measurement. *MNRAS*, 190:413–420, February 1980.

R. A. Sunyaev and Y. B. Zel'dovich. Small-Scale Fluctuations of Relic Radiation. *Astrophysics and Space Science*, 7:3–19, April 1970. doi: 10.1007/BF00653471.

R. A. Sunyaev and Y. B. Zel'dovich. The Observations of Relic Radiation as a Test of the Nature of X-Ray Radiation from the Clusters of Galaxies. *Comments on Astrophysics and Space Physics*, 4:173, November 1972.

M. Trodden and S. M. Carroll. TASI Lectures: Introduction to Cosmology. *ArXiv Astrophysics e-prints*, January 2004.

K. Umetsu, T. Broadhurst, A. Zitrin, E. Medezinski, D. Coe, and M. Postman. A Precise Cluster Mass Profile Averaged from the Highest-quality Lensing Data. *The Astrophysical Journal*, 738:41, September 2011. doi: 10.1088/0004-637X/738/1/41.

K. Umetsu, E. Medezinski, M. Nonino, J. Merten, A. Zitrin, A. Molino, C. Grillo, M. Carrasco, M. Donahue, A. Mahdavi, D. Coe, M. Postman, A. Koekemoer, N. Czakon, J. Sayers, T. Mroczkowski, S. Golwala, P. M. Koch, K.-Y. Lin, S. M. Molnar, P. Rosati, I. Balestra, A. Mercurio, M. Scodeggio, A. Biviano, T. Anguita, L. Infante, G. Seidel, I. Sendra, S. Jouvel, O. Host, D. Lemze, T. Broadhurst, M. Meneghetti, L. Moustakas, M. Bartelmann, N. Benítez, R. Bouwens, L. Bradley, H. Ford, Y. Jiménez-Teja, D. Kelson, O. Lahav, P. Melchior, J. Moustakas, S. Ogaz, S. Seitz, and W. Zheng. CLASH: Mass Distribution in and around MACS J1206.2-0847 from a Full Cluster Lensing Analysis. *The Astrophysical Journal*, 755:56, August 2012. doi: 10.1088/0004-637X/755/1/56.

D. Walsh, R. F. Carswell, and R. J. Weymann. 0957 + 561 A, B - Twin quasistellar objects or gravitational lens. *Nature*, 279:381–384, May 1979. doi: 10.1038/279381a0.

J. Wambsganß. Discovering Galactic planets by gravitational microlensing: magnification patterns and light curves. *MNRAS*, 284:172–188, January 1997.

S. Weinberg. *Cosmology*. Oxford University Press, 2008.

S. D. M. White and M. J. Rees. Core condensation in heavy halos - A two-stage theory for galaxy formation and clustering. *MNRAS*, 183:341–358, May 1978.

R. Williamson, B. A. Benson, F. W. High, K. Vanderlinde, P. A. R. Ade, K. A. Aird, K. Andersson, R. Armstrong, M. L. N. Ashby, M. Bautz, G. Bazin, E. Bertin, L. E. Bleem, M. Bonamente, M. Brodwin, J. E. Carlstrom, C. L. Chang, S. C. Chapman, A. Clocchiatti, T. M. Crawford, A. T. Crites, T. de Haan, S. Desai, M. A. Dobbs, J. P. Dudley, G. G. Fazio, R. J. Foley, W. R. Forman, G. Garmire, E. M. George, M. D. Gladders, A. H. Gonzalez, N. W. Halverson, G. P. Holder, W. L. Holzapfel, S. Hoover, J. D. Hrubes, C. Jones, M. Joy, R. Keisler, L. Knox, A. T. Lee, E. M. Leitch, M. Lueker, D. Luong-Van, D. P. Marrone, J. J. McMahon, J. Mehl, S. S. Meyer, J. J. Mohr, T. E. Montroy, S. S. Murray, S. Padin, T. Plagge, C. Pryke, C. L. Reichardt, A. Rest, J. Ruel, J. E. Ruhl, B. R. Saliwanchik, A. Saro, K. K. Schaffer, L. Shaw, E. Shirokoff, J. Song, H. G. Spieler, B. Stalder, S. A. Stanford, Z. Staniszewski, A. A. Stark, K. Story, C. W. Stubbs, J. D. Vieira, A. Vikhlinin, and A. Zenteno. A Sunyaev-Zel'dovich-selected Sample of the Most Massive Galaxy Clusters in the 2500 deg^2 South Pole Telescope Survey. *The Astrophysical Journal*, 738:139, September 2011. doi: 10.1088/0004-637X/738/2/139.

Y. B. Zel'dovich. Gravitational instability: An approximate theory for large density perturbations. *Astronomy & Astrophysics*, 5:84–89, March 1970.

W. Zheng, M. Postman, A. Zitrin, J. Moustakas, X. Shu, S. Jouvel, O. Host, A. Molino, L. Bradley, D. Coe, L. A. Moustakas, M. Carrasco, H. Ford, N. Benitez, T. R. Lauer, S. Seitz, R. Bouwens, A. Koekemoer, E. Medezinski, M. Bartelmann, T. Broadhurst, M. Donahue, C. Grillo, L. Infante, S. W. Jha, D. D. Kelson, O. Lahav, D. Lemze, P. Melchior, M. Meneghetti, J. Merten, M. Nonino, S. Ogaz, P. Rosati, K. Umetsu, and A. van der Wel. A magnified young galaxy from about 500 million years after the Big Bang. *Nature*, 489:406–408, 2012.

F. Zwicky. Nebulae as Gravitational Lenses. *Physical Review*, 51:290–290, February 1937a. doi: 10.1103/PhysRev.51.290.

F. Zwicky. On the Probability of Detecting Nebulae Which Act as Gravitational Lenses. *Physical Review*, 51: 679–679, April 1937b. doi: 10.1103/PhysRev.51.679.

F. Zwicky. On the Masses of Nebulae and of Clusters of Nebulae. *The Astrophysical Journal*, 86:217, October 1937c. doi: 10.1086/143864.